Chemical Applications of X-ray Charge-Density Analysis

Tibor S. Koritsanszky[†]

Department of Chemistry, University of the Witwatersrand, WITS 2050, Johannesburg, South Africa

Philip Coppens*

Department of Chemistry, State University of New York at Buffalo, Buffalo, New York, 14260-3000

Contents

I. Charge Densities from X-ray Diffraction

As X-ray scattering by electrons is much stronger than that of the nuclei, intensities of scattered X-rays are almost exclusively determined by the distribution of the electrons. Thus, X-ray diffraction is a priori a tool for the determination of electron distribution in solids. This was realized soon after the discovery of X-ray diffraction in 1912 and long before the development of quantum mechanics. Debye wrote in 1915 that "the experimental study of the scattering of atoms, in particular for light atoms, should get more attention, since along this way it should be possible to determine the arrangement of the electrons in the atoms".[1] That it took practically half a century for any significant progress in this direction to be made was due to inaccuracy of the data of that period and to the success of the spherical-atom approximation, according to which atomic scattering is assumed to be that of *spherically averaged ground-state atoms*. The vast majority of current X-ray structure determinations still use the spherical-atom assumption and tacitly assume that the nuclear positions follow from the maxima in the electron density.

The first indication of the shortcomings of this assumption came, predictably, from bond lengths involving hydrogen atoms. The H atom, lacking a shell of core electrons, is strongly affected by bonding. It was recognized as early as the 1950s that anomalously short X−H bonds from X-ray diffraction were

* To whom correspondence should be addressed. E-mail: coppens@acsu.buffalo.edu.
[†] Current address: Department of Chemistry, State University of New York at Buffalo, Buffalo, NY, 14260-3000.

Tibor Koritsanszky received his degrees from Eötvös Loránd University, Budapest (M.Sc. in Chemistry), and from the Free University of Berlin (Doc. Rer. Nat.). He worked as a Research Scientist for the Central Research Institute for Chemistry of the Hungarian Academy of Sciences, a Research Associate at the State University of New York at Buffalo and at the University of Bern, and an Assistant Professor in the Institute of Crystallography of the Free University of Berlin. In 1998 he joined the faculty of the University of Witwatersrand in Johannesburg, where he was an Associate Professor in the Department of Chemistry. Since 2000 he has been a Research Professor, Head of the Jan Boeyens Structural Chemistry Laboratory, and Director of the Molecular Design Research Center. His research interests include structural and computational chemistry and high-resolution crystallography with focus on modeling X-ray data and experimental determination of solid-state electron densities.

Philip Coppens received his Ph.D. degree from the University of Amsterdam and has since been employed at the Weizmann Institute of Science, Brookhaven National Laboratory and the State University of New York at Buffalo, where he is currently Distinguished Professor of Chemistry. He is a Corresponding Member of the Royal Dutch Academy of Sciences and a Doctor Honoris Causa of the University of Nancy, France. He is a Past President of the American Crystallographic Association and has served as President of the International Union of Crystallography from 1993 to 1996. Among his awards are the Gregori Aminoff Prize of the Royal Swedish Academy of Sciences and the Martin Buerger Award of the American Crystallographic Association. His research interests include X-ray charge-density analysis, synchrotron radiation crystallography and photocrystallography, the study of light-induced metastable and transient species in crystals, the latter by use time-resolved diffraction, and, in general, the combination of experimental results with parallel quantum mechanical calculations. His most recent book, entitled *X-ray Charge Densities and Chemical Bonding*, was published in 1997.

due to a migration of electron density from the region of the hydrogen nucleus into the bond, as predicted by the theory of covalent bonding.

Technical developments that started in the 1960s and are still continuing have made X-ray diffraction a unique tool for mapping the charge distribution in crystals. They include the development of automated diffractometers, much better low-temperature techniques, neutron diffraction, advances in computing power and software, the availability of intense and short wavelength synchrotron radiation, and more recently the advent of area detectors which allow collection of very large data sets of adequate accuracy in much shortened time periods of days, or even hours, rather than weeks or months. Indeed, an electron density microscope which would allow on-line examination of the electron density in crystals seems within the reach of the facilities currently available.

The density-based quantum theory of atoms in molecules (AIM) provides a powerful tool for the interpretation of X-ray determined charge densities. In a series of both theoretical and experimental studies, information well beyond classical atomic connectivity has been obtained from analysis of the charge distribution. For example and as discussed in more detail below, in *syn*-1,6:8,13-biscarbonyl[14]-annulene a transannular interaction is observed which is not included in the classical description of the molecule.[2] Similarly, in the alternating S,N ring of tetrasulfur tetranitride, an S−S bond path across the ring is found, which is not considered in the classical description of the molecule.[3] The AIM theory allows for a characterization of the nature of chemical interactions based on experimental and/or theoretical electron densities rather than being limited to the classical connectivity of atoms.

In addition, the crystallographic experiment yields information on the nature of intermolecular interactions, including charge transfer in cocrystals with more than one molecular component. Examples are the neutral to ionic transformation in TTF-chloranil, which is currently being investigated,[4] and studies on low-dimensional conductors such as TTF-TCNQ.[5] The important intermolecular interactions are identified by bond paths linking molecules. For hydrogen-bonded systems, the topological parameters of the bond paths have been used to derive relevant nonbonded potentials.[6]

Analysis of the Laplacian of the electron density shows that molecules pack in a key-lock arrangement in which regions of charge concentration face electron-deficient regions in adjacent molecules in crystals.

Quantitative evidence is accumulating for the enhancement of molecular dipole moments in solids relative to those of isolated molecules, especially in polar crystals. Perhaps not surprising, but now quantitatively accessible, molecules are found to have different dipole moments in different crystalline environments.

The difference between supported (i.e., bridged by other groups) and unsupported metal−metal bonds has been investigated, and the great variety of metal−ligand bonding is being analyzed. Metal atom d-orbital populations show expected differences in homologous series and between high- and low-spin complexes. As the field is broad, this review concentrates on its chemical applications and does not cover all aspects. In particular, extended solids are only mentioned briefly.

Given the breadth of applications, it is not surprising that a number of review articles and books have appeared. Among these are reviews by Hirshfeld[7] and Spackman, the latter on experimentally determined electrostatic moments up to 1992,[8] and comprehensive reviews by Spackman published in 1994[9] and 1997.[10] X-ray charge-density analysis is discussed in the 1999 compilation *Crystallography Across the Sciences*,[11] while two books have appeared. *X-ray Charge Densities and Chemical Bonding*[12] is a text suitable as an introduction for new practitioners of the field. The book *Electron Density and Bonding in Crystals*[13] gives details of the diffraction experiment and theory with more emphasis on the physical than on the chemical aspects of the method.

II. Elements of Electron Density Determination

A. Expressions

1. Electron Density

For a molecular system of N electrons and M nuclei, the stationary state function (Ψ) is a function of the electronic spin and space coordinates ($\tau_i = (s_i, r_i)$; $i = 1, 2, ..., N$) and, within the Born–Oppenheimer approximation, the fixed nuclear space coordinates (R_k; $k = 1, 2, ..., M$). The probability of finding any of the electrons in the volume element dr is given by

$$\rho(\mathbf{r})\,d\mathbf{r} = N\{\int|\Psi|^2\,d\tau'\}d\mathbf{r} \qquad (1)$$

where $d\tau'$ denotes integration over all spin coordinates and the space coordinates of all electrons but one. $\rho(\mathbf{r})$ is the electron density (ED), also referred to as the electronic charge density.

2. Structure Factor and Difference Densities

X-ray diffraction, being an electron–photon interaction phenomenon, needs to be interpreted on the basis of quantum mechanics.[14] The complexity involved in calculating the observed intensity pattern from first principles calls for approximations that are based on assumptions supported by independent observations.[15] Within the kinematical theory, the coherent, elastic scattering amplitude (F) of the diffracted beam is the Fourier transform of the thermal average of the electron density $\langle\rho(\mathbf{r})\rangle$ in the unit cell, which is defined by the lattice translation vectors $\mathbf{a}_{i,i=1,3}$

$$F(\mathbf{H}) = \int_V \langle\rho(\mathbf{r})\rangle \exp(2\pi i\mathbf{H}\mathbf{r})d\mathbf{r} \qquad (2)$$

where $\mathbf{H} = h\mathbf{a}_1^* + k\mathbf{a}_2^* + l\mathbf{a}_3^*$, is the scattering vector, with integral components with respect to the reciprocal axes $\mathbf{a}_{i,i=1,3}^*(\mathbf{a}_i\mathbf{a}_j^* = \delta_{ij})$, and V is the unit cell volume.[12]

The conventional reconstruction of the crystal structure from its diffraction image relies on the physically plausible assumption that atomic contributions dominate the total scattering, that is, electrons are primarily localized around the nuclei and their local distributions are fairly well described by individual atomic densities. This is the basis for the approximation in which the molecular (crystalline) ED is composed of a superposition of isolated atomic densities ρ^0. This is the independent atom model (IAM) in which a molecule is approximated as a *promolecule*, defined as the superposition of spherical densities of isolated atoms k centered at $\mathbf{R}_k$

$$\rho_{IAM}(\mathbf{r}) = \sum_k \rho_k^0(\mathbf{r} - \mathbf{R}_k) \qquad (3)$$

Atomic partitioning of the ED is an essential feature of topological analysis and an important concept in chemistry. In the diffraction analysis it is assumed that no electronic excitation takes place and that the averaged density $\langle\rho\rangle$ is a canonical ensemble average over pure vibrational states.[15] This *thermal average* can be expressed in closed form within the harmonic *convolution approximation*, according to which the total ED is described as a superposition of density units, each of which rigidly follows the motion of the nucleus it is attached to

$$\langle\rho(\mathbf{r})\rangle = \sum_k \int \rho_k(\mathbf{r} - \mathbf{R}_k^0 - \mathbf{u}_k)P_k(\mathbf{u}_k)d\mathbf{u}_k \qquad (4)$$

where ρ_k is the static ED of the kth scatterer at the equilibrium position $\mathbf{R}_k^0$ and P_k is the probability density function describing the vibrational displacement $\mathbf{u}_k$ of the kth center ($\mathbf{u}_k = \mathbf{R}_k - \mathbf{R}_k^0$). In the harmonic approximation

$$P(\mathbf{u}) = (2\pi)^{-3/2}\,|\mathbf{U}|^{-1/2}\exp\left(-\frac{1}{2}\mathbf{u}^t\mathbf{U}^{-1}\mathbf{u}\right) \qquad (5)$$

is a trivariate normal distribution with $\mathbf{U} = \langle\mathbf{u}\mathbf{u}^t\rangle$ being the mean-square atomic displacement tensor, the components of which are commonly referred to as atomic displacement parameters (ADP). More general vibrational distribution functions, accounting for anharmonic motion, may be required in specific cases and are available.[12]

The Fourier transform of (4), using eq.(5) leads to the generalized structure factor

$$F(\mathbf{H}) = \sum_k f_k(\mathbf{H})\exp(2\pi^2\mathbf{H}^t\mathbf{U}_k\mathbf{H})\exp(2\pi i\mathbf{H}\mathbf{R}_k^0) \qquad (6)$$

where f_k is the static scattering factor of the kth density unit.

In the conventional formalism ρ_k is taken as spherically averaged, ground-state atomic density ($\rho_k = \rho_k^0$). The more dominant the core scattering relative to the valence scattering of an atom, the better the approximation this independent atom model provides. For light atoms, however, the neglect of directional characteristics of their valence biases the interpretation of the data.[16] This effect has become increasingly evident as the precision of diffraction data has improved.[17] It was soon realized that differences between observed structure factors and those calculated with the spherical-atom model carry important information on density deformations due to chemical interactions in molecules and crystals.

The *deformation density* (the density with reference to that of the promolecule)

$$\Delta\rho(\mathbf{r}) = \frac{1}{V_{cell}} \sum_{\mathbf{H}} [F_{OBS}(\mathbf{H}) - F_{IAM}(\mathbf{H})] \exp(-2\pi i \mathbf{H}\mathbf{r}) \tag{7}$$

has been used extensively in charge-density studies for recognition of bonding features and for diagnostic purposes, but its quantitative application is limited because it is a thermally averaged function and is subject to the definition of the reference density.

Deformation densities as defined by eq 7 typically show density accumulation in bonds and lone pair regions. However, bonds such as O−O or F−F are exceptions, as the spherically averaged atoms subtracted have more electrons in the bonding region than atoms oriented with their singly occupied orbital pointing toward a bonded neighbor.[18] To represent chemical bonding, reference states composed of properly oriented, nonspherical ground-state atoms have been proposed and the corresponding difference densities referred to as *chemical deformation densities*.[19] Theoretical applications show that such functions do have the expected density features in bonding regions of molecules such as H−F and H_2O_2.[20]

The deformation density should be distinguished from the *residual density*, which represents the density not accounted for in a least-squares refinement. For a good quality data set and an adequate model, the latter should be relatively featureless. If the model is inadequate, the least-squares parameters will be biased such as to minimize the residual density. *Unbiased* structural parameters for the reference state used to calculate the deformation density may be obtained by neutron diffraction, from refinement of the high-order X-ray data, which are less affected by bonding, or, more common in recent studies, from the aspherical-atom (multipole) refinement. In the last two cases, standard X−H bond lengths from neutron diffraction must be used to obtain reliable positions of the hydrogen nuclei.

3. Aspherical-Atom Formalism

To account for the density deformations due to chemical bonding, several algorithms have been developed.[21,22] The commonly used models are based on the nucleus-centered finite multipole expansion of ρ. In the formalism of Hansen and Coppens,[22] the atomic electron density ρ is divided into three components

$$\rho(\mathbf{r}) = \rho_c(r) + P_v\kappa^3\rho_v(\kappa r) + \sum_{l=0}^{l_{max}} \kappa'^3 R_l(\kappa' r) \sum_{m=0}^{+l} P_{lm}d_{lm\pm}(\vartheta,\varphi) \tag{8}$$

where ρ_c and ρ_v are the spherical core and valence densities, respectively, and the summation in the third term accounts for valence deformations. The $d_{lm\pm}$ are density-normalized real spherical harmonics expressed in polar coordinates. The isolated atom valence density and the radial functions R_l are modified by the scaling parameters (κ and κ', respec-

tively) to account for the radial expansion or contraction of the valence shell.

The core and spherical valence densities can be calculated from Hartree−Fock (HF)[23] or relativistic HF[24] atomic wave functions, while the radial functions of the deformation density are usually taken as simple Slater functions with energy-optimized exponents[25] (α_l)

$$R_l(r) = \frac{\alpha_l^{n_l+3}}{(n_l+2)!}r^{n_l}e^{-\alpha_l r} \tag{9}$$

The leading terms in eq 7 correspond to the κ formalism,[26] while for $\kappa = 1$ and $P_v = N_v$ (N_v being the number of valence electrons) the IAM is retrieved. Since the spherical harmonic functions are Fourier transform invariant, the pseudoatom scattering factor takes the form

$$f(\mathbf{H}) = f_c(H) + P_v f_v(H/\kappa) + 4\pi \sum_{l=0}^{l_{max}} i^l \langle j_l(H/\kappa') \rangle \sum_{m=0}^{+l} P_{lm}d_{lm\pm}(\beta,\gamma) \tag{10}$$

where f_c and f_v are the Fourier transforms of ρ_c and ρ_v, respectively, $\langle j_l \rangle$ is the lth-order Fourier−Bessel transform of R_l

$$\langle j_l \rangle = \int j_l(2\pi Sr)R_l(r)\,dr \tag{11}$$

and $d_{lm\pm}(\beta,\gamma)$ are spherical harmonics expressed in reciprocal-space polar coordinates.

In addition to the conventional parameters, the charge-density parameters P_v, P_{lm}, κ, and κ' are optimized in the least-squares refinement based on the measured structure factors.

4. Electrostatic Properties from the Charge Density

The expectation value of any physical property represented by a one-particle operator $\hat{O}$ can be obtained from the ED with the expression

$$\langle \hat{O} \rangle = \int \hat{O}\rho(\mathbf{r})\,d\mathbf{r} \tag{12}$$

Properties of central importance are the electrostatic moments for which $\hat{O} = r_1^i\, r_2^j\, r_3^k$. The evaluation of this integral over part of a continuous charge distribution requires space partitioning, which introduces a dependence on the method used. For molecules in crystals or ergo for an atom in a molecule or extended solid, the definition of the volume over which the desired property is to be integrated becomes crucial. Space can be partitioned with well-defined *discrete* boundaries or with overlapping functions, often referred to as *fuzzy* boundaries. Examples of the latter are the Mulliken population analysis for atomic charges and Hirshfeld partitioning, in which the ED at a point in space is divided according to the relative contribution of each atom to the promolecule density at that point[27] (also called *stockholder partitioning*, as each atom gets back proportional to what it invested). While the Hirshfeld method is well defined, the Mulliken population analysis is basis-set dependent and may assign density remote from a nucleus

to that nucleus, especially when large basis sets including diffuse functions are used, as is now generally the case. As the atom-centered multipole formalism in eq 8 implies atomic partitioning, properties obtained by use of eq 10 are often referred to as *pseudoatomic* properties.

Since the atom-centered multipolar functions on the neighboring atoms overlap, the pseudoatom model corresponds to a fuzzy boundary partitioning scheme, unlike the topological-atom model which is based on discrete boundary partitioning (atomic basins bounded by zero-flux surfaces). The atomic charges and higher moments are definition-dependent and thus can only be compared when identically defined. On the other hand, the result of the integration over the whole molecule is less dependent on the nature of the partitioning scheme, as the density is low in the intermolecular region in which the boundaries are located.

Using the multipole formalism, atomic electric moments are readily evaluated in closed analytic forms;[12] molecular moments can subsequently be obtained from the atomic moments An element is nonzero if ρ has a component of the same symmetry; furthermore, the first nonvanishing moment is origin independent.

The diffraction method is capable of providing all components of each of the atomic and molecular moments: not only the magnitude but also the direction of the dipole moment vector are obtained. Numerous applications have shown that reliable estimates of molecular dipole and second moments can be obtained from the multipole representation of X-ray charge densities,[8] as discussed in section VII.B.

Another density-related property of chemical interest is the electrostatic potential (EP)

$$\Phi(\mathbf{r}) = \sum_{k=1}^{M} \frac{Z_k}{|\mathbf{R}_k - \mathbf{r}|} - \int \frac{\rho(\mathbf{r}')}{|\mathbf{r}' - \mathbf{r}|}d\mathbf{r}' \quad (13)$$

defined as the energy required to move a positive unit charge from infinity to the point in space defined by $\mathbf{r}$. The EP can be evaluated either from the structure factors via Fourier summation or analytically from the multipole expansion with parameters as determined by the least-squares (LS) procedure.[28] The former method leads to the potential in the periodic crystal, while the latter refers to a molecule lifted from the crystal. It is clear from the mathematical expressions involved that the EP depends strongly on the low-order reflections, the coefficients in the Fourier summation being equal to $F(\mathbf{H})/H^2$.

Thus, the electrostatic potential is less dependent on the weaker high-order reflections or on the completeness of the data set than the ED itself. The EP at the nucleus ($\Phi(\mathbf{r} = \mathbf{R}_k)$ is sensitive to the valence-shell redistribution. It is related to the binding energy of the 1s electron and dependent on the net charge of the atom considered.

Related properties are the electric field (EF) vector defined as the electric force associated with $\Phi(\mathbf{r})$

$$\mathbf{E}(\mathbf{r}) = -\nabla\Phi(\mathbf{r}) = \int \frac{\rho_{tot}(\mathbf{r}')(\mathbf{r} - \mathbf{r}')}{|\mathbf{r} - \mathbf{r}'|^3}d\mathbf{r}' \quad (14)$$

(with ρ_{tot} representing both the nuclear and electronic charge) and the electric field gradient (EFG), a tensor property with components

$$\Delta E_{\alpha\beta} = -\frac{\partial^2\Phi}{\partial r_\alpha \partial r_\beta} \quad (15)$$

For nuclei with an electric quadrupole moment, the magnitude of the EFG components at the nuclear positions can be measured by magnetic resonance and Mössbauer techniques. Though unlike spectroscopic methods, X-ray diffraction is applicable to any nucleus; the X-ray results can never be of comparable accuracy as they depend crucially on the ED close to the nucleus, which is not well determined by the X-ray experiment. On the other hand, the X-ray method gives more detailed information on the origin of the tensor components as the full ED is recorded.[29]

B. Experiment and Analysis

1. Experimental Conditions

The success of the experimental method is subject to the accuracy and the extent of the data and to the adequacy of the model used in the interpretation. The data collection, reduction, and refinement involved in ED studies are not trivial procedures and require considerable expertise.[30] The most important prerequisite—to maintain kinematical conditions during the measurement—is practically unattainable, but the use of smaller specimen allowed by the new technology has greatly reduced the difficulties. Behind this general approach is the expectation that "systematic errors" can be revealed and corrected for during data reduction and refinement. Among these effects, extinction and thermal diffuse scattering (TDS) are the most difficult to handle. Several models are in use for proper allowance for extinction,[31] and new empirical TDS corrections are being developed.[32] A further essential requirement is to measure intensity data covering the full reciprocal space up to the highest possible resolution (extending the data collection to as high scattering angles as possible). This can be achieved by lowering the wavelength of the primary radiation and/or by lowering the temperature at which the measurement is undertaken. The latter factor manifests itself not only in increased scattering power of the sample, but also in increased ratio of the coherent-elastic to the diffuse scattering, i.e., a reduction in thermal diffuse scattering. The advantages of very low temperature ($T \leq 20$ K) measurements[33] are, not unexpectedly, accompanied by technical complications. A typical experimental setup designed for such a task is a closed-cycle helium refrigerator mounted on a large four-circle diffractometer. Such systems have proven to deliver excellent data[34,35] but introduce experimental complications related to the size of the cryostat and the fact that the sample is hidden from view. Because of collision problems, the important high-order data range may be restricted. In several but not all[35]

designs, the primary beam enters the vacuum chamber through a cylindrical Be- or carbon-based window, the background scattering and absorption of which introduce uncertainties in the intensity measurement.[36] Because of this, use of open-flow helium systems, which avoid this difficulty, is now increasing. Rapid parallel data collection with area detectors has made such devices economically feasible.

Until recently, the majority of ED studies were based on data collected with conventional sources (X-ray tubes), scintillation counters, and liquid-nitrogen cooling devices. To achieve the required accuracy with a point detector, the angular profile of the diffraction peak must be scanned for each reflection. The reduction of integrated intensity to structure factor amplitudes is a well-developed procedure that can lead to accurate and reproducible data.[37] Nevertheless, the time-consuming nature of such serial measurements severely limits extended applications.

The field of ED determination has been revolutionized by the development of new detectors. With area detectors, such as image plates (IP) and charge-coupled devices (CCD), the time needed to collect an extended data set is reduced from several weeks or even months to a few days, without considerable loss in precision.[38] The latter fact is basically due to the high level of redundancy achievable. Furthermore, synchrotron radiation has greatly advanced charge-density experiments.[39] The application of an intense, bright X-ray source of variable wavelength reduces systematic errors, increases the resolution, and enhances the accuracy of the data. Despite these advantages, only a few ED studies based on synchrotron radiation and serial detection have been reported,[40] basically because of beam-time limitations and the problem of short time intensity fluctuations of the source. Area detectors provide the solution, as demonstrated by the increasing number of studies based on both IP[41] and CCD[42] applications.

Technical difficulties associated with the use of area detectors in extreme low- temperature crystallography are being eliminated. A helium cryostat, equipped with a special "antiscatter" device inside the vacuum chamber to reduce the scattering of the direct beam by the carbon-fiber wall of the chamber, has been designed and applied successfully.[43] Because of the short measuring time required with area detectors, it becomes feasible to use open-flow helium cooling devices, a prototype of which has been described and applied in synchrotron diffraction studies.[44]

The quality of sealed-tube X-ray data collected with CCDs has been extensively tested for organic,[45] organometallic,[46] and inorganic[47] materials. The latest comparative study[47] has shown that the EDs obtained with CCDs mounted on different platforms, measured with different data collection strategies, and reduced with different data processing software, leading to various data redundancies and statistics, are consistent with each other and compare well with those derived from sequential data. The crucial question concerning area detector measurements is how to improve the peak integration. All presently available commercial data reduction programs[48] have

been designed for standard structure determinations and thus have not yet been developed to the sophistication that would be desirable for charge-density studies.

2. Data Analysis

The extraction of the ED from a set of structure factors can be viewed as a nonlinear basis transformation, that is, a projection from the reciprocal (diffraction) space representation of ρ to its real-space representation. If the complex Fourier components (i.e., the magnitudes and the phases of the structure factors) were available free of experimental errors, the real-space image could be reconstructed from the diffraction pattern via inverse Fourier transformation, with a precision subject to the resolution of the experiment. Since the phases are not known and the amplitudes are limited in number and accuracy, image formation is a multistep procedure. Starting with reasonable estimations of the phases provided by a well-established structure, the structure factor amplitudes predicted by a density model such as the multipole formalism are adjusted to the measured values through variation of the structural and charge-density parameters. A detailed mapping of the ED can thus be considered as the completion of structure determination. The problem is over-determined since the number of observations is larger than the number of parameters but is in a sense under-determined because of the lack of phase information.

Two mathematical methods have been implemented to complete the image formation: the method of least squares (LS) and entropy maximization. The latter one is the subject of active research leading to promising but at this time somewhat inconclusive results lacking consistent chemical information and therefore will not be discussed here. The reader interested in entropy maximization is referred to a review by Gilmore[49] as well as a recent article by Roversi et al.[50]

A variety of LS programs, based on different but mathematically equivalent models for the static density, have been developed and are used extensively (LSEXP,[21a] MOLLY,[22] VALRAY,[51] POP,[52] ASRED,[53] and XD[54]). Among these, VALRAY and XD provide routines to perform the topological analysis of the multipole density. The program NEWPROP,[55] interfaced to MOLLY, can map and analyze $\nabla^2\rho$, while the newest version of VALRAY[56] has an implementation for topological partitioning and property calculations. TOPXD,[57] an interface of TOPOND[58] to XD, is the latest development for calculation of one-electron AIM properties from the experimental electron density.

The LS procedure gives the best fit to the data for a given model and leads to parameter estimates and their uncertainties. For a given precision (gauged by the reproducibility of the observations), the correctness of these estimates depends on the completeness and efficiency of the model. Since the model is never perfect—it may be inadequate or ambiguous—the parameters can be either biased or indeterminate. Statistical tests are necessary but not sufficient in judging the accuracy. Charge-density refinements are

subject to the arbitrariness in the selection of the variables. The same data can often be fitted equally well, in a statistical sense, with different sets of variables, leading to statistically equivalent estimates of the parameters of the thermally averaged ED, but properties depending only on a subset of these variables could still be biased.

The usual practice is to try several models that differ in the selection of the variables. Applicable tests for the physical relevance of the mathematically equivalent LS solutions are limited. It is thus desirable to introduce restrictions among the variables to support the physically most significant solution. The pseudoatom model can be restricted by applying chemical and/or noncrystallographic local symmetry to the atomic densities. In the former case, the densities of equivalent atoms or functional groups, having similar chemical environment, are kept identical. Local symmetry can easily be imposed with properly chosen local coordinate systems centered at the atomic sites. In such frames, the symmetry restrictions on the pseudoatomic density can be formulated according to the index picking rules of the spherical harmonics applicable for the assumed local point group.[59] The requirement that the crystal be neutral can be imposed as a constraint on the monopole populations[22] by adding the $F_0 = N$ condition (F_0 and N being, respectively, the structure amplitude at zero scattering angle and the number of electrons in the unit cell) to the observations[60] (slack constraint) or by rescaling the valence-shell populations after completion of the refinement by the scale factor applied only to the core structure factors.[21b]

A generally accepted strategy followed almost routinely in multipole refinements is to start from the parameters of the IAM model and to increase the complexity of the model in a stepwise manner. Owing to their low scattering power and intense thermal motion, H atoms should be treated with a special care. The use of independent observations, mainly neutron diffraction parameters, is a clear advantage, provided systematic differences between neutron and X-ray thermal parameters are properly taken into account.[61] The physical significance of the ADPs of non-hydrogen atoms is also an important issue. An inadequate density model manifests itself in unreliable estimates for the ADPs or, in other words, *no reasonable estimate of the charge-density parameters can be obtained without an adequate description of the thermal motion.*

According to the rigid bond test, introduced by Hirshfeld,[62] the bond-projected components (z_A^2 and z_B^2) of the displacement tensors ($\mathbf{U}_A$ and $\mathbf{U}_B$) of a pair of covalently bonded atoms (A and B) of comparable nuclear mass should not differ markedly. The difference mean-square displacement amplitudes ($\Delta_{AB} = z_A^2 - z_B^2$) for atoms at least as heavy as carbon were estimated to be smaller than 0.001 Å^2. A significant departure from the *rigid-bond postulate* can mean that the ADPs are biased by unresolved or indeterminable valence density asphericities, by poor data quality, or by unrecognized disorder. It is thus reasonable to assume that restrictions on Δ_{AB}, applied in the fit of the structure factors, are likely to

support the physically most significant LS estimation of both the ADPs and the multipole populations. Intramolecular ADPs, calculated from ab initio force fields, can be incorporated into the refinement in terms of rigid-bond and rigid-link constraints.[63] A closely related approach is to start from ADPs predicted by the rigid-body model[64] (in this case $\Delta_{AB} = 0$ for all interatomic separation) and maintain the rigidity of the covalent bonds formed by atoms of comparable mass in subsequent cycles.[65]

Parameter indeterminacies are especially severe for noncentrosymmetric structures for which the LS solution can lead to a physically meaningless result.[66] The reason for this, as discussed in detail by El Haouzi et al.,[67] is that certain parameters or combinations of parameters are insensitive to the change in the structure factor amplitudes but are markedly affected by the phases. As a consequence, their estimates become indeterminate. Typical parameters of this nature are odd-order multipoles being invariant under crystal-class symmetry. In such a situation, application of chemical and/or noncrystallographic symmetry constraints is essential to retrieve a physically meaningful static density.

In exploring the performance of the aspherical-atom model and calibrating the extraction of electronic properties from X-ray diffraction data, model studies have become increasingly important. In the course of these studies, structure factors generated from ab initio wave functions of isolated molecules or crystals are used as observations. The clear advantage of this approach is that each condition affecting the "real situation" can be independently simulated.

Spackman and Byrom[68] analyzed the performance of multipole models of varying sophistication in reproducing theoretical electrostatic moments and electric field gradients at the nuclei of several molecules. Both static and dynamic (including thermal motion) structure factors were calculated at the HF level of theory for hypothetical crystals composed by superimposing isolated molecules as they occur in the corresponding real crystals. This study suggested a general trend for the model to underestimate the magnitudes of dipole moments by about 10−15% and to overestimate the traces of the second moment tensors by a few percent. On the other hand, the deviations of the largest principal components of the EFG tensors from the corresponding true values were found within the LS errors.

A number of studies aimed at the comparison of theoretical and experimental EDs have claimed improved agreement when the effects of nonbonded interactions and the crystal environment are included in the theoretical calculations.[69] Because of the increasing feasibility of periodic ab initio methods[70] on small organic systems, it has become possible to investigate crystal-field effects on the structure factors and on the corresponding multipole-projected ED. Extending their approach to interacting systems, Spackman at al.[71] showed that though the inclusion of molecular interactions in the theoretical structure factor calculation results in only minor changes, the effect is systematic and nonuniform in both reciprocal
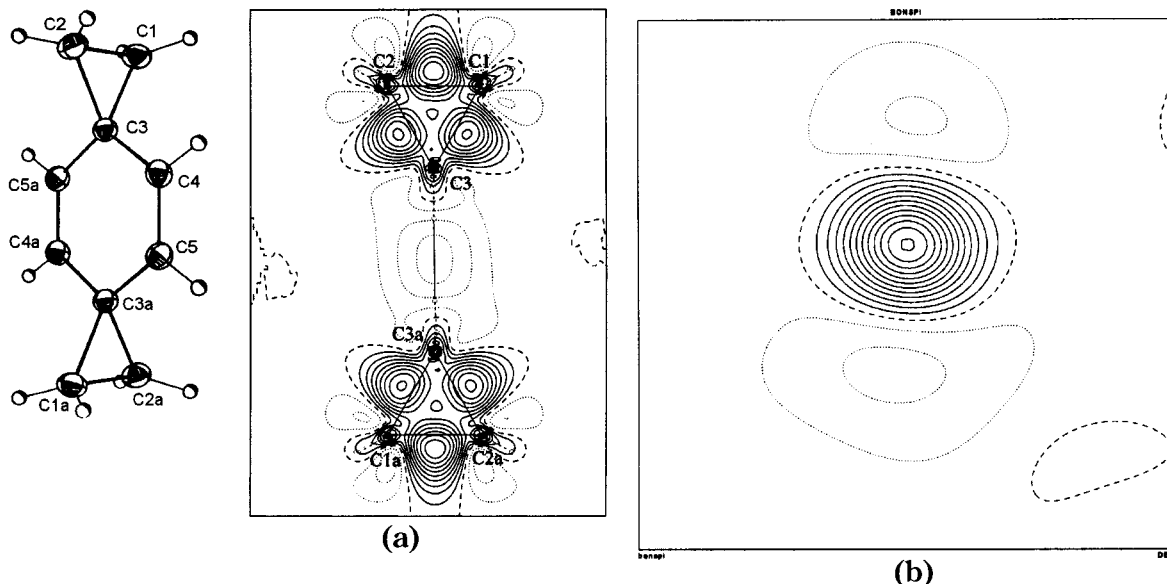
(a)   **(b)**

Figure 1. Static deformation density in dispiro [2,2,2,2] deca-4,9-diene (a) in the cyclopropyl rings, (b) in the C−C bond *exo* to the three-membered ring, showing π-character of the bond. The molecular diagram is shown on the left. (Reprinted with permission from ref 74. Copyright 1997 Wiley-VCH.)

and direct spaces. The multipole models applied appeared to successfully retrieve all characteristics of the interaction density and to correctly account for the enhancement of the dipole moment upon crystallization. In a closely related model study on urea, de Vries at al.[72] demonstrated that this was not the case for this noncentrosymmetric structure, if random noise was introduced into the simulated data. Spackman et al.[73] also analyzed the problem of phase retrieval in noncentrosymmetric space groups by means of model refinements on theoretical structure factors of several small-molecule crystals. An important point that emerged from this study is the capability of the multipole model to retrieve the phases with the desired accuracy. For the seven structures examined (with the exception of hexamethylenetetramine), the root-mean-square phase angle error $((\sum_{\mathbf{H}}(\varphi_{true} - \varphi_{mod\ el})^2/N_{obs})^{1/2})$ was found to be less than 2° while the error in the Fourier density amounted to about 0.01 e/Å^3. It was also shown that the eigenvalue filtering technique leads to a dramatic improvement in the phasing of the hexamethylenetetramine data, for which the unconstrained model performed poorly. On the basis of examination of the eigenvector associated with the lowest eigenvalue, the linear dependence between *xyz*-type octupole populations ($P_{3,-2}$) of the C and N atoms could clearly be identified as the origin of the phase indeterminacy. Despite these promising results, the phase problem remains an important issue needing further attention, especially in view of recent studies extending charge-density determination to biochemical systems.[176,178,179]

III. Chemistry from the Electron Density

A. Use of the Deformation Density

Deformation densities were used extensively in early charge-density analyses and indeed provided the first confirmation that bonding features are accessible by accurate X-ray methods. They generally but not always (see comments made in section II.A.2 above) show density in bond and lone pair regions and thus confirm long-used chemical concepts. When the density is calculated directly from the observed structure factors and a reference density subjected to thermal motion is subtracted (eq 7), a *thermally averaged* density at experimental resolution is obtained. Deformation densities shown in most recent work, however, are based on the functions and populations from the aspherical-atom (multipole) refinement and do not include the effect of thermal smearing. They thus correspond to a 'static' density at infinite resolution, with the caveat that any features beyond the experimental resolution are inescapably dependent on the nature of the basis set of functions used in the refinement. Nevertheless, such maps have great diagnostic potential and are routinely used to check the quality of an analysis. By comparing experimental densities with those from periodic theoretical calculations, shortcomings in either method can become apparent.

A recent example of meaningful chemical information extracted from the deformation density is provided by the combined experimental and theoretical studies of conjugation of cyclopropane ring with neighboring double bonds by Boese and co-workers.[74,75] The conjugation of the HOMO of a cyclopropyl ring with the LUMO of the neighboring π-system leads to a lengthening of the cyclopropyl-ring bond connected to the conjugated system and a shortening of the bond exocyclic to the propyl ring. The deformation electron density in the rings of one of the compounds investigated, dispiro[2,2,2,2]deca-4,9 diene in which two double bonds and two cyclopropane rings are aligned alternately around a ring of six carbon atoms, is shown in Figure 1a. The characteristic bending of the bonds in the three-membered rings is evident. In this and in several other examples reported, the bonds adjacent to the cyclopropane rings show significant elongation of the deformation density peak in the π-direction (Figure 1b), thus

giving direct evidence for conjugation between the cyclopropyl rings and the double bonds.

B. Theory of Atoms in Molecules

1. Topological Atom

The widely used concept of the atom as a building block, according to which a chemical system such as a molecule consists of units bearing recognizable and transferable contributions to the properties of the total system, has only recently been defined rigorously on the basis of quantum theory. Bader and co-workers showed that[76] based on its state function, a many electron system can uniquely be partitioned into open quantum subsystems (Ω) which satisfy specific boundary conditions. Such open systems, referred to as atoms in molecules (AIM), are regions of real space bound by surfaces of local zero flux (S) in the gradient field of ρ, $\nabla\rho(\mathbf{r})$, and contain a single nucleus. The normals to S, $\mathbf{n}(\mathbf{r})$, are perpendicular to the gradient vectors of the charge density

$$\nabla\rho(\mathbf{r})\cdot\mathbf{n}(\mathbf{r}) = 0, \ \forall\mathbf{r}\in S(\Omega,\mathbf{r}), \ \mathbf{n}(\mathbf{r}) \perp S(\Omega,\mathbf{r}) \quad (16)$$

Atoms are thus real-space topological "objects" defined as disjoint spatial regions that can exchange charge and momentum across their interaction surface S and whose observables obey the quantum equations of motion. This new concept of the atom emerges from the topology of the ED of the molecule, and as a natural consequence, concepts such as the chemical bond, molecular structure, and molecular stability are also deducible from the electron density topology.

2. Topological Structure of Molecules

The topology of a scalar field, such as ρ, can be explored by analyzing its gradient vector field (Figure 2). Since $\nabla\rho$ points in the direction of the largest increase in ρ, a path following its increase (a trajectory) must originate at a minimum or saddle point
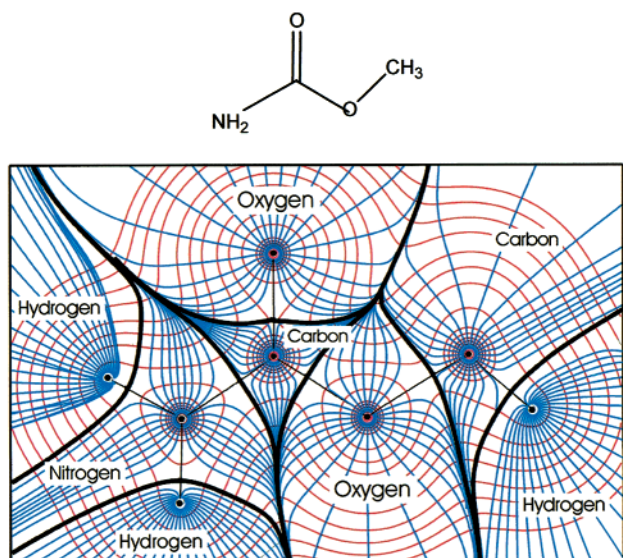

Figure 2. Methyl carbamide. The trajectories of the gradient of the charge density superimposed on the charge-density contours. Zero-flux surfaces forming the boundaries of the atomic basins are indicated by bold lines.[232]

(minimum in at least one direction) and terminate at a maximum or saddle point (maximum in at least one direction) of ρ. Each of these locations of extrema is associated with a critical point (CP) where $\nabla\rho$ ($\mathbf{r}_{CP}$) $= 0$. A CP is characterized by the rank (ω) of the Hessian matrix (the 3×3 ordered array of the second derivatives of ρ) and by the algebraic sum of the signs (σ) of the principal curvatures of ρ ($\mathbf{r}_{CP}$). The eigenvalues of the Hessian at $\mathbf{r}_{CP}$ are labeled λ_1, λ_2, and λ_3 with $\lambda_1 \leq \lambda_2 \leq \lambda_3$. At a CP where all curvatures are negative (($\omega = 3$, $\sigma = -3$)CP), ρ exhibits a local maximum; this typically occurs at nuclear positions (ρ has a cusp here which is homeomorphic to a maximum). All trajectories in the neighborhood of a $(3,-3)$CP terminate at this point, and they collectively define the region of space associated with the corresponding nucleus. Thus, a topological-atom is the union of the attractor and its associated basin.[77] The interaction between two such domains results in formation of a $(3,-1)$CP of ρ between the nuclei in question, a saddle point which is called a bond critical point (BCP). The pairs of trajectories (corresponding to the eigenvector associated with the positive eigenvalue λ_3) originating at this point and terminating at the two $(3,-3)$CPs define the line of maximum density linking two atoms. The existence of this atomic interaction line[78] indicates charge accumulation between the nuclei—a necessary condition for bond formation. The interaction line corresponding to equilibrium nuclear separation is referred to as the bond path (BP), and its presence is considered a sufficient condition for two nuclei to be bonded. The network of the BPs in a molecule is interpreted as the molecular graph associated with a stable structure. To each point in the nuclear configuration space, one and only one graph can be assigned. As a consequence of particular geometrical arrangements of BPs, two additional types of stable CPs can be formed. The occurrence of a $(3,+1)$CP or ring critical point (RCP) is the result of the linkage of BPs so as to form a ring. The set of the trajectories originating at the RCP form the ring surface. All of these paths terminate at the nuclei of the ring, except for a set of single trajectories each of which terminates at one of the BCPs associated with the BPs of the ring. A local minimum of ρ (a $(3,+3)$CP or cage critical point (CCP) is found in the interior of a molecule enclosed by ring surfaces. Trajectories only originate at a CCP and terminate either at the nuclei, or at the BCPs, or at the RCPs. For a number of different types of CPs ($m(\omega,\sigma)$), the Poincaré−Hopf relationship[79] holds

$$m(3,-3) - m(3,-1) + m(3,+1) -$$
$$m(3,+3) = 1 \quad (17)$$

For crystals, this equality is modified such that its right-hand side becomes equal to zero (the Morse relation).[80]

3. Topological Classification of Atomic Interactions

Those trajectories that terminate at the BCP and correspond to the eigenvectors associated with the negative eigenvalues λ_1, λ_2, span the interatomic surface S. Since the perpendicular curvatures λ_1 and λ_2 of ρ at the BCP are negative, charge is locally

concentrated here with respect to points on S. The parallel curvature (along the bond path) is positive at the BCP; thus, charge is locally depleted here relative to points along the BP.

The nature of the interaction depends on which of the curvatures dominates. *Shared* interactions (covalent bonds) are dominated by the negative curvatures; charge is concentrated in the internuclear region as a result of the perpendicular contractions of ρ toward the BP. This charge concentration is reflected in a relatively large value of $\rho(\mathbf{r}_{BCP})$ and in a large negative value of the Laplacian ($\nabla^2\rho(\mathbf{r}_{BCP})$), the sum of the principal curvatures ($\lambda_1 + \lambda_2 + \lambda_3$). For *closed-shell* interactions (i.e., ionic and van der Waals interactions), the positive curvature of ρ along the BP is dominant; charge is depleted in the interaction surface as a result of the contraction of ρ toward each of the nuclei. This charge depletion is characterized by a relatively low value of $\rho(\mathbf{r}_{BCP})$ and by a low positive value of $\nabla^2\rho(\mathbf{r}_{BCP})$.

The Laplacian of ρ is related, through the local virial theorem, to the electronic kinetic energy density ($G(\mathbf{r})$) and the potential energy density of the electrons ($V(\mathbf{r})$)

$$2\,G(\mathbf{r}) + V(\mathbf{r}) = \frac{1}{m}\left(\frac{h}{4\pi}\right)^2\nabla^2\rho(\mathbf{r}) \qquad (18)$$

where m is the mass of the electron.

This relationship indicates that the potential/kinetic energy dominates over the total energy in those regions of space where charge is locally concentrated/depleted, that is, where $\nabla^2\rho(\mathbf{r}) < 0/\nabla^2\rho(\mathbf{r}) > 0$. For *shared interactions*, where charge is both accumulated (measured by $\rho(\mathbf{r}_{BCP})$) and concentrated (measured by $\nabla^2\rho(\mathbf{r}_{BCP})$) along the BP, there is a continuous region of space, including the valence regions of the participating atoms, over which the Laplacian is negative. In contrast to this situation, for *closed-shell interactions*, the valence regions of the atoms are separated by a region of space over which the Laplacian is positive.

A positive value of $\nabla^2\rho(\mathbf{r}_{BCP})$ can indicate a noncovalent dative bond, a purely ionic interaction, or a van der Waals interaction. However, in many cases the interpretation that two neighboring atoms are linked by a noncovalent dative bond is at variance with commonly used molecular orbital theory. It is to be noted that a different view may be obtained by examination of either the *Fermi hole density* (FHD) or the *electron localization function* (ELF),[81] which are accessible from the wave function. The FHD is a measure of the degree to which the density at a point $\mathbf{r}_2$ is excluded by the spreading out of the same spin density originating from an electron at $\mathbf{r}_1$. It is obtained by placing an α (spin up) reference electron at point $\mathbf{r}_1$ in the molecular space and plotting the exclusion of the same-spin density in that space. The ELF function is defined such that complete localization corresponds to a value of one, while gaslike delocalization gives a value equal to 0.5. In regions of space where no electron pairing occurs, its value would be close to zero. Both functions provide information on the degree of electron localization.[82]

The local properties of ρ at the BCP are thus characteristic of the particular type of interaction occurring between bonded atoms. The value of $\rho(\mathbf{r}_{BCP})$ can serve as a measure of the bond order in nonpolar covalent bonds.[83] The accumulation of charge in the binding region is necessary to balance the repulsive force acting between the nuclei. It is thus anticipated that $\rho(\mathbf{r}_{BCP})$ is in a direct relationship with the bond distance, that is, it increases as the bond length decreases, a correlation found for the C−C bonds in hydrocarbons.[84] The two negative curvatures of ρ at the BCP define the *bond ellipticity*, $\epsilon = \lambda_1/\lambda_2 - 1$, which is a measure of the extent to which charge is preferentially accumulated in a plane perpendicular to the BP. Since $\epsilon = 0$ for a cylindrically symmetric bond and is greater than 0 for a double bond, it is a measure of the π character and the extent of conjugation.

The BP does not necessarily coincide with the internuclear axes between the bonded pair of atoms. It is usually curved from the perimeter of strained rings or from the edges of cage structures. The deviation of the length of the BP from the internuclear distance is thus an indicator of the strain in a bond.[85] A curved BP suggests that the density is not distributed such as to maximally balance the repulsive forces of the nuclei.

4. Laplacian of the Electron Density

The Laplacian, a scalar field of ρ ($\nabla^2\rho(\mathbf{r}) = \partial^2\rho/\partial x^2 + \partial^2\rho/\partial y^2 + \partial^2\rho/\partial z^2$), plays an important role throughout the AIM theory and provides insight not only into static[86] (structural) but also into reactive properties[87] of a molecule. The region of the outer shell of an atom over which $\nabla^2\rho(\mathbf{r}_{BCP}) > 0$ is called the *valence shell charge concentration* (VSCC). Upon chemical bonding, this VSCC is distorted and extrema are formed (Figure 3). The maxima (bonded or nonbonded)
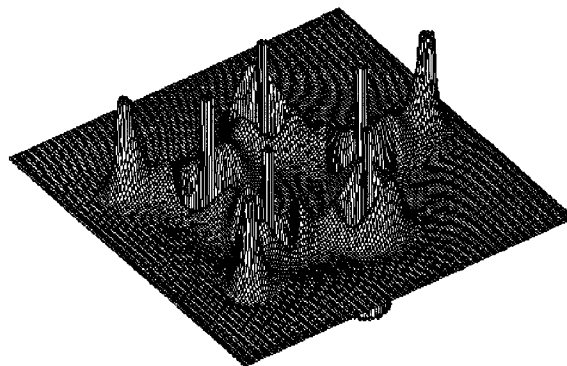

Figure 3. Relief map of the negative Laplacian of the electron density in the molecular plane of 1,2,4-triazole at the HF/6-311++G(3df, 3pd) level of theory. The values are truncated at 120 e/Å^5.[65] (Reprinted with permission from ref 65. Copyright 1997 Oldenbourg Verlage.)

correspond in number, location, and size to the localized pairs postulated in the Valence shell electron pair repulsion (VSEPR) model.[88]

If two reactants approach each other in a Lewis acid−base-type reaction, their relative orientation can be predicted by the Laplacian functions of their ED. Charge concentrations/depletions of one molecule

can be considered to be complementary to depletions/concentrations of the other. Thus, local features of the Laplacian can be used as plausible descriptors and predictors of molecular recognition and complementarity.

5. AIM Properties

For a system in a stationary state, an AIM property ($A(\Omega)$), a scalar, vector, or tensor, is obtained by the integration of the corresponding property density ($\rho_A(\mathbf{r})$) over the atomic basin

$$A(\Omega) = \int_\Omega \rho_A(\mathbf{r})d\mathbf{r} = \int_\Omega d\mathbf{r} \frac{N}{2} \int \{\Psi^* \hat{A}\Psi + (\hat{A}\Psi)^*\Psi\}d\tau' \quad (19)$$

where N is the number of electrons in the system and the second integration is over the spin coordinates of all electrons and the spatial coordinates of all electrons but one.

The most important consequence of this definition is that a physical property of the total system is given as the sum of its atomic properties

$$A = \int_\Omega A(\Omega) \quad (20)$$

The local virial theorem is the differential form of the corresponding atomic theorem obtained by integrating eq 18 over an atomic basin. As the integral of $\nabla^2\rho$ vanishes because of eq 16, the result is

$$2T(\Omega) = -V(\Omega) \text{ or } 2E(\Omega) = -V(\Omega) \text{ or } E(\Omega) = -T(\Omega) \quad (21)$$

where $E(\Omega)$, $V(\Omega)$, and $T(\Omega)$ are, respectively, the average electronic, potential, and kinetic energies of an atom. It is to be emphasized that this theorem provides the partitioning of the total energy into atomic contributions via eq 20. The theorem also ensures the highest degree of atomic transferability, that is, if the ED of an atom in two different molecules is identical, then the atom contributes an identical amount of energy to the total energies of both molecules.

The approach described above is unambiguous in the sense that it does not rely on any orbital model. It also provides a unique definition of the molecular structure because all nuclear configurations in the neighborhood of the equilibrium geometry are represented by equivalent molecular graphs. These aspects make the AIM theory a particularly useful interpretive tool in experimental charge-density studies. The density model used, although formally related to the wave function representation of the atomic density, is also free of assumptions on orbitals. However, the ED extracted from X-ray diffraction data, as discussed below, does not correspond to a pure quantum state.

IV. Topological Analyses of Experimental Densities

Important questions raised throughout the topological studies of experimental EDs are related to the above discussion: (i) to what extent does the topology of the experimental static model density compare with that derived from quantum-chemical calculations on the isolated, ground-state molecule and on the periodic system; (ii) if disagreement is found, is the information significant enough to draw conclusions on the nature of crystal-field effects and on intermolecular interactions; (iii) to what extent are experimental topological properties reproducible and which aspects of the experimental procedure have the greatest influence on their estimates?

As for the theoretical part, the quality of the wave function is the main concern, i.e., basis set effects and the approximations in the calculation are the crucial issues. The proper choice of the molecular geometry at which the wave function is calculated is also of relevance. The BCP properties, being sensitive indicators of the bond strength, correlate with the bond distance. The optimized geometry appears to be the right choice but it is usually distorted with respect to the geometry occurring in the crystal. For a meaningful comparison, it has proven mandatory to perform the calculation at the molecular geometry established experimentally.

As far as the experimental method is concerned, systematic errors, data resolution, model inadequacies and ambiguities, as well as inappropriate refinement strategies should be considered as possible sources of an unrealistic topology.

To elucidate these effects, combined experimental and theoretical studies are of central importance.

A. Experimental versus Theoretical Topology

Until recently, the vast majority of experimental topological studies have focused on organic compounds (molecular crystals), and a considerable amount of information on chemical bonds formed by the first-row elements has been accumulated. Many of these investigations include analysis of theoretical densities for comparison purposes. The most representative examples are chosen here to highlight basic trends. With few exceptions, a topological equivalence between experimental and theoretical densities (i.e., the same number and type of CPs) exists, and the agreement in terms of BCP properties is found to be generally satisfactory, outstandingly good for nonpolar bonds but less satisfactory for polar bonds.

1. Carbon–Carbon Bond

Owing to the fundamental nature of its bonding, diamond occupies a unique position in solid-state physics. The benchmark of an ideal C–C single bond has been the object of many theoretical and experimental studies.[89] The latest quantum topological analysis[90] uses a four-parameter model (κ, κ', $P_{3,-2}$, $P_{4,0}$, $P_{4,4} = 0.74045P_{4,0}$) to compare the results extracted from 10 experimental structure factors and from density functional-based theoretical data[91] with those obtained directly from periodic HF calculations by Zuo and Bader.[92] The procedures lead to statistically equal topological indices, as judged by the values of the densities and the Laplacian at the bond, ring, and cage CPs (Table 1). Both sp^3 and s^2p^2 configurations for the spherical valence density were tested in the fit of the simulated dynamic data sets

Table 1. Topological Properties of C−C Bonds[a]

|	$\rho(\mathbf{r}_{BCP})$	$\nabla^2\rho(\mathbf{r}_{BCP})$	ϵ	R
diamond	1.596(45)	−10.16(8)	0.00	1.5445(4)
	1.603	−12.26	0.00	
ethane	1.61	−16.1	0.31	1.510
	1.70	−15.9	0.0	1.528
ethylene	2.16	−16.7	0.19	1.336
	2.29	−22.4	0.22	1.306
acetylene	2.84	−31.2	0.00	1.183
	2.74	−31.3	0.00	1.190
benzene	2.15	−16.9	0.22	1.392
	2.20	−23.1	0.22	
bullvalene				
$\quad$ C(sp^3)-C(sp^2)	1.78(1)	−16.0(1)	0.04	1.5157(2)
	1.79	−17.5	0.02	
$\quad$ C(sp^2)−C(sp^2)	2.36(2)	−26.0(1)	0.29	1.3450(2)
	2.31	−25.2	0.43	
$\quad$ C(sp^2)−C(r)	1.92(2)	−19.3(1)	0.09	1.4727(2)
	1.91	−19.6	0.08	
$\quad$ C(r)−C(r)	1.54(1)	−7.3(1)	0.90	1.5352(2)
	1.57	−11.0	0.47	

[a] First line: experimental. Second line: theoretical, as follows. Diamond: from the fit of calculated structure factors (ref 91); ethane, ethylene, acetylene HF/6-31G (ref 93); benzene HF/3-21G* (ref 94); bullvalene MP2/6-31G** (ref 95).

of different resolution. The sp^3 model was shown to be superior to the s^{2}p^2 model since it gave a better fit and led to BCP properties insensitive to the data resolution.

The relatively weak intermolecular forces in hydrocarbon crystals are expected to have a minor influence on the primary topology of the molecular densities which constitute the building blocks of the crystal density. As dominant features of the isolated molecule are likely to be preserved in the crystal, it is not surprising that the earliest attempts to explore the topology of experimental densities were focused on the simplest hydrocarbons, such as ethane, ethylene, acetylene,[93] and benzene.[94] These studies demonstrated that the topological features from the multipole projection method are in accord with theoretical predictions, that is, local maxima occur only at the nuclear sites and BCPs are located at the midpoint of the $C-C$ bonds in regions of negative Laplacian. Despite the relatively low resolution of the X-ray data sets used in the early work, the BCP properties of the C−C bonds obtained in these studies (Table 1) are chemically meaningful. Both $\rho(\mathbf{r}_{BCP})$ and $-\nabla^2\rho(\mathbf{r}_{BCP})$ increase with increasing bond order, and the experimental quantities, especially $\rho(\mathbf{r}_{BCP})$, resemble closely those obtained at the HF/6-31 level of theory.

On the basis of the combined analysis of X-ray and neutron data of deuterated benzene, $\rho(\mathbf{r}_{BCP})$ averaged over the three symmetrically independent C−C bonds (the molecule lies on the center of inversion in an orthorombic unit cell of space group *Pbca*) was found to be 2.15 e/Å^3. This is in excellent agreement with the value of 2.2 e/Å^3 derived at the HF level. Although $\nabla^2\rho(\mathbf{r}_{BCP})$ appears to be slightly overestimated by the experiment (−17 compared to −23), the bond ellipticities perfectly match those obtained theoretically.

The study on bullvalene (**1**, Scheme 1)[95] demonstrates the topological equivalence between theoreti-

Scheme 1
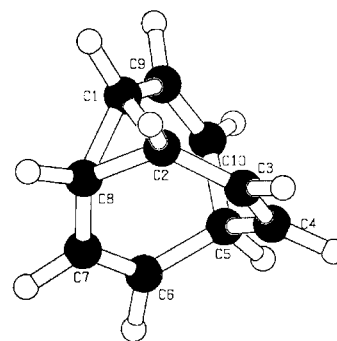
cal and experimental densities in the C−C bonds. This molecule exhibits four different types of C−C bonds: a C$_{sp^3}$ − C$_{sp^2}$ single, a C$_{sp^2}$ = C$_{sp^2}$ double, a C$_r$−C$_r$ bent bond in the cyclopropane ring, and a C$_{sp^2}$ − C$_r$ single bond which is conjugated with the adjacent double bonds. Although, the molecule occupies a general position in the unit cell, C_{3v} molecular symmetry was imposed in the multipole refinement and thus the bond properties refer to a symmetry-averaged density. The experimental results, included in Table 1, clearly show the expected differences for the bonds, in almost perfect agreement with the theory at MP2/6-311G** level. The highest/lowest density accumulation and contraction are found in the double/bent bonds by both methods, and the effect of conjugation, as anticipated by a simple orbital model, is also observed in terms of a relatively higher value of $\rho(\mathbf{r}_{BCP})$ and a lower value of $\nabla^2\rho(\mathbf{r}_{BCP})$ when the single C$_{sp^2}$−C$_r$ is compared with the single C$_{sp^3}$−C$_{sp^2}$ bond. As discussed above, the bent character of the bonds in the cyclopropane ring corresponds to an outward displacement of the bond peak in the deformation density, away from the midpoint of the internuclear line.[75] The displacement of the BCP of the cyclic C−C bond from the internuclear line is 0.02 Å (Figure 4a), which is much less than the corresponding distance of the deformation-density bond peak of 0.12 Å (Figure 4b), thus illustrating the sensitivity of the deformation maps to bonding features.

2. Polar Bonds

The correlation between experimental and theoretical topology for polar bonds was first discussed in detail by Gatti et al.[96] in their study on the ED of L-alanine extracted from 23 K X-ray data. In this study, the theoretical BCPs (calculated at the HF/6-31G** level of theory for the isolated molecule at the experimental geometry) were found to be located closer to the less electronegative atom in the C−O and C−N bonds than the experimental BCPs, leading to nonnegligible differences in the $\rho(\mathbf{r}_{BCP})$ and $\nabla^2\rho(\mathbf{r}_{BCP})$ values. The theory gave about 10−15% lower values for $\rho(\mathbf{r}_{BCP})$ than the experiment. This trend was much more pronounced for $\nabla^2\rho(\mathbf{r}_{BCP})$, especially for the C−O bonds of the carboxylate group. Since ρ usually possesses a relatively flat minimum along the bond path, $\rho(\mathbf{r}_{BCP})$ can be quite insensitive to the location of the BCP. The same may be true for $-\nabla^2\rho(\mathbf{r}_{BCP})$ in a nonpolar covalent bond
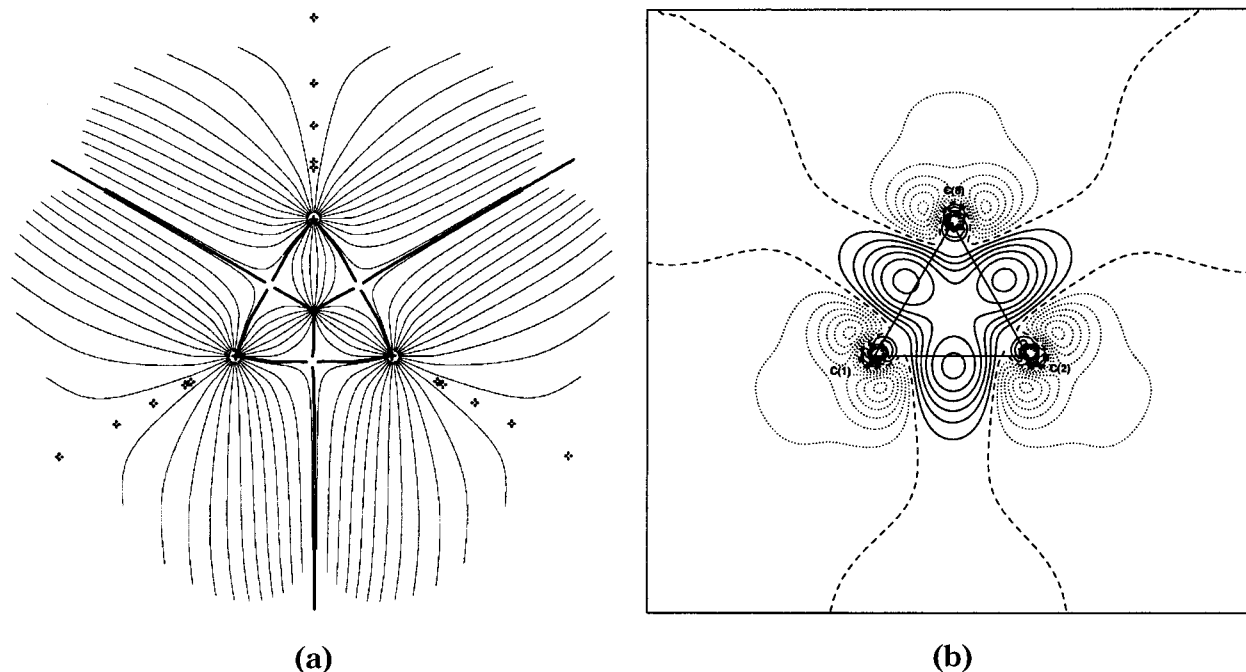
(a)

(b)

Figure 4. (a) Map of the gradient vector field of the theoretical charge density in the cyclopropane ring of bullvalene. The bond paths connecting the atoms and lines denoting the interatomic surfaces in this plane are drawn as heavy lines. (b) Experimental deformation density in this plane.[95]

in which this function exhibits a plateau between the two bonded VSCCs. However, for polar bonds, the BCP is usually located close to the bonded VSCC maximum of the less electronegative atom where the parallel curvature (λ_3) changes considerably. While the perpendicular curvatures obtained by the different methods tend to be in fair accordance, the parallel curvature in the C−O bond appears systematically underestimated by the experiment, leading to more negative experimental than theoretical $\nabla^2\rho(\mathbf{r}_{BCP})$ values. The effect of the quality of the basis set and the Coulomb correlation on the topology was also discussed in this report. The authors conclude, in agreement with earlier findings,[97] that changes in the parallel curvatures for covalent bonds can amount to up to 50% upon changing the basis functions and up to 20% upon including electron correlation. In contrast, the $\rho(\mathbf{r}_{BCP})$ values showed only moderate variation (~1%).

Since in the crystal structure of L-alanine the oxygen atoms of the carboxylate group are acceptors in hydrogen bonds, the discrepancies between theory and experiment could also be due to intermolecular interactions. This assumption did not gain support from a theoretical study on urea,[98] in which crystal-field effects on the topology of the carbonyl bond were analyzed by comparing the crystal density from periodic HF calculation with that derived for the isolated molecule (both calculations utilizing 6-31G** basis sets). Here, the BCP displacement upon crystallization was found to be lower for the C−O than for the C−N bond, accompanied by an increase and decrease, respectively, in the $-\nabla^2\rho(\mathbf{r}_{BCP})$ values. The VSCC of the *keto*-oxygen atom in the bulk was shown to be a nearly uniform torus-shaped electron-rich region, indicating an increased ability of the O atom to participate in hydrogen bonds. Accordingly, this

Scheme 2

2
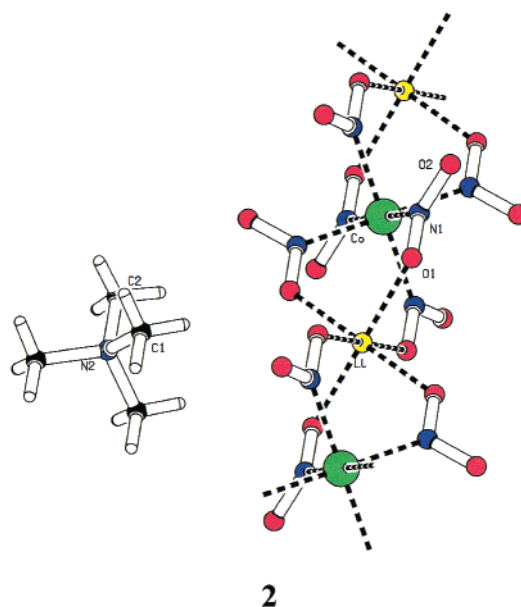
O atom is an acceptor in four H bonds. The rearrangement of the nonbonded region of the oxygen atom clearly results in a loss of π-character of the bond.

The theory versus experiment comparison was further explored by Bianchi et al. in their study of the EDs obtained by experiment and theory for lithium bis(tetramethylammonium)hexanitrocobaltate-(III) (**2**, Scheme 2).[99] The authors presented a detailed analysis of the BCP properties of the C−N and N−O bonds in the tetramethylammonium and nitro groups and found that the substantial discrepancies between the theoretical (periodic HF/3-21G* calculation) and experimental bond curvatures were not solely due to the different BCP locations. The disagreement was

especially pronounced for the N−O bonds in which the experimental λ_3 values were found to be much larger than the theoretical ones (λ_3(exp)/λ_3(theor) = 2.25 on average), not only at the BCP locations, but also in a broad interval around them. This results in the experimental $\nabla^2\rho(\mathbf{r}_{BCP})$ values being substantially less negative than those calculated from the wave function, a trend opposite to that found for the C−O bonds. A multipole refinement with extended radial functions for the valence deformation density did not improve the situation, neither did the refinement of anharmonic thermal parameters.

Howard et al.[100] reported experimental BCP indices for the C−O bonds in (2*S*)-3-(3′,4′-dihydroxyphenyl)-alanine (L-DOPA) and for the analogous bonds found the same anomaly as observed in L-alanine. Using a set of static structure factors generated from the wave function, they performed a multipole refinement with the same model, keeping the thermal parameters fixed at zero values and a refinement strategy as applied in the treatment of the real data. They found that the BCP indices of the theoretical density projected into the pseudoatom representation were in better agreement with the experimental than with the exact results. This observation suggests that the static density model as employed is inadequate in representing fine details of the topology of the carbonyl bond.

In the most recent study, Volkov et al.[101] give a detailed account of the different factors affecting the topology of the N−O, C−N, and aromatic C−C bonds in *p*-nitroaniline. Single-point calculations were performed on the isolated molecule at the experimental geometry at the HF, DFT, and MP2 levels, utilizing different basis sets. To elucidate crystal-field effects, full periodic calculations (PHF/6-21G** and PHF/6-31G**) were done. It was found, in line with earlier observations, that the basis set, correlation, and crystal-field effects manifest themselves mainly in the location of the BCP and in the magnitude of the positive curvature. The authors noted "*though these effects are important they cannot account for the differences in the theoretical and experimental topologies*". In fact, for the N−O and C−C bonds, the theoretical λ_3 values at PHF/6-311G** level were about two times lower than those extracted from 20 K synchrotron data. These discrepancies cannot be accounted for by the combined effect of basis set and correlation on the theoretical bond curvature, which is estimated as about 6 e/Å^3 in the worst case (the N−O bond). On the other hand, when the comparison was based on the PHF/6-311G** density projected into the multipole model, the agreement for the N−O and C−C bonds improved significantly. This confirms that the model as applied biases the topology of the ED. It follows that quantitative conclusions based on the comparison of theoretical and experimental results, especially for polar bonds, should be drawn with caution. The bias is most likely due to the inadequacy of the deformation radial functions (eq 9) or to the inadequate choice of their parameters (α_l and n_l) that are energy−rather than density− optimized. While the κ model, which includes only the spherical valence part (i.e., the $P_v\kappa^3\rho_v(\kappa r)$ term

in eq 8), has been proven to be successful in retrieving theoretical monopole deformations in diatomic molecules,[102] the experimental extraction of the corresponding information on the aspherical density may be suspect. The related κ' parameters are the least stable LS variables. Quite often, the convergence of their refinement can be reached only by using a block-diagonal approach that turns off their correlations with other parameters. The partitioning involved in the aspherical-atom model unavoidably yields nonlocality of the density. The refined κ' values are sometimes much smaller than one, implying diffuse aspherical density and overlapping basis functions. The calibration of these parameters by fitting to ab initio densities[103] can help standardize the experimental bond topological values. In the κ'-restricted multipole model (KRMM), proposed by Abramov et al.[104] and systematically evaluated by Volkov et al.,[105] these parameters are obtained from a fit to periodic Hartree−Fock (PHF) or periodic density functional (PDFT) densities and fixed in the treatment of real data, leading to more reliable experimental estimates of molecular dipole moments.

B. Reproducibility of the Experimental Topology

The "absolute" calibration described above might work with error-free, simulated observations of, in principle, unlimited resolution, provided these data exhibit sufficient selectivity for all parameters to be determined. In reality, however, experimental data are limited and may contain information the model is not designed to account for in full detail. In this situation, though the accuracy cannot be evaluated, the repeatability and reproducibility of the estimates can still provide a basis for relative calibration of the experiment.

To have statistical significance, a reliability evaluation must be based on a sufficiently large sample of estimates obtained from different experiments performed under systematically varied conditions. Such studies, especially those focusing on BCP properties, are not available. However, the analysis of the results obtained for comparable bonds in different molecules helps to identify the limitations of the experimental method.

1. Amino Acids and Oligopeptides

Amino acids have been extensively studied with the aim of exploring the transferability of electronic properties of chemically equivalent atoms and functional groups. Table 2 summarizes the experimental $\rho(\mathbf{r}_{BCP})$ and $\nabla^2\rho(\mathbf{r}_{BCP})$ values of bonds common to 11 amino acids (L-alanine,[96] DL-aspartic acid,[106] DL-proline,[38] L-asparagine, DL-glutamic acid, DL-serine, L-threonine,[107] L-arginine,[108] L-cystine,[109] α-glycine,[110] and DL-histidine[111]) and the related compound L-Dopa,[100] obtained independently in five laboratories under different experimental conditions and with different refinement strategies. The source of radiation applied (synchrotron radiation, Mo Kα or Ag Kα), the temperature maintained (20−100 K), and the detector used (conventional scintillation counter, solid state or CCD) during the data collection are the most important variables in the comparison. One should

Table 2. Topological Properties of Selected Bonds in Amino Acids[a]

	C−O$_1$	C−O$_2$	C$_\alpha$−N	C-C$_\alpha$	C$_\alpha$−C$_\beta$
Ala(Mo)^0	2.86	3.02	1.70	1.76	1.67
NC 23	29.6	39.0	11.1	10.8	10.1
Asn(Syn)^0	2.74(4)	2.90(4)	1.74(3)	1.67(3)	1.85(3)
NC 100 1.46	34.3(2)	32.5(2)	13.6(1)	8.6(1)	16.1(1)
Asn(Syn)^0	2.63(2)	2.69(2)	1.67(3)	1.67(2)	1.62(3)
NC 110 1.12	29.6(1)	26.6(1)	8.6(1)	10.6(1)	10.1(1)
Arg(MO)^0	2.59	2.68	1.70	1.63	1.60
NC 130 1.20	23.7	23.7	8.3	11.2	11.6
Asp(Ag)^0	2.71(3)	2.87(3)	1.69(2)	1.69(2)	1.61(2)
C 20 1.37	37.6(2)	36.1(2)	12.9(1)	12.9(1)	12.1(1)
Cys(Mo)^0	2.65	2.86	1.54	1.76	1.68
NC 110 1.12	22.4	27.5	7.25	13.25	11.58
Glu(Syn)^0	2.53(4)	2.77(4)	1.72(3)	1.86(2)	1.68(2)
C 100 1.30	27.3(2)	33.9(3)	9.3(1)	14.5(1)	10.1(1)
Gly(Mo)^0	2.67	2.77	1.69	1.78	-
C 23 1.15	30.5	32.8	11.9	15.6	-
His(Mo)^0	2.66(3)	2.83(5)	1.61(1)	1.73(1)	1.56(1)
C 110 1.23	34.2(2)	37.8(2)	7.33(3)	13.24(4)	9.24(3)
Pro(Syn)^0	2.83(4)	2.84(4)	1.68(2)	1.88(2)	1.66(2)
C 100 1.12	39.3(3)	34.3(3)	9.7(1)	15.5(1)	11.5(1)
Ser(Syn)^0	2.70(3)	2.74(3)	1.69(2)	1.77(2)	1.79(2)
C 100 1.54	36.6(1)	35.7(2)	11.4(1)	13.4(1)	14.8(1)
Ser(Mo)^0	2.55(4)	2.67(4)	1.72(3)	1.86(3)	1.77(3)
C 100 1.22	32.0(3)	31.4(3)	16.9(2)	15.5(1)	14.4(1)
Thr(Ag)^0	2.64(4)	2.78(4)	1.72(3)	1.80(3)	1.80(3)
NC 25 1.34	30.7(3)	38.1(2)	13.2(1)	15.4(1)	13.8(1)
L-Dopa(Mo)^0	2.70(2)	2.84(2)	1.62(3)	1.71(1)	1.79(1)
NC 173 1.08	32.6(6)	38.8(4)	8.4(4)	12.02(1)	13.07(1)
average	2.68(9)	2.80(10)	1.68(5)	1.76(8)	1.70(9)
	31.5(4.9)	33.4(4.8)	10.7(2.8)	13.0(2.2)	12.2(2.1)

[a] Upper line, electron density at the BCP (e/Å^3); lower line, negative Laplacian at the BCP (e/Å^5). Entries in the first column of each row are as follows. First line: compound identification, radiation used; (Mo) Mo Kα, (Ag) Ag Kα, (Syn) synchrotron. Second line: (C) centrosymmetric, (NC) noncentrosymmetric; measurement temperature in K; resolution in $\sin(\theta)/\lambda$ (Å^{-1}). Numbers in parentheses are experimental standard uncertainties, except for the last row, where they represent root-mean-square deviations calculated for the sample.

also consider the differences in the chemical nature of the β-substituents, the molecular conformation, the crystal packing, and symmetry. Despite varying conditions, the results are fairly consistent, especially in terms of the $\rho(\mathbf{r}_{BCP})$ quantities, which appear to be statistically equal for the chemically equivalent bonds. The Laplacian is markedly less reproducible, in particular for the C−O bonds of the carboxylate group ($\nabla^2\rho(\mathbf{r}_{BCP})_{min} = 22.4$, $\nabla^2\rho(\mathbf{r}_{BCP})_{max} = 39.0$ e/Å^5). Its root-mean-square deviation, calculated for the sample for each bond, is an order of magnitude larger than the experimental standard uncertainties, which are affected by the extent to which correlations between LS variables are included in the calculation.

A series of experimental ED studies has been devoted to small peptides. The primary goal of these investigations was to explore the transferability of the pseudoatomic density in terms of multipole populations rather than in terms of topological descriptors. However, in a recent paper Pichon-Pesme et al.[112] summarize the results of topological analyses of peptide bonds in N-acetyl-L-tryptophane,[113] N-acetyl-α,β-dehydrophenylalanine methylamide,[114] leu-enkephalin,[115] triglycine,[116] N-acetyl-L-tyrosine ethylester monohydrate,[117] glycyl-L-threonine dihydrate,[118] glycyl-aspartic acid, and tyrosyl-glycyl-glycine.[112] In Table 3 average bond distances, BCP locations, $\rho(\mathbf{r}_{BCP})$, $\nabla^2\rho(\mathbf{r}_{BCP})$, and ϵ values are repro-

Table 3. Topological Indices of the Bonds in a Peptide Unit Averaged over a Series of Experimental Determinations (Refs 112−118)[a]

	C1A−C1	C2A−N2	C1−N2	C1=0
distance (Å)	1.518(11)	1.447(11)	1.338(5)	1.236(5)
d_1 (Å)	0.76(3)	0.62(2)	0.55(1)	0.48(2)
	0.78	0.63	0.54	0.52
d_2	0.76(4)	0.83(2)	0.79(1)	0.76(2)
	0.75	0.82	0.79	0.72
$\rho(\mathbf{r}_{BCP})$ (e/Å^3)	1.70(5)	1.8(1)	2.4(1)	2.8(1)
	1.76	1.92	2.43	2.89
$\nabla^2\rho(\mathbf{r}_{BCP})$ (e/Å^5)	−12.7(9)	−10.2(2.3)	−23.4(3.2)	−26.1(3.8)
	−14.4	−13.2	−28.6	−31.3
ϵ	0.14(6)	0.10(3)	0.21(8)	0.10(5)
	0.12	0.11	0.24	0.14
no. of bonds	17	16	17	17

[a] Atomic numbering as defined in Scheme 3. d_1 and d_2 are the distances of the BCP from the first and second atom, respectively. First line: experimental. Second line: theoretical.

duced for the four bonds in the peptide link (**3**, Scheme 3). These parameters are based on the same

Scheme 3
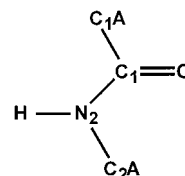
interpretation of different data sets, that is, the same level of extension of the multipole model and the same refinement strategy. Of the four topological indices, the BCP locations and $\rho(\mathbf{r}_{BCP})$'s spread over a narrow range. The standard deviations of $\nabla^2\rho(\mathbf{r}_{BCP})$ values increase with the bond polarity but are smaller than those found for amino acids. The bond ellipticity is the least reproducible descriptor and does not appear to be accessible from these studies. The observation that a standardized interpretation of X-ray data of chemically analogous systems yields almost identical BCP locations in equivalent bonds (and thus identical partitioning) suggests transferability of AIM properties.

Duplicate measurements available for the noncentrosymmetric structures of glycyl-L-threonine[118,119] and L-asparagine monohydrate[107,120] provide a unique opportunity for a direct comparison of the results. For glycyl-L-threonine,[118] refinement of the Mo Kα data collected at 110 K with a scintillation counter up to a resolution of $\sin\theta/\lambda = 1.20$ Å^{-1}, followed a block-diagonal refinement strategy in which the exponents of the deformation radial functions (κ'), were also included. The fact that the disorder of the O atom of one of the water molecules in the unit cell was not resolved had only a minor influence on the BCP properties. In a second study,[119] based on a 100 K CCD-synchrotron data extended up to $\sin\theta/\lambda = 1.32$ Å^{-1}, the κ' parameters were fixed at 1.0. The comparison of the results yields 99%, 95%, and 88% correlation for $\rho(\mathbf{r}_{BCP})$, $\mathbf{r}_{BCP}$, and $\nabla^2\rho(\mathbf{r}_{BCP})$, respectively, the bond-parallel curvatures showing the largest discrepancies (correlation $r[\lambda_3] = 0.65$). However, all BCP properties based on the former measurement are significantly lower in value than those from the latter study.

A similar conclusion on the effect of the treatment of κ' on the curvature parallel to the bond can be drawn from comparison of results for L-asparagine. In the treatment of a $\sin\theta/\lambda < 1.07$ Å^{-1} data set,[120] the KRMM was implemented, while in the analysis of a somewhat more extended data set,[107] the exponents of the deformation radial functions were not refined. Here again, all bond indices except λ_3 show high correlation: $r[\rho(\mathbf{r}_{BCP})] = 0.99$, $r[\nabla^2\rho(\mathbf{r}_{BCP})] = 0.95$, $r[\lambda_1] = 0.96$, $r[\lambda_2] = 0.91$, but $r[\lambda_3] = 0.88$.

These comparisons indicate that the κ' parameters, as expected, affect the fine details of the topology of the bond densities and that assessment of the quality and bond analysis in general should include not only the Laplacian but all principal curvatures of ρ. When this is done, as Arnold et al.[120] point out, "fortuitous error cancellation is less likely to occur". The authors use the H tensors ($H_{ij} = [\partial^2\rho/\partial x_i\partial x_j]_{BCP}$) in an icosahedral representation that provides a simple way to compare not only their magnitude but also their orientation. Surprisingly, a better correlation between theory and experiment was obtained for each of the six components of the transformed tensors than for the three principal curvatures.

2. Model Ambiguities

As argued in the foregoing section, the reproducibility of the diffraction measurement is a necessary but not a sufficient condition for the reproducibility of different measurands. Due to recent advances in instrumentation, data quality is less of an issue. Though the reproducibility of the experiment remains of crucial importance, the recurrent problem of parameter uncertainties and indeterminacies in the model is receiving renewed attention. It is important, in this respect, to differentiate between uncertainties due to model inadequacies and uncertainties due to model ambiguities. The multipole model has been proven to be basically adequate, but no recipe exists for an unambiguous selection of the LS variables. In careful studies, more often than documented, a "trial-and-error" approach is followed in which several variable-parameter choices are "challenged" for their performance in the fit and for the physical relevance of their estimates. A good fit ensures neither "reasonable" estimates nor efficient data prediction. The intrinsic property of an LS solution that it is based on a particular hypothesis seems to be forgotten and rediscovered from time to time. Though the test of the solutions in parameter space is of paramount importance, it has limited selectivity because of its statistical nature. The deformation density projects the solution into real space and thus can provide a test of chemical significance, but its quantitative interpretive power is limited. The derivatives of ρ, on the other hand, are not only highly sensitive to local changes in the model ED, but are physical descriptors of fundamental nature. That is why topology analysis can be considered as an important tool of solution screening.

The indeterminacy in the parameter estimates ("nonuniqueness" of the LS solution) was addressed in the study of ammonium dihydrogen phosphate (NH$_4$H$_2$PO$_4$).[121] The compound crystallizes in a non-centrosymmetric space group ($P2_12_12_1$). The positional and thermal parameters of the heavy atoms were obtained from a refinement against high-order data, while those of the H atoms were from a neutron diffraction measurement. All conventional parameters were fixed in the fit of the static density described up to the hexadecapolar (N and P atoms), octupolar (O atom), and quadrupolar (H atoms) level of the multipole expansion. To eliminate correlation, these variables were grouped into four sets (5κ, $5P_v$, $39P_{lm}$, and $5\kappa'$), each of which was separately refined and reiterated until convergence was reached. First, no restriction on the charge transfer between the anion and cation was imposed; then, in subsequent refinement cycles, the total charges of both ions were fixed at different values ($0.1e$, $0.3e$, $0.5e$, $0.7e$, $1.0e$ net charge on the cation). In all cases the unit cell was maintained neutral (i.e., the anion had the opposite charge of the cation). The refinement allowing for free charge transfer led to a cation–anion charge separation of $0.1e$, to be compared with the formal value of $1e$. The charge-restricted models resulted in statistically equivalent fits and parameter estimates, except for the charges and monopole deformations (different κ values) of the H atoms. It is thus not surprising that the topology of the $P-O$ bond remained unaltered. On the other hand, the LS solutions associated with different, preassigned κ' values for the P atom led to significantly different $\nabla^2\rho(\mathbf{r}_{BCP})$ and λ_3 estimates for the $P-O$ bond but again without any statistically detectable change in the quality of the fit. This correlation was found to be independent of the amount of charge separation, either constrained or varied.

Thermal motion effects were analyzed in the 15 K study of the non-centrosymmetric structure of potassium hydrogen(+)-tartrate.[122] The main issue considered concerns the extent to which LS constraints, which enhance the physical significance of the ADPs, can reduce bias in the experimental static ED and its topological features. To elucidate the effect of "rigid-bond"- and "rigid-link"-type restrictions, the BCP properties of the static densities, as extracted by using different subsets of the data, with cutoff values of 0.85, 1.08, and 1.27 Å^{-1} in $\sin\theta/\lambda$ and different refinement models, were compared. In the restricted model, ADPs corresponding to the internal vibrational modes, generated from an ab initio HF/6-311** harmonic force field for the isolated molecule, were used as starting parameters. In each refinement cycle shifts were constrained to fulfill the rigid-body motion requirement.[64] The unconstrained refinement, even with the use of all measured data ($\sin\theta/\lambda = 1.27$ Å^{-1}), biased the ADPs, especially for the O atoms of the carbonyl bonds, the resulting $\Delta(C-O)$ values being 4–10 times larger than the theoretical ones. The inadequate deconvolution of thermal motion affected the topology of the $C-O$ bond in the carboxylate group most, as is evident from the $\nabla^2\rho(\mathbf{r}_{BCP})$ value along the BP and the VSCCs of the O atom as functions of data extension used in the fit (Figure 5a). A considerable shift of the BCP toward the C atom occurred as more high-order data were included. This shift was accompanied by an increase in the absolute
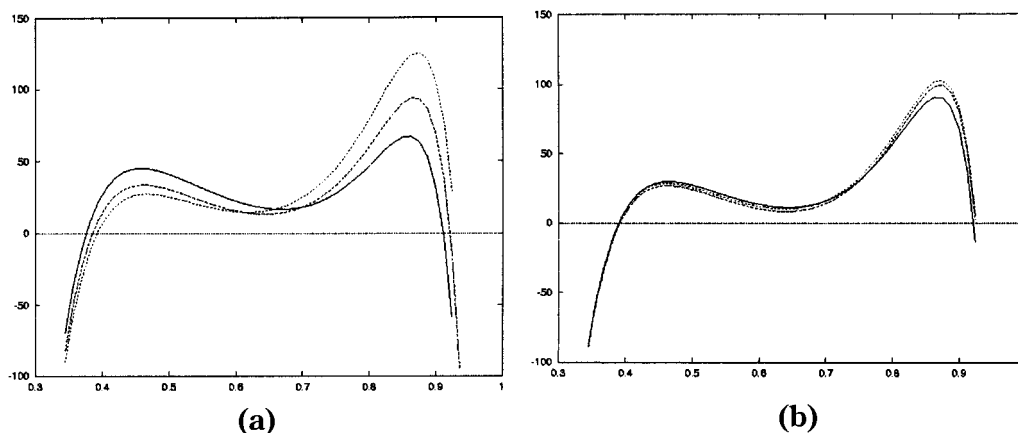
(a) (b)

Figure 5. Experimental negative Laplacian function (vertical axis) along a C=O bond path (horizontal axis) of the carboxylate group in potassium hydrogen(+) tartrate obtained by refinements against data of different resolutions: $\sin(\theta)/\lambda \leq 1.27$ Å^{-1} (—), $\sin(\theta)/\lambda \leq 1.09$ Å^{-1} (- - -), and $\sin(\theta)/\lambda \leq 0.85$ Å^{-1} (· · ·); unconstrained refinement (a) and with rigid-bond constraint (b). Units are e and Å.[122]

value of $\nabla^2\rho(\mathbf{r}_{BCP})$ and by a drastic change in the location and size of the bonded VSCCs. When only the low-order data were fitted, the bonded VSCC of the C/O atoms increased/decreased by about 100% compared to the values obtained by the full-data fit. This trend was eliminated by the use of the rigid-bond constraints, which removed the correlation between ADPs and static density parameters, and led to topological indices insensitive to the data resolution (Figure 5b), thus demonstrating the value of including theoretical information on intramolecular vibrations in the charge-density analysis.

C. Applications to Molecular Crystals

Since 1995, numerous applications of the AIM concept to multipole-modeled experimental densities have been reported. Despite the issues addressed in the foregoing paragraphs, the general outcome of these studies have provided relevant, and sometimes unique, chemical information. We review them here in a systematic manner with the intention of elucidating chemical trends rather than following the actual chronological order in which they have been published.

The descriptive power of the topological analysis of the ED is well demonstrated by the 110 K study of 7-dispiro[2.0.2.1]heptane carboxylic acid (**4**, Scheme 4).[123] The three-membered rings in this triangulane exhibit features expected on the basis of bent bonds

Scheme 4

4
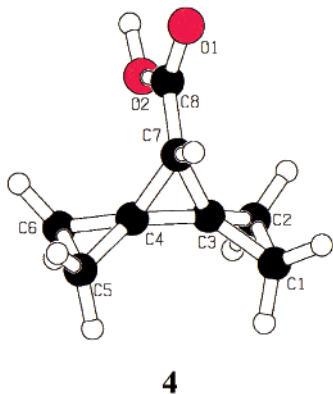
with strong π-character and charge buildup in the center of the rings. The analysis of the experimental Laplacian reveals that (i) the extent of σ-delocalization (charge shift into the ring's plane) in the central ring is smaller than that expected for cyclopropane—a feature attributed to the effect of *spiro*-conjugation and of the presence of a π-acceptor substituent, (ii) the bonded VSCC of the *exo* atoms in the terminal rings are more pronounced than those of the *endo* atoms—an asymmetry also attributed to the effect of the carboxyl group, (iii) the BCPs of proximal bonds are shifted not only outward from the bond line but also along it, away from the *spiro* atoms in the terminal rings but toward the spiro atoms in the central ring.

1. Aromaticity in Carbon-Based Ring Systems

A new structural feature of the ring system in annulene emerged from the topological analysis of the experimental ED of *syn*-1,6:8,13-biscarbonyl[14]-annulene (**5**, Scheme 5).[2] In the usual description,

Scheme 5

5
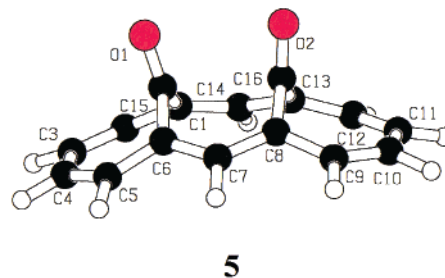
this molecule is considered as a fusion of two lateral, seven-membered rings via a central eight-membered ring. The multipole density, derived from high-resolution 19 K data, exhibits an extra BCP between the two bridge-carbon atoms C15 and C16 involved in the central ring (Figure 6). On the basis of the bond indices ($R = 2.593$ Å, $\rho(\mathbf{r}_{BCP}) = 0.116(3)$ e/Å^3, and $\nabla^2\rho(\mathbf{r}_{BCP}) = 1.53(1)$ e/Å^5) [for the sake of brevity, the units of $\rho(\mathbf{r}_{BCP})$ and $\nabla^2\rho(\mathbf{r}_{BCP})$ will be omitted from here on], the interaction can be characterized as closed-shell type most likely of steric origin. The
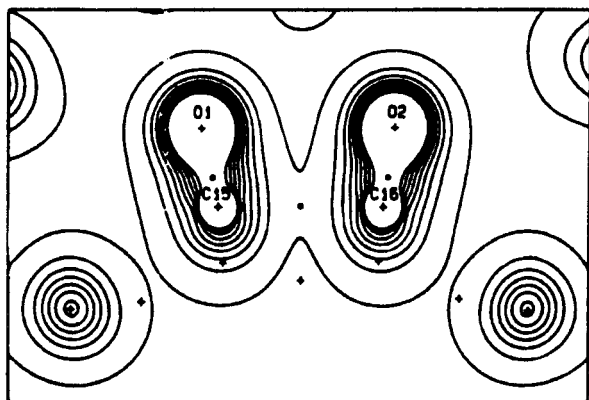
Figure 6. Transannular critical point in *syn*-1,6:8,13-biscarbonyl[14]-annulene. (Reprinted with permission from ref 2. Copyright 1995 International Union of Crystallography.)

topological consequence of this extra BP is the presence of two RCPs associated with the two five-membered rings formed by the cross-ring interaction. These saddle points were located supporting the internal consistency of the ED. It is important to note that no BCPs could be found along the transannular lines connecting the atoms C1 with C6 and C8 with C13, though the corresponding distances are shorter (by about 0.1 Å) than the distance between the bridge atoms. This eliminates the argument that the extra BCP formation is solely of geometrical nature. The result demonstrates the interpretive power of the topological method in the classification of molecular structures. It is also a warning against blindly following the standard practice in crystal structure determination: knowledge of nuclear positions does not necessarily imply knowledge of the full chemical structure as implied by the topology of the ED.

Citrinin (**6**, Scheme 6) is a molecule with a diversity

Scheme 6
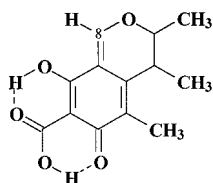
of chemical bonds. The main skeleton is composed of two six-membered rings (dihydropyrane condensed with a quinomethide). The adjacent alcoholic, carboxyl, and carbonyl substituents of the latter ring form a cooperative intramolecular hydrogen-bond

Scheme 7
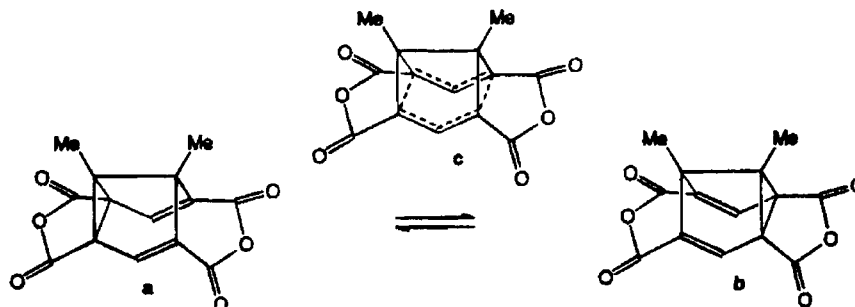
system of two fused rings. This almost planar arrangement seems to be supported by π-delocalizations extended along both sides of the ring's skeleton. The hydrogen bonds have short O⋯O distances in the range of 2.329(8) and 2.423(9) Å.

The experimental ED based on 19 K X-ray[124] data shows a high degree of internal consistency revealed in a variety of topological values. The conjugated bond system can be identified in terms of a linear variation of $\rho(\mathbf{r}_{BCP})$ as a function of the bond path length for the 13 C−C bonds in the molecule. On the basis of $\rho(\mathbf{r}_{BCP})$, double and single bond character can be assigned to three and five bonds, respectively, while the remaining five bonds form an intermediate class between the first two sets. Further information on this conjugation is provided by the analysis of the principal curvatures at the BCPs. As the $\rho(\mathbf{r}_{BCP})$'s increase on passing from the single to double bonds, so do the ϵ's, reflecting both an increased charge contraction toward the corresponding BPs and enhanced π-bond character. The angles between the eigenvectors associated with the major curvatures λ_2 of adjacent bonds amount to less than 20° along the conjugated framework. This indicates that the major axes for all conjugated bonds are aligned perpendicular to the ring system.

One of the most interesting aspects of this study is that not only static but also reactive properties of the molecule could be deduced from the topology of the experimental ED. The display of the reactive surface of the molecule, in terms of the $\nabla^2\rho = 0$ isosurface, predicts the carbon atom (C8), which forms the double bond and is adjacent to the oxygen atom in the dihydropyrane ring, to be the most likely center for nucleophilic attack. This finding is in complete agreement with the chemical behavior of the molecule. The mechanism of the reaction, yielding an alcohol upon treating citrinin with alkali, is based on the electrophilic character of the carbon atom in question.

Semibullvalene and its derivatives undergo a Cope rearrangement through a homoaromatic transition state (**7**, Scheme 7).[125] It has been predicted that the energy barrier to this valence isomerization can be lowered by electron-donating/withdrawing substituents attached symmetrically to the semibullvalene nucleus at the 1 and 5/2, 4, 6, and 8 positions and that the substituent effects can result in a homoaromatic ground state.[126] Theoretical calculations using correlated ab initio and DFT methods concluded that this is the case for 1,5-dimethyl-2,4,6,8-semibullvale-
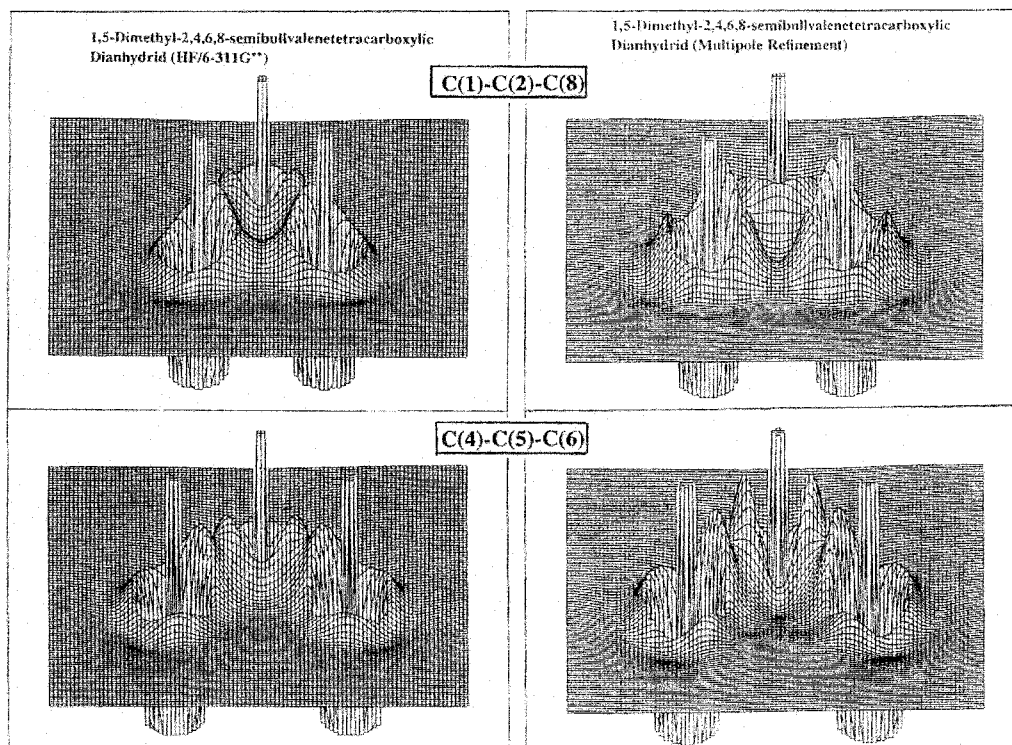
Figure 7. Negative Laplacian of theoretical (left) and experimental (right) densities of 1,5-dimethyl-2,4,6,8-semibullvale-netetracarboxylic dianhydride in the plane of the C(1)−C(2)−C(8) and C(4)−C(5)−C(6) atoms. In the theoretical result the first three atoms form a ring structure, with three BCPs and one RCP. All BCPs, including that associated with the C(2)−C(8) interaction, lie in regions of negative Laplacian. No BCP is found between the C(4) and C(6) atoms in the experiment; the Laplacian is flat in that region, and no bonded VSSCs are present.[128]

netetracarboxylic dianhydride (**7**).[127] In support of this prediction are the solid (^{13}C CP-MAS) and the solution-phase (^{13}C) NMR spectra, neither of which show temperature dependence over the range of 298−183 and 293−223 K, respectively. However, X-ray diffraction studies reveal that the C_2 symmetry, characteristic for the homoaromatic system and apparent for the molecular structure at 293, 243, and 163 K, is broken at lower temperatures.[128] The C2−C8 and C4−C6 distances, associated with forming and breaking of the corresponding cyclopropane rings, respectively, continuously decrease and increase as the temperature is lowered further (R(C2−C8) = R(C4−C6) = 1.966(3) Å at 163 K, R(C2−C8) = 1.6674(12) Å and R(C4−C6) = 2.2051(12) Å at 15 K). This observation indicates that the structures derived at ambient temperatures correspond to a superposition of the two, nondegenerate valence isomers rather than to a homoaromatic ground state. The analysis of the ADPs obtained by the multipole refinement using the 15 K data shows no recognizable sign of a disordered structure. Neither does the experimental geometry, which is in fair agreement with that derived by geometry optimization at the HF/6-311G** level (R(C2−C8) = 1.602 Å; R(C4−C6) = 2.237 Å; unlike the theoretical methods referred to above, the HF theory predicts the homoaromatic state to be a transition state, not the ground state). Nevertheless, only the topological analysis of the experimental ED provides definite evidence that only one tautomer occurs at 15 K. In agreement with the result based on the wave function, no BCP is found between the C4 and C6 atoms, while the other bond shows the expected covalent character ($\nabla^2\rho(\mathbf{r}_{BCP})_{exp}$

= 1.38(3), $\nabla^2\rho(\mathbf{r}_{BCP})_{theo}$ = 1.36). The experimental and theoretical Laplacians are shown in Figure 7.

The temperature dependence of the relative populations of the tautomers can be monitored by the change in the relevant distances, and the resulting relationship can be used to estimate the equilibrium constant of the Cope process and of the difference in free energy of the tautomers in the solid state (ΔG° = 0.162 kcal/mol).

2. Nitrogen-Containing Compounds

The characterization of the electronic structure of the trimethylamine nitroimide (**8**, Scheme 8) mol-

Scheme 8
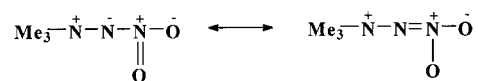
ecule possessing three connected N atoms in completely different bonding environments is a challenge for assessing the descriptive power of the topological method. According to the formal picture of the bonding, both $N-N$ bonds should have considerable ionic character due to the terminal quaternary ammonium and nitro groups. On the other hand, the nonbonding electrons of the central N atom are expected to delocalize into the π-system of the nitro group. Low-temperature X-ray analysis[129] shows that the backbone of the molecule occupies a crystallographic mirror plane with two symmetry-related methyl groups completing the structure. The length of the N^+-N bond on the left of the diagram is at 1.472(1) Å, comparable to the value characteristic for

a single bond, while the N−N(O$_2$) bond length (1.315-(2) Å) is shorter. This, together with the planar arrangement, supports π-delocalization. For the former bond, the BCP is located in a region of relatively high density ($\rho(\mathbf{r}_{BCP})$ = 1.90(3)), but of a low charge accumulation ($\nabla^2\rho(\mathbf{r}_{BCP})$ = −2.51(8)), while the latter bond appears to have a strong covalent (double bond) character ($\rho(\mathbf{r}_{BCP})$ = 3.45(5)), $\nabla^2\rho(\mathbf{r}_{BCP})$ = −30.6(2), and ϵ = 0.53). The Laplacian distribution around the central N atom shows only one nonbonded VSCC, which gives further evidence for the resonance form on the right of Scheme 8 being more representative than that on the left-hand side of the diagram. The intramolecular BCP between the terminal H and O atoms in the molecular main plane ($\rho(\mathbf{r}_{BCP})$ = 0.17-(1), $\nabla^2\rho(\mathbf{r}_{BCP})$ = 1.65(1)) explains the stabilization of the *cis*-conformation via an intramolecular C−H⋯O hydrogen bond.

The antifungal activity of protonated polyamines is interpreted as an electrostatic interaction of these cations with the negatively charged phosphate groups of DNA. Thus, the knowledge of the distribution of charge in these systems, in particular the potential surface of the polyamine, can help explain their biological activity. The [PF$_6$]$^-$ salt of *E*-tetraethyl-1,4-diammoniumbut-2-ene (**9**, Scheme 9) can be consid-

Scheme 9
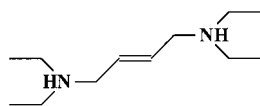
ered as a model system. The 100 K X-ray structure determination established that the asymmetric unit contains one-half of the cation, a center of inversion being located at the midpoint of the C=C double bond in the monoclinic unit cell.[130] The leading forces of the crystallization are most likely N−H⋯F-type hydrogen bonds. The experimental $\rho(\mathbf{r}_{BCP})$ values for all bonds are uniformly higher than those obtained at the HF/6-311** level, while the $\nabla^2\rho(\mathbf{r}_{BCP})$ values are lower than the theoretical results. The BCP properties confirm the expected difference in bond order between the C=C and C−C bonds. The C−N bonds appear to be of equal strength in terms of the charge concentration based on the experimental $\nabla^2\rho(\mathbf{r}_{BCP})$ (−23 on average), while the corresponding theoretical values (−5.3 and −5.8) suggest the two N−C(ethyl) bonds to be different from the N−C-(butene) bond (−10.8).

Because of the current interest in modeling of biochemical processes, accurate evaluation of electrostatic properties of nucleic acids is of paramount importance. Numerous experimental investigations have aimed at the determination of the distribution of charge in related molecules. Detailed topological studies are available for nitrogen-containing aromatic systems such as imidazole, triazole, pyrimidine, and pyridine derivatives. Common to these investigations is the attempt to gain information on the aromatic character or the extent of conjugation in the heter-orings. The comparison of the results is rather inconclusive, mainly because the usual bond topological indices alone do not seem to provide a consistent

description of aromaticity that involves electron delocalization and thus must be formulated in terms of collective rather than local parameters. As emphasized by Howard and Krygowski[131] in their theoretical investigation on benzenoid hydrocarbons, ED descriptors evaluated at the ring CP seem to be the natural choice for such a purpose, since increased aromaticity corresponds to increased contraction of the electron density into the ring plane. Nevertheless, in the studies discussed below, ring properties have not been used to describe aromaticity.

From the comparison of topological features of experimental EDs, obtained by combined X-ray and neutron diffraction studies of two five-membered nitrogen heterocycles, imidazole[94] and triazole,[65] the following points emerge. The $\rho(\mathbf{r}_{BCP})$ values, averaged over the four C−N bonds, amount to 2.20 for the former and 2.26 for the latter molecule. Judging from their estimated standard uncertainties, these quantities are statistically equal (the largest deviation from the sample means are 0.07 and 0.12, respectively). On the basis of the individual $\rho(\mathbf{r}_{BCP})$ values, none of the bonds can be considered as clearly double or single, which suggests that both rings are aromatic. However, the picture based on the $\rho(\mathbf{r}_{BCP})$'s is not supported by the $\nabla^2\rho(\mathbf{r}_{BCP})$'s and ϵ's, which show hardly any trend. An interesting result of the triazole study is the equivalence of the two bonds in the N1−C5=N4 skeleton (C5−N1: R = 1.3311(7) Å, $\rho(\mathbf{r}_{BCP})$ = 2.26, $\nabla^2\rho(\mathbf{r}_{BCP})$ = −19.5. C5=N4: R = 1.3307(7) Å, $\rho(\mathbf{r}_{BCP})$ = 2.27, $\nabla^2\rho(\mathbf{r}_{BCP})$ = −21.2). This is characteristic of a structure intermediate between the possible tautomers (**10**, Scheme 10). Since in the crystal the

Scheme 10
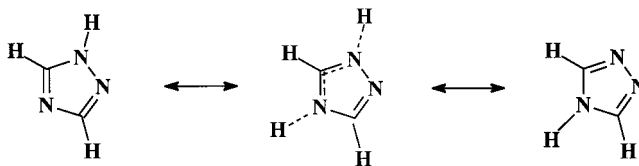
two terminal N atoms are donors and acceptors in strong hydrogen bonds, the crystalline environment can be considered as balancing the bonds and enhancing the aromatic character of the rings. A very similar situation occurs in the imidazole ring in which the BCP properties of the formal double bond do not differ markedly from those of the single bond (C2−N3: R = 1.325 Å, $\rho(\mathbf{r}_{BCP})$ = 2.27, $\nabla^2\rho(\mathbf{r}_{BCP})$ = −15.0. C2−N1: R = 1.348 Å, $\rho(\mathbf{r}_{BCP})$ = 2.20, $\nabla^2\rho(\mathbf{r}_{BCP})$ = −19.8).

On the basis of experimental BCP properties of 4-cyanoimidazoleium-5-olate,[132] the molecule can formally be described as two conjugated systems (N1−C2−N3 and O8−C5−C4−C6−N7) linked by single C−N bonds (C4−N3: $\rho(\mathbf{r}_{BCP})$ = 2.05(6), $\nabla^2\rho(\mathbf{r}_{BCP})$ = −16.4(17). C5−N1: $\rho(\mathbf{r}_{BCP})$ = 2.03(6), $\nabla^2\rho(\mathbf{r}_{BCP})$ = −19.8(18)). This feature could also be attributed to the effect of the crystal environment, since each of the N atoms of the N−C−N skeleton is involved as a donor in strong hydrogen bonds.

In 9-methyladenine, the experimental $\rho(\mathbf{r}_{BCP})$'s for the 10 C−N bonds cover a larger range (1.91−2.73) but their variation is not consistent with that of the

bond ellipticities (0.14−0.28).[94] For the imidazole ring in 9-methyladenine, taking the N−CH$_3$ bond as a "prototype" of the single bond in adenine ($\rho(\mathbf{r}_{BCP}) = 1.91$), a picture consistent with that depicted in Scheme 11 (**11**) emerges. The ED of the pyrimidine

Scheme 11
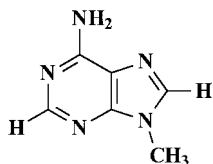
ring seems to be more delocalized than that of the imidazolee. The highest $\rho(\mathbf{r}_{BCP})$ value is associated with the formal C=N double bond in the imidazole ring. This bond appears to be more localized in adenine than the corresponding bond in imidazolee.

The BCP parameters obtained for 1-methyluracil by the X + N method (123 K) suggest extended conjugation over the pyrimidine ring[133] ($2.01(8) < \rho(\mathbf{r}_{BCP}) < 2.29(8); -22.7(27) < \nabla^2\rho(\mathbf{r}_{BCP}) < -16.7(24)$). The C−N bonds in the ring can be characterized as strong, shared interactions ($\rho(\mathbf{r}_{BCP})_{ave} = 2.22$, $\nabla^2\rho(\mathbf{r}_{BCP}) = -19.7$) compared to the more polar N−C(Me) *exocyclic* single bond. The *C−C* bonds in the ring are of intermediate type; the formal single bond possesses only slightly lower $\rho(\mathbf{r}_{BCP})$ than the formal double bond. The expected differences are more pronounced in terms of the ϵ values.

The molecule of 2-pyridone can be considered as a model system of biological processes involving proton transfer via tautomerism (**12**, Scheme 12). In the

Scheme 12
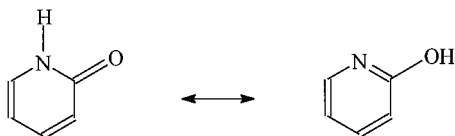
solid phase at 123 K, the *lactam* form is favored (**12**, left). The planar molecules are linked via N−H⋯O hydrogen bonds into puckered chains along the *c*-axis in an orthorhombic unit cell.[134] The $\rho(\mathbf{r}_{BCP})$'s of the *C−C* bonds in the pyridine ring are higher than expected for the formally single bonds and lower than for the double bonds, but consistent with the magnitude of the differences in the bond lengths. In addition, a statistically uniform distribution of the ellipticities among C−C and C−N bonds is found. Thus, all indications point to π-delocalization over the entire ring, that is, a tendency toward the *lactim* tautomer (**12**, right), in agreement with the intermolecular hydrogen-bonding pattern.

3. Sulfur-Containing Compounds

The molecule of 3,3,6,6-tetramethyl-*S*-tetrathiane (**13**, Scheme 13) of D_2 symmetry (twist-boat conformation) lies along the diagonal 2-fold axis of a tetragonal unit cell with the ring's carbon atoms located on the axis.[135] Experimental and theoretical $\rho(\mathbf{r}_{BCP})$ values for the S−S and S−C bonds are in fair agreement (S−S: $R = 2.023(1)$ Å, $\rho(\mathbf{r}_{BCP})_{exp} =$

Scheme 13
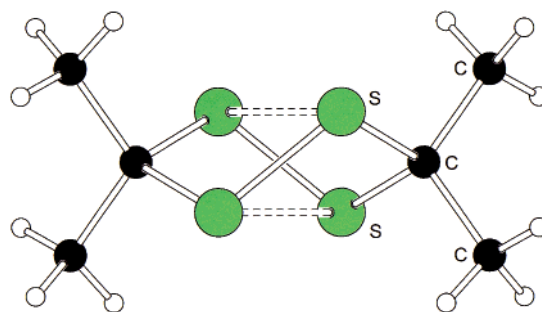
13

1.13(3), and $\rho(\mathbf{r}_{BCP})_{theo} = 1.09$. S−C: $R = 1.847(1)$ Å, $\rho(\mathbf{r}_{BCP})_{exp} = 1.33(3)$, and $\rho(\mathbf{r}_{BCP})_{theo} = 1.23$), but considerable discrepancies for the corresponding $\nabla^2\rho(\mathbf{r}_{BCP})$ quantities are found. The most striking result is that the molecular graphs obtained by the two methods are different. The experimental ED exhibits a BP network consistent with the full lines in the graph depicted in Scheme 13 (**13**). The neighboring molecules in the crystal are connected via S⋯S intermolecular BPs ($R = 3.669(2)$ Å, $\rho(\mathbf{r}_{BCP}) = 0.04$, $\nabla^2\rho(\mathbf{r}_{BCP}) = 0.44$). In the theoretical ED of the isolated molecule, on the other hand, two BPs corresponding to trans-annular, intramolecular S⋯S interactions of closed-shell type are present (as indicated by the broken lines in Scheme 13) ($R = 3.150$ Å, $\rho(\mathbf{r}_{BCP}) = 0.12$, $\nabla^2\rho(\mathbf{r}_{BCP}) = 1.45$). Accordingly, four RCPs (corresponding to the four four-membered rings formed in such a way) and one CCP can be located. The authors mention the possibility that the intermolecular S⋯S contacts present in the crystal destabilize the intramolecular interactions across the ring. However, in the case of tetrasulfur−tetranitride,[136] the topological analysis of both experimental and theoretical densities locate BCPs between the (much closer) proximal S atoms across the ring ($R_{ave} = 2.5972(2)$ Å, $\rho(\mathbf{r}_{BCP})_{ave} = 0.37(1)$, $\nabla^2\rho(\mathbf{r}_{BCP}) = 1.61(1)$, experimental values) (Figure 8), despite the relatively
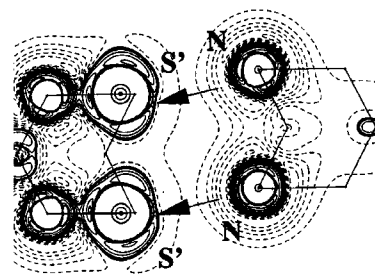

Figure 8. Experimental contour plot of the negative of the Laplacian in the NNS'S' plane of two neighboring molecules in crystals of tetrasulfur tetranitride. Arrows mark the "key−lock" arrangement of valence-shell charge concentrations-depletions on neighboring N and S atoms. (Reprinted with permission from ref 136. Copyright 2000 The Royal Society of Chemistry.)
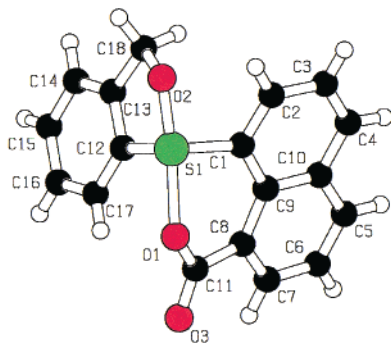
strong S⋯N intermolecular interactions ($R = 3.0882(8)$ Å, $\rho(\mathbf{r}_{BCP})_{ave} = 0.09(1)$) that seem to stabilize the crystal. A pair of S⋯N contacts link the molecules in such a way that helical chains along the crystallographic *b*-axis are formed. The Laplacian distribution in the plane of the interacting atoms reveals key-lock arrangement of the VSCC of the

N and *S* atoms, in which charge concentration in the valence shell of the N atom faces the charge depletion in the valence shell of the S atom. The S−N bonds appear to be polarized and possess considerable π-character ($R_{ave} = 1.629(1)$ Å, $\rho(\mathbf{r}_{BCP})_{ave} = 1.54(1)$, $\nabla^2\rho(\mathbf{r}_{BCP})_{ave} = -10.6(1)$, $\epsilon_{ave} = 0.17$). The corresponding BPs are inwardly bent, while those for the S···S interactions are displaced outward from the CCP.

For the description of molecules for which electron-counting models fail to account for the complete bonding situation, the concept of hypervalency has been invoked.[137] A representative example is a tetracoordinate sulfur compound that possesses a regular or distorted trigonal-bipyramidal geometry with a linear $X-S-Y$ arrangement of the axial substituents and a lone pair completing the five-coordination. In this case, the coordination number of the central S atom is larger than the number of valence electron pairs available in the orbital model. These bonds are significantly longer than those of the corresponding single bonds, and their strength is controlled by the electronegativity of the X and Y ligands. Structural studies on representative sulfuranes and sulfonium salts have revealed a wide range of S−O interactions in $-O-S-O-$ systems and showed that with increased polarity of one of the bonds, the other gains substantial covalent character.[138] In an extreme case, the three-center system splits into a covalent bond and a weak $S···O$ interaction.

The molecule of diaryl(alkoxy)(acyloxy)spiro-λ^4-sulfane (**14**, Scheme 14) represents an intermediate,

Scheme 14

14

asymmetric $O-S···O$ system. The asymmetric unit contains also one-half a molecule of dioxane (at a special position), the oxygen atom of which (O_d) is connected via an intermolecular interaction to the sulfur atom. The S−O bond distances based on high-resolution X-ray data[139] are 1.694(2) (S−O), 2.045(2) (S···O), and 3.054(2) Å (S···O_d). The topological analysis of the experimental ED has led to bond indices that clearly differentiate between these bonds. The shortest bond has the highest $\rho(\mathbf{r}_{BCP})$ value (1.26-(1)); the BCP lies in a region of charge concentration ($\nabla^2\rho(\mathbf{r}_{BCP}) = -0.5(1)$) and thus can be characterized as a polarized, weak covalent bond. Both longer bonds have lower $\rho(\mathbf{r}_{BCP})$ and positive $\nabla^2\rho(\mathbf{r}_{BCP})$, suggesting a closed-shell interaction with appreciable ionic character. The VSCC of the central S atom is clearly separated from the VSCCs of both O atoms. In

contrast to this situation, the VSCCs of the S and C atoms overlap in the equatorial plane. All of these finding are in fair agreement with those obtained at the HF/6-311G**(2df,2p) level of theory.

The need for the concept of hypervalency and related questions, such as the role of the d orbitals in the description of the electronic structure of these molecules as well as the covalent versus ionic character of the S−O bonds, have been critically examined by Cioslowski et al.[140] The authors emphasize the advantages of using "observable-based interpretative tools" in characterizing these systems.

4. Carboranes

The structure prediction power of the AIM theory is of particular importance in describing other electron-deficient molecules, such as boranes and carboranes. As the topological study by Bader and Legare[141] demonstrates, ring formations play an important role in the stabilization of these systems. In other words, the charge delocalization over the ring surfaces and charge accumulations in the bonds contribute to a comparable extent to the stability of the structure. According to the formal valence electron rule, 1,5-dicarba-*closo*-pentaborane representing the smallest carborane cage, is an electron-"precise" molecule in which no bond is formed between the B atoms in the equatorial plane. The topology of the experimental ED of the ethyl-substituted molecule (pentaethyl-1,5-dicarba-*closo*-pentaborane)[142] (**15**, Scheme 15), veri-
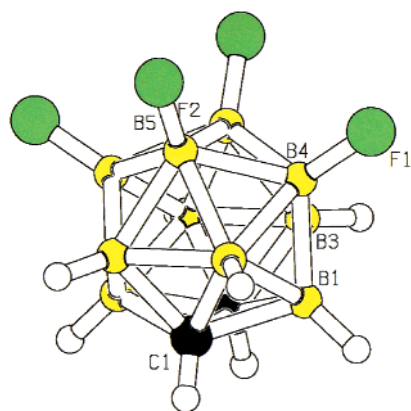
Scheme 15
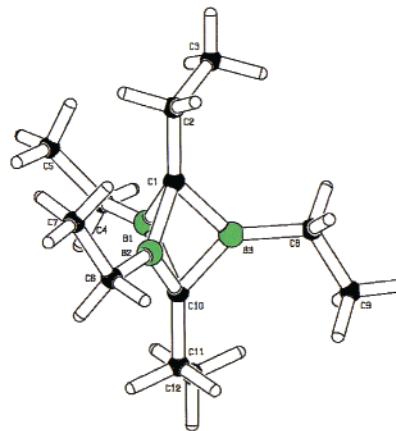
15

fies the prediction that the boron atoms are formally trigonal. Despite the short B−B distances ($R_{ave} = 1.876(4)$ Å), no BPs directly connecting the boron atoms are found, but the density midway between the B atoms amounts to a relatively high value ($\rho(B-B)_{ave} = 0.72$) that is, however, considerably lower than the density in the C−B bonds ($\rho(C-B)_{ave} = 1.03$). This is due to the charge concentration in the BCBC-rings, the RCPs of which are located close to the corresponding B−B internuclear lines.

Charge delocalization becomes an increasingly important stabilizing factor in more electron-deficient systems, such as large cage carboranes. According to the experiment-based topological structure of 8,9,-

Scheme 16

16

10,12-tetrafluoro-*o*-carborane[143] (**16**, Scheme 16), each of the C and B atoms forming the icosahedron is hexacoordinated (six BP terminate at each nucleus). The B−B and C−B bonds in the cage are similar in terms of the $\rho(\mathbf{r}_{BCP})$ and $\nabla^2\rho(\mathbf{r}_{BCP})$ parameters ($\rho(B-B)_{ave} = 0.81$, $\rho(C-B)_{ave} = 0.89$ and $\nabla^2\rho(B-B)_{ave} = -1.4$, $\nabla^2\rho(C-B)_{ave} = -3.4$), though the BCP locations are markedly different for the two types of bonds. Owing to the charge delocalization over the faces (CCB, CBB, and BBB rings), all BPs associated with the peripheral bonds are outwardly bent with extremely large bond ellipticities (0.82−5.38). Extended charge localization is reflected in the Laplacian of the density, which is negative over each of the ring surfaces beyond the atomic core regions.

## 5. Experimental Topological Analysis of Hydrogen Bonding

The characterization of H bonds (D−H···A) on the basis of the ED has attracted considerable attention over the past decade. Early topological analyses of theoretical EDs of H-bonded complexes between nitriles and hydrogen halides[144] have shown a linear correlation between the bond energy and $\rho(\mathbf{r}_{BCP})$ of the N···H bonds for internuclear separation greater than 2 Å. Koch and Popelier[145] proposed a set of "necessary and sufficient" criteria, based on the AIM theory, for recognizing an H···A interaction as an H bond. These are (i) the existence of a BP (BCP) between the H and the A atoms, (ii) a low value of $\rho(\mathbf{r}_{BCP})$ which correlates with the bond energy, (iii) positive $\nabla^2\rho(\mathbf{r}_{BCP})$, (iv) mutual penetration of the H and A atoms, measured by the difference between the nonbonded and bonded atomic radii of the participating atoms, (v) loss of charge at the H atom, (vi) decrease of dipolar polarization of the H atom, and (vii) decrease of the volume of the basin associated with the H atom.

Many of these characteristics of the H bond can be obtained from experimental deformation EDs, especially by comparison with the theoretical densities for the isolated molecules. Such comparisons are not free of ambiguities because the level of approximation and basis set effects are of importance. Despite promising results,[146] the question whether the experimental error (estimated to be 0.05 in a general

position) allows for detecting crystal-field effects that are approximately of the same magnitude remains relevant. As discussed in the preceding section, studies using simulated data indicate that real-space changes due to H bonding are well localized at the H and A atoms and that these changes affect the low-angle structure factors to only about 1%. Because of this low signal-to-noise ratio, detection of crystal-field effects requires precise data and adequate modeling. To establish a correct structural model, in particular with respect to the positional and thermal parameters of the H atoms, it is essential to include neutron diffraction information in the analysis (X + N method). However, corrections for the different nature of the experimental errors of the two techniques may have to be applied.[61] A number of studies performed at this level of sophistication are discussed below.

Owing to its extremely high proton affinity, 1,8-bis(dimethylamino)naphthalene[147] (**17**, Scheme 17;

Scheme 17
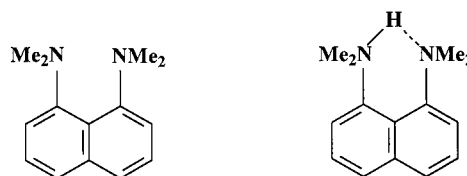
"proton sponge"), forms very stable ionic complexes with acids. The proton is captured in a N−H···N intramolecular H bond, the strength of which alone would not explain the unusually high basicity of the acceptor molecule. In the ionic complex of **17** with 1,2-dichloromaleic acid,[148] the H−N distances in the N−H···N hydrogen bond (1.106(5) and 1.608(6) Å) indicate that the proton in the cation is more strongly bonded to one of the N atoms. Furthermore, it does not lie on the N−N internuclear axis. On the other hand, the O···H···O hydrogen bond in the anion is almost symmetric and the proton is located practically on the O···O interatomic line.

The analyses of the experimental electron density and its Laplacian (Figure 9) obtained from X + N data give information on the nature of the H bonds and provide evidence for the charge redistribution upon protonation. The proton in the cation is covalently bonded to the nearest N atom ($\rho(\mathbf{r}_{BCP}) = 1.91(3)$), but the CP of the second H···N interaction in the cation is in a region of positive Laplacian ($\rho(\mathbf{r}_{BCP}) = 0.53(2)$, $\nabla^2\rho(\mathbf{r}_{BCP}) = 4.3(1)$). The VSCC of the acceptor N atom is considerably polarized toward the proton. The bond path trajectory along N−H···N is not linear, i.e., the N−H and H···N BPs are longer than the corresponding internuclear distances and the angle between the BPs (136.2°) is smaller than the geometrical bond angle (153.3°). In the O···H···O hydrogen bond the CPs lie within the VSCC of the H atom, i.e., $\nabla^2\rho(\mathbf{r}_{BCP})$ is negative for both interactions, but no continuous region of negative Laplacian along the linear BPs is observed, suggesting the interaction to be electrostatic in nature. However, in the theoretical Laplacian maps a continuous ridge in the negative Laplacian connects the hydrogen atom to the nearest O atom, a difference that requires further attention.
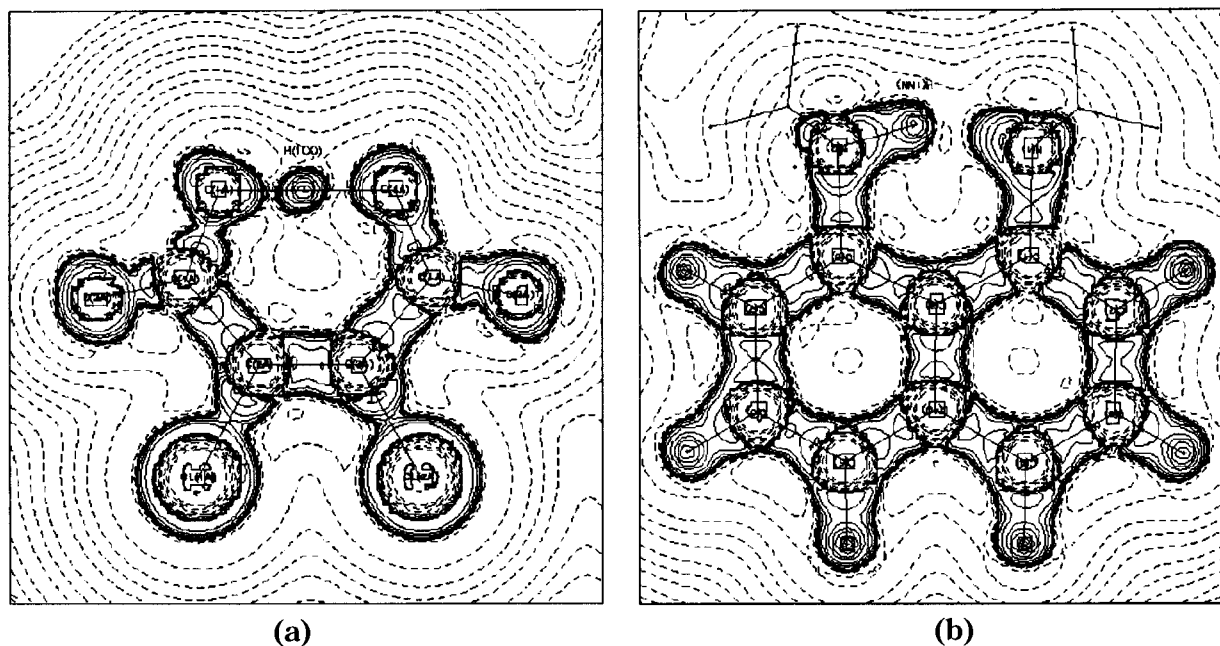
Figure 9. Experimental Laplacian maps in the molecular plane of (a) 1,2-dichloromaleic acid and (b) 1,8-bis-(dimethylamino)naphthalene (bottom). Contours are at logarithmic intervals in $-\nabla^2\rho(\mathbf{r})$ e/Å^5.[148]

Comparison of the geometrical parameters of the neutral and ionic species shows that upon protonation the aromatic C—C bonds become shorter while the C—N bond at the acceptor N atom lengthens. These structural changes manifest themselves in the $\rho(\mathbf{r}_{BCP})$ values, indicating that in the ionic form the conjugation, which in the base includes also the NH$_2$ groups, is limited to the naphthalene ring. The line representing the $\rho(\mathbf{r}_{BCP})$ vs r_{BCP} dependence for the C—C bonds in the ionic species has a higher slope and lies above the corresponding line for the base.

Very strong O···H-type H bonds, with O···O distances less that 2.5 Å, are found in the crystal structures of certain acid salts of dicarboxylic acids.[149] The O···H···O hydrogen bond is either symmetric (single-well potential) or the proton is situated near the midpoint of the O···O internuclear line (double-well potential). Quite frequently the proton, occupying a special position, is shared by two symmetry-related carboxyl groups.[150] In many of these cases, the space group assignment is related to the proton's position and thus the interpretation of the X-ray data relies on the neutron diffraction results. In the crystal structure of methylammonium hydrogen succinate monohydrate (**18**, Scheme 18), for example, the

Scheme 18
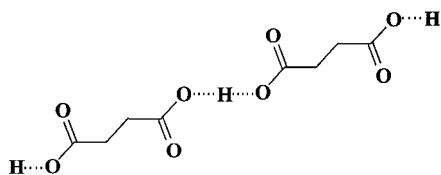
hydrogen succinate anion and the proton are located on inversion centers while the methylammonium cation and the water molecules are situated on a mirror plane of space group $P2_1/m$. There is a symmetric intermolecular O···H···O hydrogen bond, the proton being at an inversion center, with an

O···H distance of 1.2209 Å. The O atom of the other C=O bonds of the carboxyl groups are acceptors in two intermolecular H bonds of intermediate strength. The experimental topological study[151] shows that for the strong O···H interaction, the BCP is located 0.28 Å from the proton (Figure 10), with $\rho(\mathbf{r}_{BCP}) = 1.06(3)$
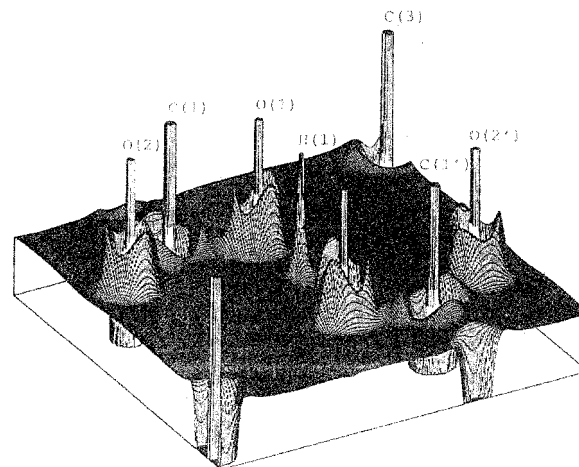

Figure 10. Negative of the Laplacian of methylammonium hydrogen succinate monohydrate. A least-squares plane defined by the labeled atoms is shown.[151]

and $\nabla^2\rho(\mathbf{r}_{BCP})$ negative ($-6.8(10)$). These values, when compared with those found for the weaker interactions ($\rho(\mathbf{r}_{BCP}) = 0.23$, $\nabla^2\rho(\mathbf{r}_{BCP}) = 2$ on average), indicate considerable covalent character for the symmetric O···H interaction. The covalent nature of the strong O···H bonding is also supported by the non-equivalence of the carbonyl bonds in the carboxylate group. The BCP parameters of the C—O(···H) bond indicate it to be weakened ($R = 1.286$ Å, $\rho(\mathbf{r}_{BCP}) = 2.52(2)$, $\nabla^2\rho(\mathbf{r}_{BCP}) = -29.7(1.2)$) relative to the second C—O bond of the carboxylate group ($R = 1.245$ Å, $\rho(\mathbf{r}_{BCP}) = 2.86(2)$, $\nabla^2\rho(\mathbf{r}_{BCP}) = -35.4(1.3)$).

An analogous bonding situation occurs in the crystal structure of methylammonium hydrogen maleate (**19**, Scheme 19). The asymmetric unit of the

Scheme 19
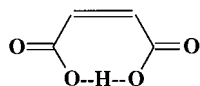
centrosymmetric structure (*Pnam*) contains a methylammonium ion in a general position and two hydrogen maleate ions on crystallographic mirror planes bisecting the C=C bonds.[152] The protons are located on the mirror planes between two symmetry related O atoms with O−O distances of 2.4214(5) and 2.4183(5) Å for the two anions, respectively. Both O···H interactions possess covalent character with basically the same BCP indices ($\rho(\mathbf{r}_{BCP})$ = 1.13(2) and 1.09(2), $\nabla^2\rho(\mathbf{r}_{BCP})$ = −5.9(9) and −7.1(9) for the two interactions), as found for the succinate ion. The values of $\rho(\mathbf{r}_{BCP})$ are only 40% of the theoretical value reported for the O−H covalent bond in water.

Additional examples of molecules possessing very strong O−H···O intramolecular H bonds are found among the β-diketone enols in which the proton is located midway between the *keto-* and *enol-*oxygen atoms in a low-barrier potential. Such an arrangement has been rationalized in terms of the resonance-assisted hydrogen-bonding (RAHB) model,[153] according to which the structure is stabilized through π-delocalization of the O=C−C=C−O−H *keto−enol* group (**20**, Scheme 20). The experimental verification

Scheme 20
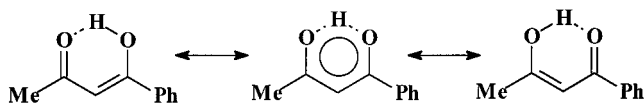
of this model is difficult because the X-ray diffraction image of a statistically disordered *keto−enol* system is most likely to be very similar to or practically indistinguishable from that of an ordered, delocalized system. However, the state-of-the-art diffraction study on benzoylacetone (**20**) provides justification for the latter picture, since the structure analysis based on 20 K neutron data excludes the possibility of the H atom being a static or dynamic disorder site.[154] The O···H···O bonding is almost symmetric with the H atom located, respectively, 1.329(11) and 1.245(11) Å away from the *keto-* and *enol-*oxygen atoms. In line with the ordered structure and the prediction of the RAHB model, the *keto−enol* group is planar and highly symmetric. The C−O and C−C bond lengths are intermediate between those typical for the corresponding double and single bonds.

Fine details of the bonding situation, such as π-delocalization, are revealed by the experimental BCP indices (based on 8.4 K X-ray data collected with Ag Kα radiation).[154] The $\rho(\mathbf{r}_{BCP})$'s and the ellipticities of the two, formally single C−C bonds in the *keto−enol* group are in the range of those obtained for the aromatic C−C bond in the benzene ring. The C−C bond adjacent to the *enol-*oxygen has slightly larger $\rho(\mathbf{r}_{BCP})$ (2.17) and ϵ (0.29) values than the C−C bond

adjacent to the keto oxygen (2.04 and 0.25). This suggests that one of the *enol* forms makes a larger contribution to the structure, in agreement with the slightly asymmetric position of the H atom in the O···H···O group. For the two O···H interactions, the $\rho(\mathbf{r}_{BCP})$'s are relatively high (0.76(3) and 0.89(3) e/Å³) and the $\nabla^2\rho(\mathbf{r}_{BCP})$'s are negative (−4.5(2) and −9.1(2) e/Å⁵). The VSCCs of the O atoms participating in the bond are well separated from those of the H atom, but they are enhanced and elongated along the BPs. These observations are in close agreement with those found in the other studies discussed above and are supported by a detailed theoretical analysis.[155]

Abramov[156] proposed a simple expression for the kinetic energy density along bond paths of both open-shell and closed-shell interactions. The expression for closed-shell interactions gives a reasonable approximation to HF values for distances 0.7 > *r* > 2.1 Å away from the nuclei. It is based on the Thomas−Fermi approach[157] and includes a gradient correction[158] which vanishes at the CP:

$$G(\mathbf{r}_{BCP}) = \left(\frac{3}{10}\right)(3\pi^2)^{2/3}\rho^{5/3}(\mathbf{r}_{BCP}) + \left(\frac{1}{6}\right)\nabla^2\rho(\mathbf{r}_{BCP}) \quad (22)$$

The potential energy density can be estimated by combining this equation with eq 18, assuming that the local virial theorem holds also in the case of experimental density. Espinosa et al. made use of the above expression in their analysis of the strength of H bonds as implied by the topology of experimental EDs.[6] The distances of BCPs from the nuclei participating in X···H···O (X = O, N, C) interactions are typically in the range where eq 22 is applicable. Structural and topological parameters of 83 H bonds (with O···H distances in the range 1.56−1.97, 1.65−2.63, and 2.28−2.59 Å, for X = O, N, and C, respectively) were used in the analysis, the results of which are shown in Figure 11. Both energy densities show an exponential dependence on the O···H distance. The decrease of $G(\mathbf{r}_{BCP})$ with increasing distance is expected on the basis of similar correlations found for $\rho(\mathbf{r}_{BCP})$ and $\nabla^2\rho(\mathbf{r}_{BCP})$. Using the analytical representations of both energy densities, it is possible to draw the boundary between weak and strong H bonds. Characteristic of the former and latter interaction is the positive and negative value of $\nabla^2\rho(\mathbf{r}_{BCP})$, respectively. At the $\nabla^2\rho(\mathbf{r}_{BCP})$ = 0 point, $V(\mathbf{r}_{BCP})$ = 2 $G(\mathbf{r}_{BCP})$ (from eq 18). This condition, when applied to the empirical functions for *V* and *G*, leads to an O···H separation of 1.33 Å (*G* = 320 kJ/mol/au³). This distance can be considered as a threshold below which an H bond possesses covalent character. A further important result of this study is the relation found between the energy of the H bond and $V(\mathbf{r}_{BCP})$. Theoretically calculated bond dissociation energies (*D*) as a function of the O···H distance can be fitted with an exponential curve, the exponent of which is found to be statistically equal to the exponent in the equation used to fit $V(\mathbf{r}_{BCP})$. The relationship $E(\mathbf{r}_{BCP}) = -D = -^1/_2 V(\mathbf{r}_{BCP})$ seems to be valid to a good approximation.

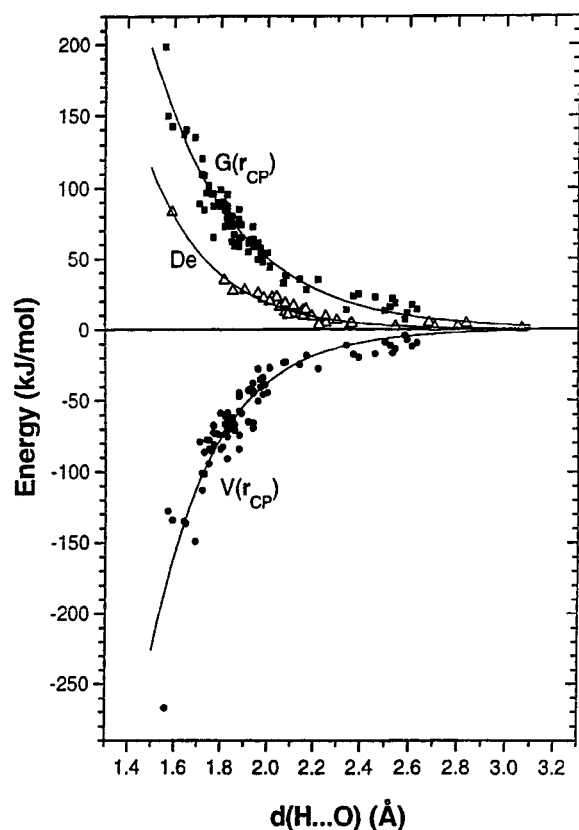As the energy density corresponds to a force per unit area, $V(\mathbf{r}_{BCP})$ can be interpreted as the pressure

Figure 11. Experimental kinetic energy density at the bond critical point $G(\mathbf{r}_{CP})$ (kJ/(mol·au³)), experimental potential energy density $V(\mathbf{r}_{CP})$, and theoretical dissociation energy (kJ/mol) as a function of the H···O distance. (Reprinted with permission from ref 6. Copyright 1998 Elsevier Science.)

exerted by the H-bond system (atomic basins) on the electrons around the BCP while $G(\mathbf{r}_{BCP})$ can be interpreted in the opposite sense.

These results are encouraging and seem to leave little doubt that the effects of secondary forces on the molecular ED have an observable effect on the Bragg intensities. Furthermore, it appears that these effects can be projected into the parameters of the aspherical-atom model, though in intermolecular regions the total ED is only slightly different from that of a superposition of promolecules. Because of this, Spackman[159] reinterpreted the H-bond data used in the study outlined above in terms of a very simple model in which the ED of the O···H system was taken as the superposition of spherical HF densities of the participating atoms. Not unexpectedly, this two-atom model, without additional parameters (i.e., without fitting the model-predicted properties to those observed), reproduces the observed behavior of $G(\mathbf{r}_{BCP})$ extremely well and that of $V(\mathbf{r}_{BCP})$ reasonably well, but it fails to reproduce the $\rho(\mathbf{r}_{BCP})$ vs $\nabla^2\rho(\mathbf{r}_{BCP})$ relation, especially at high values, i.e., at low internuclear separation. This is because the bond charge concentration due to covalent interaction is not accounted for by the promolecule density.

In a subsequent study, Espinosa et al.[160] found for the same H-bond data that the kinetic and potential energy densities at the BCP were linearly related to the positive and negative curvatures, respectively, of ρ at the BCP. In other words, as all curvatures of ρ

at the BCP increase in magnitude upon shortening of the H bond, both components of the local energy at the BCP similarly increase in magnitude. This provides an effective partitioning of the local energy into components associated with the dilution and concentration of the electrons at the BCP.

In very recent work, Espinosa and Molins[161] assume that the empirical local energy density at the BCP, H_{BCP}, can be expressed as a function of the A···H separation (R) by a sum of two exponentials (where A, B, and $D > 0$ and $C < 0$)

$$H_{BCP}(R) = G(\mathbf{r}_{BCP},R) + V(\mathbf{r}_{BCP},R) = \\ A\cdot\exp(-B\cdot R) + C\cdot\exp(-D\cdot R)$$

and that H_{BCP} is proportional to the interaction potential ($U(R) = -\nu H_{BCP}(R)$). The proportionality constant ν was estimated from the force constant of the O···H hydrogen bond in ice VIII and from the values of the local energy densities at the equilibrium O···H separation. The function obtained was successfully tested against Morse- and Buckingham-type potentials and several physical and chemical properties.

D. Minerals

The adequate modeling of the Si—O interaction in SiOM (M = Si, Al, B) groups is crucial to the understanding of the crystal chemistry of silicates and zeolites. An interesting feature of the Si—O bond in a silicate framework —Si—O—Si— is its shortening with increasing Si—O—Si angle.[162] On the basis of the conventional orbital picture, this correlation can be ascribed to the increase of the π-character of the bond due to $d(Si)-p(O)$-type orbital overlap that is favored by the linear arrangement of the three atoms.[163] The significance of the $d(Si)$ orbitals in the bond formation has been the subject of a series of MO studies on small molecules representative of the silicate- and zeolite-type structures.[164] Parallel to these efforts, experimental investigations have been extended to minerals with the aim of characterizing the Si—O bond in terms of deformation densities.[165] The first application of topological descriptors to theoretical densities of a variety of hydroxysilicic acid and siloxane molecules[166] revealed that the shortening of the Si—O bond is accompanied by a charge build-up at $\mathbf{r}_{BCP}$ together with a concentration of ρ both perpendicular and parallel to the BP. $\rho(\mathbf{r}_{BCP})$, $|\lambda_1|$, $|\lambda_2|$, λ_3, and $\nabla^2\rho(\mathbf{r}_{BCP})$ all increase as the Si—O bond length decreases, while the partial π-character of the bond decreases (ϵ approaches to zero) as the bond angle opens.

BCP analyses of experimental densities have been performed on coesite,[167] scolecite,[168] natrolite,[168b] mesolite,[168b] topaz,[169] and danburite.[170]

Coesite, a silica polymorph, is a framework of two nonequivalent, corner-sharing silicate tetrahedra. The existence of 8 symmetry-independent Si—O bonds, together with 12 nonequivalent OSiO and five SiOSi groups in the crystal makes coesite an especially suitable system to study the nature of the Si—O interaction. The experimental deformation density was reported by Geisinger et al.[171a] The same data were later reexamined by Downs,[167] who also evalu-

Table 4. Averaged Bond Topological Parameters of Si−O Bonds in SiOM Fragments (M = Si, Al, B) of Minerals[a]

compound	N	SiOM	R_{min}	R_{max}	R_{ave}	$\rho(\mathbf{r}_{BCP})_{ave}$	$\nabla^2\rho(\mathbf{r}_{BCP})_{ave}$
coesite							
experiment	8	SiOSi	1.5950	1.6186	1.611(3)	1.04(3)	20.3(5)
BLYP3						0.945(2)	23.6(3)
natrolite	2	SiOSi	1.6296	1.6373	1.634(5)	0.94(2)	13.7(1.1)
	4	SiOAl	1.6072	1.6201	1.613(3)	1.06(5)	14.3(2)
scolecite	4	SiOSi	1.6196	1.6418	1.633(6)	0.95(2)	16.2(5)
	8	SiOAl			1.611(11)	1.03(3)	17.7(6)
scoletice	4	SiOSi	1.6183	1.6442	1.634(7)	0.88(10)	12.9(4.0)
	8	SiOAl	1.5992	1.6341	1.613(5)	1.14(4)	12.6(2.1)
mesolite	6	SiOSi	1.6147	1.6464	1.635(5)	0.92(4)	11.2(1.5)
	12	SiOAl	1.5980	1.6354	1.614(3)	1.12(3)	10.9(1.1)
danburite	1	SiOSi	1.6150	1.6238	1.618(20	0.96(2)	18.1(6)
	3	+ SiOB					
topaz	4	SiOAl	1.6370	1.6420	1.642(2)	1.29(4)	9.7(1.0)

[a] The second line for coesite represents periodic DFT results (BLYP3). Numbers in parentheses are root-mean-square deviations based on the sample distribution.

ated the BCP properties. The Si−O bond lengths vary in the range of 1.595(1)−1.6208(9) Å. There is one linear SiOSi group, while the others exhibit nearly equal valence angles (143.45° averaged over four groups). An intriguing result of the coesite study is the observed difference between the experimental electrostatic potentials at the oxygen sites. One of the bridging O atoms is found to be distinctly more electronegative despite the structural equivalence between the SiOSi groups, suggesting a nonlocal influence on the potential. The latest study[171b] includes periodic calculation at the BLYP3 level and compares the results with those obtained experimentally. The calculated BCP indices show high correlation with the Si−O bond distance in accord with the outcome of the small molecule studies discussed above. The observed and calculated values for coesite agree on average within 10%, with the exception of the curvature along the bond path λ_3 and $\nabla^2\rho(\mathbf{r}_{BCP})$. Experimental values for the curvature are lower and those for the $\rho(\mathbf{r}_{BCP})$ slightly higher than the values predicted by density functional theory.

In zeolites, some of the Si atoms are replaced by Al atoms, thus forming Si−O−Al groups, the central O atom of which can accept a proton. The Brønsted acidity of such sites is related to the catalytic activity of zeolites. Common to the structures of zeolite-like aluminosilicates, natrolite ($Na_2[Al_2Si_3O_{10}]\cdot 2H_2O$), scolecite ($Ca[Al_2Si_3O_{10}]\cdot 3H_2O$), and mesolite ($Na_2Ca_2[Al_2Si_3O_{10}]\cdot 8H_2O$) is the ordered framework of corner-linked SiO_4 and AlO_4 tetrahedra. The cavities are occupied by water molecules and Na and/or Ca^{2+} cations coordinated to the oxygen sites. Of the 6, 12, and 18 nonequivalent Si−O bonds, in natrolite, scolecite, and mesolite, respectively, 2, 4, and 8 are adjacent (sharing common O atoms in SiOSi groups) while the remaining bonds are interconnected via Al atoms (SiOAl-type). The BCP properties are expected to depend on the coordination of the central oxygen atom, that is, the strength of the Si−O bond decreases due to the protons and the cations in the vicinity of the O atoms. Indeed, the comparative study of the experimental ED of these zeolites shows a relatively wide scatter when the Si−O BCP properties are plotted against the bond distance. A weak but significant correlation can be found between R(Si−O) and $\rho(\mathbf{r}_{BCP})$, $\lambda_{1,2}$, and the bonded atomic radii, while the Laplacian at the BCP seems to be

statistically independent of the interatomic separation. Table 4 lists R(Si−O), $\rho(\mathbf{r}_{BCP})$, and $\nabla^2\rho(\mathbf{r}_{BCP})$ values averaged over SiOSi- as well as SiOAl-type bonds. The former Si−O bonds appear to be consistently weaker than the latter ones in all three zeolites. The overall agreement of the BCP parameters with those calculated for coesite is reasonable. There are however large differences in the individual values of $\nabla^2\rho(\mathbf{r}_{BCP})$ for the Si−O bonds in scolecite and mesolite. For scolecite, the data reproduced from the study by Kuntzinger et al.[168a] appear to have higher internal consistency than those reported by Kirfel and Gibbs.[168b] The limited reproducibility in the experimental bond curvatures does not allow detailed chemical conclusions to be drawn at this time.

The properties of the Al−O bonds exhibit trends similar to those found for the Si−O bonds. The Al−O bond is considerably weaker than Si−O (R(Al−O)$_{ave}$ = 1.743(3) Å, $\rho(\mathbf{r}_{BCP})_{ave}$ = 0.68(5), and $\nabla^2\rho(\mathbf{r}_{BCP})_{ave}$ = 12.6(1.7), averaged over the 24 bonds in the three structures).

The borosilicate framework in danburite ($Ca[B_2-Si_2O_8]$) is formed by corner-sharing SiO_4 and BO_4 tetrahedra. The asymmetric unit is composed of five bridging O atoms, of which three are involved in SiOB, one in SiOSi, and one in BOB groups. This arrangement is realized by four independent Si−O (Table 4) and four B−O bonds (R_{ave} = 1.474(11) Å, $\rho(\mathbf{r}_{BCP})_{ave}$ = 1.05(6), and $\nabla^2\rho(\mathbf{r}_{BCP})_{ave}$ = 8.1(1.5)).

In the neosilicate topaz ($Al_2[SiO_4]F_2$), edge-sharing Al octahedra and corner-sharing Si tetrahedra form the silicate network resulting in each bridging O atom to be coordinated by one Si and two Al atoms. There are four unique Si−O (Table 4) and four Al−O bonds (R_{ave} = 1.895(3) Å, $\rho(\mathbf{r}_{BCP})_{ave}$ = 0.64(3), and $\nabla^2\rho(\mathbf{r}_{BCP})_{ave}$ = 4.8(4)).

V. Toward Electron Density Analysis of Very Large Molecules

As the number of macromolecular structures refined at a resolution higher than 1 Å is continuously increasing, a scattering model beyond the spherical-atom formalism becomes desirable, not only to probe the electron distribution, but equally to improve the estimate of the structure factor phases. We will first consider transferability of the electron density from smaller fragments and then discuss the trend toward

charge-density analysis of high-quality macromolecular data sets.

To what extent can macromolecular electron densities be built up from smaller fragments? The AIM theory provides a quantum mechanical definition of molecular residues recognized as functional groups in chemistry. The partitioning scheme assigns density units to group of atoms in a molecule, which can be used to build chemically analogous molecules. The key question concerning the theoretical construction of polymers is the transferability of the monomers. Are interaction surfaces defining a fragment in one system preserved in another system, i.e., in a slightly different chemical environment? Chang and Bader[172] demonstrated, based on theoretical EDs, how this approach is applicable to the construction of polypeptides from peptide units and discussed the transferability of these functional groups (see also Popelier et al.[173]).

A different approach to transferability is based on the formal atomic partitioning of the multipole formalism. As outlined in section II.A.3, the multipole model is a one-center formalism, that is, the total ED, molecular or crystalline, is composed of atomic contributions. Simple reasoning suggests that two chemically equivalent atoms have the same contribution to the total ED, provided their chemical environments are similar. Such chemical symmetry can either be imposed into the model in terms of constraints, keeping the multipole populations the same for the two atoms, or by constructing a molecular electron density from known pseudoatomic densities. The latter strategy has been explored using the peptide results discussed in section IV.[174] The comparison reveals that the deformation EDs, obtained from different compounds but with the same refinement strategy, are in agreement within 0.1 e/Å^3 and that the multipole populations of chemically equivalent atoms are statistically equal. This makes it possible to build a "deformation density databank" with averaged multipole populations for each chemically unique but transferable pseudoatom. The authors find, for example, that in a properly chosen local frame the deformation ED of an sp^3 C atom can be described by only three octupolar terms in the multipole expansion. The ED of each peptide, as calculated with the averaged parameters, resembles closely the corresponding ED obtained directly from the X-ray data. This is true not only in terms of the deformation ED but also in terms of BCP properties as demonstrated in Table 3. However, the density based on a limited number of averaged multipole populations from the database appears to slightly overestimate the density averaged over those extracted from the X-ray data of each of the peptides.

Application of transferable pseudoatomic scattering factors, constructed from the database, to the thyrotropin-releasing hormone analogue tripeptide pGlu-Phe-D-Pro-ϕ[CN$_4$]-Me gives a significant improvement over the spherical-atom model in R-factor and enhanced compliance with Hirshfeld's rigid bond test,[175] indicating an improvement in the physical significance of the thermal displacement parameters (ADPs). Subsequent application to a limited resolution (0.82 Å) X-ray data set on the 3$_{10}$ helix octapep-

tide Ac-Aib$_2$-L-Lys(Bz)-Aib$_2$-L-Lys(Bz)-Aib$_2$-NHMe likewise gave a considerable improvement in the crystallographic R-factor, accumulation of electron density in the lone-pair and bond regions in the deformation maps, and a significant change in the temperature factors.[176] These experiments suggest that protein structure refinements can be improved by application of preassigned aspherical scattering factors, provided the data resolution exceeds 0.9 Å and the structure is well resolved (atomic B factors lower than 4 Å^2).

Application of the database to room-temperature data of 0.96 Å resolution on the scorpion *Androctonus australis* Hector toxin II similarly revealed bonding effects but led to an underestimation of the net charges on the peptide-bond atoms.[177] Aspherical-atom refinement of high-resolution (0.54 Å) low-temperature data on the protein crambin led to parameters within 25% of those from the transferable database and somewhat lower bonding features than predicted by the database.[178] This may indicate that further adjustments are needed, though this observation must be checked on additional data sets. The dramatic improvements in data collection techniques are being exploited in a current study on the 316 amino acid enzyme aldose reductase.[179] The data, collected at the Advanced Photon Source (APS), have resolution of 0.66 Å and an excellent internal R-factor of 2.9%. Examination of the first deformation density maps suggests that an accurate description of the electronic structure of the active site of the enzyme is within reach.

VI. Charge Density of Transition-Metal Complexes

A. Background

Transition-metal compounds are an intriguing subject for charge-density studies. Their often complicated bonding can be varied by chemical substitution, as can the metal oxidation state, so that trends can be examined. Chemical reactions of transition-metal complexes are of enormous importance both in chemical and physiological processes and how the nature of transition-metal bonding affects the properties of many technologically important solids. Thus, a better understanding of the electronic structure of transition-metal complexes is crucial in many respects.

To what extent can experimental charge densities contribute to such understanding? The first experimental charge-density analyses were performed in the early development stage of the field. Pioneering studies by Iwata and Saito reported in 1973 on Cr-(NH$_3$)$_6$Cr(CN)$_6$[180] and in 1977 by Iwata on Co(NH$_3$)$_6$-Co(CN)$_6$[181] clearly validated the predictions of ligand-field theory, showing a pronounced depopulation of the field-destabilized e$_g$ orbitals and an increased population of the stabilized t$_{2g}$ type orbitals. The Dewar−Chatt−Duncanson (DCD) σ-donation/π-back-donation model for metal−ligand bonding[182] was substantiated by the study of Cr(CO)$_6$ by Rees and Mitschler,[183] who followed up with a number of careful investigations of the nature of metal−metal bonding, some of which are discussed further below.

With continuous advances in experimental techniques and computational facilities, studies of series of related compounds became feasible. Comparison of the charge densities in a number of high-, intermediate-, and low-spin Fe porphyrins in the 1970s and 1980s showed the variation in metal d orbital occupancy with electronic structure to be readily detectable by charge-density methods.[184,185]

In more recent work on transition-metal complexes, parallel theoretical HF and/or DFT calculations are routinely performed. Since the theoretical methods involve approximations such as neglect of correlation (as in the HF method), selection of functionals (in DFT), and the frozen core approximation (both HF and DFT), the intercomparison provides a calibration in both directions. Furthermore, much additional insight is gained by analysis of the topological properties of the electron density and its Laplacian as defined in the AIM theory.[76]

In the section on transition-metal complexes, we will review recent studies concentrating on the metal atom and its binding to the surrounding ligands and on metal−metal bonding. Unless otherwise mentioned, the studies are performed at, or close to, liquid nitrogen temperature.

B. Can Orbitals Be Observed?

The cover of a recent issue of *Nature* proclaimed *Orbitals observed*,[186] an accomplishment that was rapidly highlighted in the semiscientific and popular press. The claim was based on an elegant experiment on cuprite, Cu_2O, by Zuo et al.[187] in which previously published X-ray data[188] were complemented with a set of low-order reflection collected with the convergent beam electron diffraction (CBED) technique. Strong low-order reflections of relatively simple solids are especially sensitive to the extinction effect, which reduces their intensity through rescattering of the diffracted X-ray beams in the crystal. The CBED method eliminates this bias by recording the diffraction from a very small perfect area of the sample to which perfect-crystal dynamical diffraction theory can be applied for derivation of the structure factor amplitudes. The rescattering of the beams is implicitly accounted for in dynamical theory. Multipole analysis of the data leads to a resolution unprecedented for this type of solid and, apart from giving information on Cu−Cu bonding and charge transfer between Cu and O, shows deformation features around the Cu atom reminiscent of the d orbitals depicted in chemistry text books. However, one must firmly keep in mind that the observable on which the diffraction experiment gives information is the *electron density distribution* rather than the *electron orbitals*, which are mathematical concepts not defined in a unique manner. Because of this, orbitals cannot possibly be observed, as pointed out eloquently in a recent publication by Scerri.[189] As emphasized by Wang and Schwarz in a critical analysis of a number of the conclusions drawn by Zuo et al.[190] and the subsequent publicity, features in the not always positive deformation density can sometimes be approximated by an everywhere positive, orbital *density*, but the positive and negative features
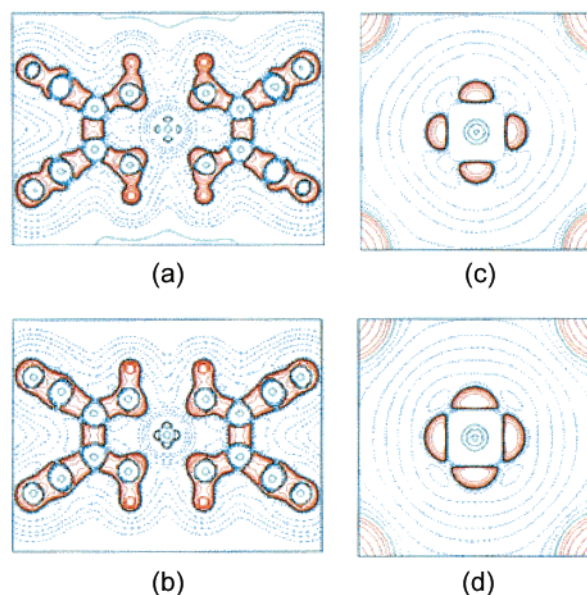

Figure 12. Negative Laplacian in the molecular plane of bis(diminosuccinonitrilo)nickel (**21**) (a, b) and the enlarged plot around Ni (c, d), where parts a and c are from experiment and b and d are from calculation. Contours are $2^i \times 10^j$ eÅ^{-5} ($i = 1, 2, 3$), where $j = -1, 0, 1$ for a, b and $j = 0, 1, 2$ for c, d. Solid red lines, positive; broken blue lines, negative; green line: zero contour.[192]

around Cu should never be confused with an orbital, which is an, in general complex, amplitude function.

It should be noted that the conclusion of Zuo et al.[187] that a Cu−Cu bond exist in Cu_2O is at variance with the results of a careful multiwavelength high-energy synchrotron analysis of Lippmann and Schneider,[191] who find no evidence for charge accumulation in the relevant tetrahedral sites.

C. Transition-Metal Atoms and Metal–Ligand Binding

In accordance with the DCD model, the MO formed by combination of a filled ligand σ-orbital with an empty 3d orbital on a metal atom represents σ-donation from the ligand to the metal atom. In the topological analysis the effect demonstrates itself by the lining up of the nonbonded VSCCs on the ligating atom ((3,−3)CP of $-\nabla^2\rho$) with the charge depletions on the M atom ((3,+1)CP of $-\nabla^2\rho$). This key-lock arrangement is evident in many charge-density studies. Both the experimental and the theoretical maps of the negative Laplacian around the Ni atom in square planar bis(diminosuccinonitrilo)nickel (**21**, Scheme 21),[192] shown in Figure 12, illustrate this

Scheme 21
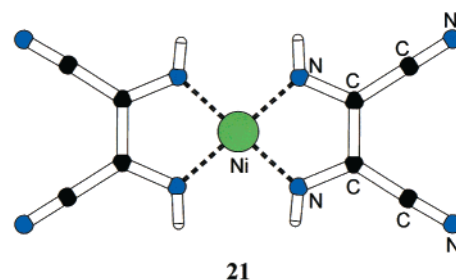
21

effect. The nonbonded VSCCs of the metal atom are located on lines bisecting the N–Ni–N angles, while the maxima of $-\nabla^2\rho$ on the N atoms point toward the voids on the metal atom. The BCP of the Ni–N bond (1.828 Å) in the bis(diminosuccinonitrilo)nickel complex is located midway between the atoms. At the BCP the density has a low value (0.94) and the Laplacian is positive (12.3), an observation which is typical for many if not all transition-metal complexes.

For **21**, the Fermi hole density with the reference electron placed on any ring C or N atom shows the ligand to be totally π-electron delocalized. It indicates a degree of electron pair localization and thus covalency in the Ni–N bond, notwithstanding the closed-shell interpretation of the Laplacian. A second example of a positive Laplacian in the metal–ligand bond is provided by the study of Smith et al. on [Ni-(H$_3$L)][NO$_3$][PF$_6$] [H$_3$L = N,N',N'-tris(2-hydroxy-3-methylbutyl)-1,4,7-triazacyclononane] (**22**, Scheme 22). Values of $\nabla^2\rho$ are positive at the BCPs of the

Scheme 22
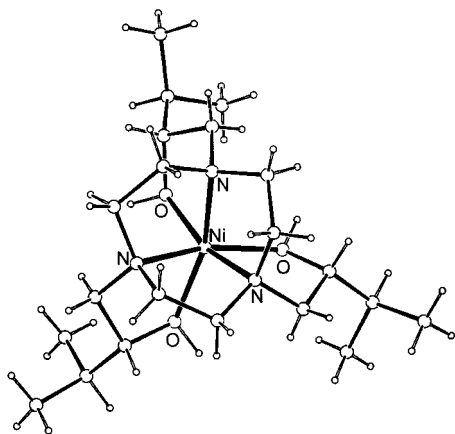
Ni–N (1.4(3)) and especially the Ni–O (9.77(7)) bonds.[193] The authors note that the closed-shell interpretation is at odds with both accepted chemical notions and other evidence from charge-density studies and conclude that "*it would appear that the topological properties of covalent metal–ligand bonding do not have the same characteristics as covalent bonding between first-row atoms*". The electron density is very high at the positions of the heavier metal nuclei. The resulting sharp decrease along the bond paths causes the curvature λ_3 at the BCP to be large and positive, corresponding topologically to an electron depletion along this direction, even though the metal–ligand bonds are partially covalent.

Despite there being a total of six ligating atoms in the Ni complex (**22**), the results suggest that only four bond paths terminate at the metal. Three of these are conventional bond paths connecting the metal nucleus with the nitrogen atoms, while the fourth bond path emanating from the Ni atom appears to be trifurcated into three branches, each leading to an oxygen atom and each corresponding to a separate BCP. This unusual arrangement, not observed in other studies, could imply that the three bond paths are so closely spaced that they cannot be separated by the resolution of the experiment or by the numerical procedure used. [We are grateful to a referee for comments on this result.]

The key-lock mechanism of metal ligand bonding is also evident in lithium bis(tetramethylammonium) hexanitrocobaltate(III) (**2**).[99] As in other compounds, the maxima of the VSCCs of the Co atom avoid the nonbonded VSCC of the N atom and the BCP of the Co–N bond (1.9655(2) Å) lies in a positive region of the Laplacian ($\rho(\mathbf{r}_{BCP}) = 0.50(1)$, $\nabla^2\rho(\mathbf{r}_{BCP}) = 12.1(1)$), in good accord with the theoretical result ($\rho(\mathbf{r}_{BCP}) = 0.62$, $\nabla^2\rho(\mathbf{r}_{BCP}) = 13.0$). The agreement between experimental and theoretical topological parameters in the first-row atom bonds is less satisfactory, however. The experimental values for λ_3 at the BCPs of the C–N and N–O bonds are approximately twice as large as the theoretical values obtained with a periodic Hartree–Fock (PHF) calculation with a modified 3-21G basis set. Inadequacy of the basis set used may be partially responsible, but a more important contribution to the discrepancy is likely the limited flexibility of the multipole model used, as discussed earlier in this review.

Much insight can be gained by analysis of a series of related complexes by, for example, varying the central 3d transition-metal atom. Figgis and co-workers studied ammonium metal Tutton salts (NH$_4$)$_2$-[M^{II}(H$_2$O)$_6$](SO$_4$)$_2$ with M = V, Cr, Mn, Fe, Cu, and Ni using both X-ray and polarized neutron diffraction.[194,195] The latter technique is used to derive the spin density of the electrons, an additional observable which combined with the charge density leads to further insight into the nature of bonding. Some of the more recent studies in this series, conducted at very low temperatures ($\sim$10 K), eliminate uncertainties due thermal diffuse scattering and to anharmonicity of the thermal vibrations, which is especially important in the Jahn–Teller-distorted complexes. The authors conclude that as more detail in the charge distribution becomes accessible at such low temperatures, limitations of the aspherical-atom refinement formalisms currently in use become evident.[196,197]

Lee et al. analyzed a series of metal squarate complexes [M^{II}(C$_4$O$_4$)(H$_2$O)$_4$] with M = Fe, Co, Ni, and Zn in which squarate dianions bridge the metal atoms into an infinite polymeric chain and combined the study with theoretical large basis set HF and DFT calculations on the isolated complex [Ni(HC$_4$O$_4$)$_2$-(H$_2$O)$_4$].[198] In these complexes the octahedral coordination of the metal atom consists of two squarate oxygen atoms and four water molecules (Figure 13).
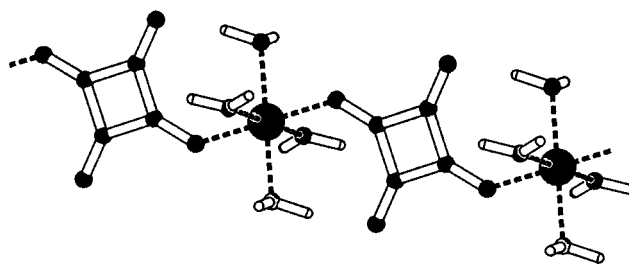

Figure 13. Infinite chain in crystals of the tetraaqua metal squarates.[198]

As in other strained ring systems (see section III.A), the deformation densities in the squarate plane show exocyclic bond peaks, indicating bent bonds, though

the experimental bending (~20° at the C atoms) is larger than that observed in the theoretical deformation density maps. The region of the Laplacian around the metal atoms in all cases shows the characteristic key-and-lock feature of metal−ligand binding. As in other complexes, Laplacian BCP parameters indicate the metal−ligand interactions to be of closed-shell nature, but an analysis of the Fermi hole function for $[Ni(HC_4O_4)_2(H_2O)_4]$, with a reference electron located at the lone pair density of either the water or squarate oxygen atoms, clearly indicates the shared character of the M−O bonds (Figure 14), in support of the discussion earlier in this section.
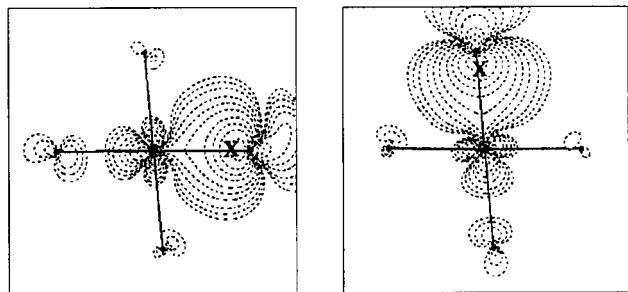

Figure 14. Fermi hole function in the molecular plane of $[Ni(HC_4O_4)_2(H_2O)_4]$ according to a DFT calculation. Reference electron located at (a) the squarate oxygen atom and (b) the oxygen atom of the water molecule (indicated by crosses).[198]

Further quantitative information on the electronic structure of metal atoms is obtained by d orbital analysis of the experimental results. The d electron populations (Table 5) show the expected increase

Table 5. d-Orbital Populations of $M(C_4O_4)(H_2O)_4$ (M = Fe, Co, Ni, Zn), from Ref 198

	Fe	Co	Ni	Ni[a]	Ni[b]	Zn
d_{z^2}	1.09(3)	0.98(4)	0.95(7)	1.09	1.22	1.36(7)
$d_{x^2-y^2}$	1.20(4)	1.11(5)	1.33(8)	1.06	1.15	1.64(8)
d_{xz}	1.43(5)	2.06(6)	2.02(9)	2.01	2.01	1.78(9)
d_{yz}	1.23(4)	1.22(6)	1.71(9)	1.98	2.02	1.55(9)
d_{xy}	1.10(4)	1.51(5)	1.84(8)	2.00	2.01	2.07(8)
total	6.05	6.88	7.89	8.14	8.41	8.40
net charge	+1.95	+2.12	+2.11			

[a] From HF calculation. [b] From DFT calculation.

from Fe (d^6) to Zn (d^{10}). For Fe, Co, and Ni, the populations of the e_g orbitals are consistently less than those of the ligand-field-stabilized t_{2g} orbitals. Among the t_{2g} orbitals, the population of d_{xz} (with z along the M−$O_{squarate}$ bond and x approximately perpendicular to the squarate plane) is higher than that for the other two orbitals for Fe, Co, and Ni, which is plausible evidence for the π-character of this M−O bond. This feature and, more general, the distribution of the electrons over the d orbitals of the Fe complex are very similar to those in corresponding Tutton salt, according to both experiment[195] and theory.[199]

The coordinated water molecules in the metal−squarate complexes are generally observed as positive by 0.1−0.3 electrons. Similar observations have been made for crystalline hydrates such as oxalic acid dihydrate,[34a] D,L-proline monohydrate,[200] L-aspar-

agine monohydrate,[107,232] and others, as well as in earlier studies of transition-metal complexes.[201,202] As theoretical results predict the charge transfer to be almost negligible, this observation merits further attention.

Transition-metal carbene complexes are generally divided into Fischer- and Scrock-type complexes. In the former, the carbene atom is electrophilic and the metal atom is generally in its low oxidation state, while in the latter the complex is nucleophilic at the carbene atom and the metal atom tends to be in its high oxidation state. Four pentacarbonyl Fischer-type chromium−carbene complexes $(CO)_5CrC(XR')R$ (X = O, N) (**23**, Scheme 23) were subjected to a charge-

Scheme 23
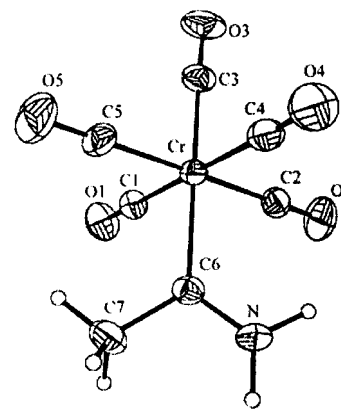
density study by Wang et al.[203] In two cases parallel theoretical calculations were performed. The combined study shows that the π-bond character in these metal carbenes can be best represented by a Cr−C−X three-center four-electron bond with the π-density largely located at both Cr and the X atom in the carbene ligand. The shortening of the M−$C_{trans\ carbonyl}$ bond for X = N, relative to X = O, is shown to be due to the close proximity of the π^*-(C−N) and π^*-(C−O) orbital energies. The $Cr(CO)_5$ fragment is the electron acceptor in the complex (−0.38 e) and the carbene fragment the donor, in accordance with the results of the theoretical calculations and the chemical behavior.

The analysis of bis(1,5-cyclooctadiene nickel) (**24**, Scheme 24) by Macchi et al.[204] constitutes the first

Scheme 24
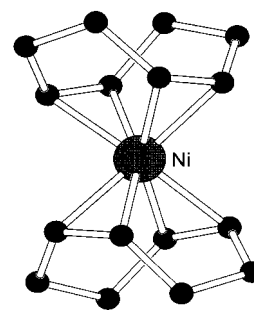
experimental study of a metal−olefinic π-ligand bond. The Ni atom and the two olefinic carbon atoms form a three-membered ring, but the topology of ρ (and the deformation density) shows features quite different from those of the strained three-membered

rings, in which, as discussed above, the bond paths are curved outward from the ring. The classification of the metal−ligand bonding is based on the comprehensive treatment of bonding in transition-metal compounds by Frenking and Fröhlich,[205] who extended the molecular-graph analysis of bonding between a molecule A_2 and an atom or atomic group X of Cremer and Kraka to M−η^2-transition-metal complexes,[206] the molecular graph being based on bond paths rather than on simple atomic connectivity. Four different types of molecular graphs are distinguished: (a) a bond path going straight from the center of the C=C bond to the metal, (b) σ-donation plus back-donation into σ^* orbitals with a strongly inwardly curved bond path, (c) DCD type σ-donation of a π-bond on the ligand, plus back-donation into a π^* orbital with bond paths that are less curved inward and almost straight except near the C atoms, and finally (d) a true metallacycle with a larger charge concentration along the M−C bonds than for c, representing covalent metal−ligand interaction. In the case of bis(1,5-cyclooctadiene nickel), the topology supports the DCD model, the Ni−C bond paths being inwardly curved but well separated (Figure 15). In accordance with this interpretation, the d orbital analysis shows a depopulation of the two d orbitals responsible for the back-donation effects and a population increase beyond the spherical distribution for the d orbitals involved in ligand donation.
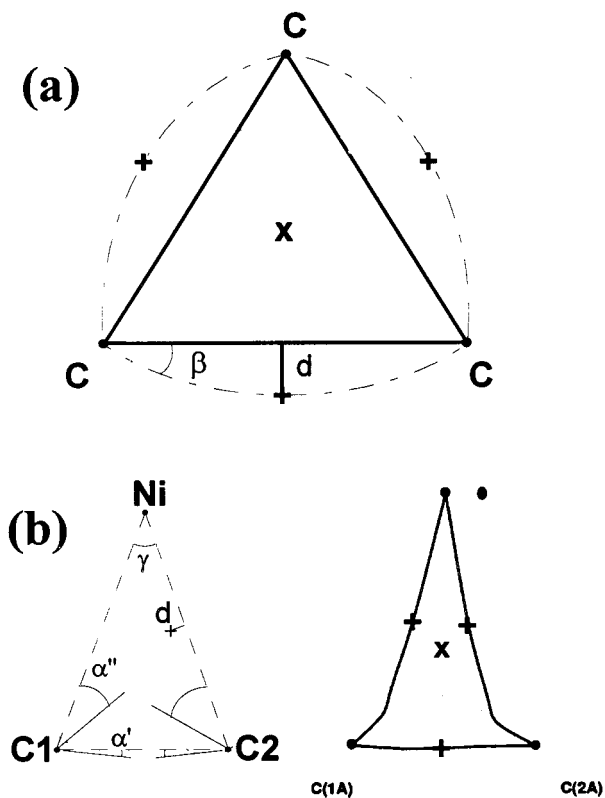

Figure 15. (a) Schematic bond path drawing of cyclopropane, drawn from theoretical results: $\beta = 9.42°$, $d = 0.06$ Å. (b) Bond path in the Ni (C=C) ring of bis(1,5-cyclooctadiene nickel) from experiment. $\alpha'C(1) = 5.42(7)°$, $\alpha'C(2) = 2.91(5)°$. The bond path angle at Ni, $\gamma = 24 (2)°$, compared with the geometrical angle of 38(1)°. The distances between the Ni−C BCPs and the geometric bond (d in the figure) are 0.101(8) and 0.144(10) Å The BCPs are located *inside* the ring.[204]

The nature of the M−H···H interaction has been the subject of a study by Abramov, Brammer et al.[207] In *cis*-HMn(CO)$_4$PPh$_3$, the hydride ligand makes a short contact of 2.101(3) Å with an electrophilic ortho phenyl hydrogen atom of the same molecule (Figure 16). The charge-density study shows the hydride H
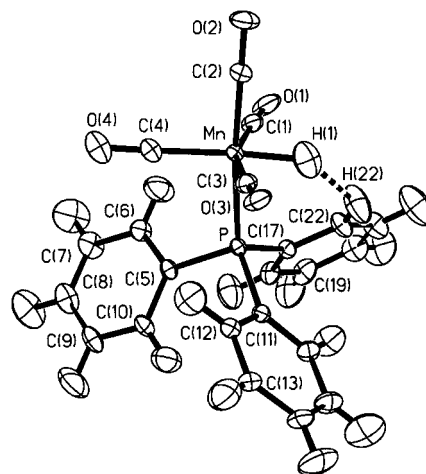

Figure 16. Molecular structure of HMn(CO)$_4$PPh$_3$. Dashed line indicates the C−H···H−Mn bond.[207]

atom to be negative (−0.4 e) and the phenyl H atom to be positively charged (+0.3 e). The H···H interaction is represented by a topological bond path with ρ_{BCP} quoted as 0.066(5) and $\nabla^2\rho$ positive but small, similar to those of typical hydrogen bonds. As for bis-(1,5-cyclooctadiene nickel), the occupancy of the d orbitals involved in back-donation to the carbonyl ligands is significantly less than that of orbitals less or not involved in this interaction. Typically,[208] the carbon atoms of the C=O ligands are more negative than the oxygen atoms.

The agostic interaction between a metal atom and a coordinated hydrogen, of relevance to C−H activation in metal-catalyzed polymerization reactions, has been the subject of a combined experimental and theoretical study of [EtTiCl$_3$(dmpe)][dmpe = 1,2-bis-(dimethylphosphino)ethane] (**25**, Scheme 25).[209] The
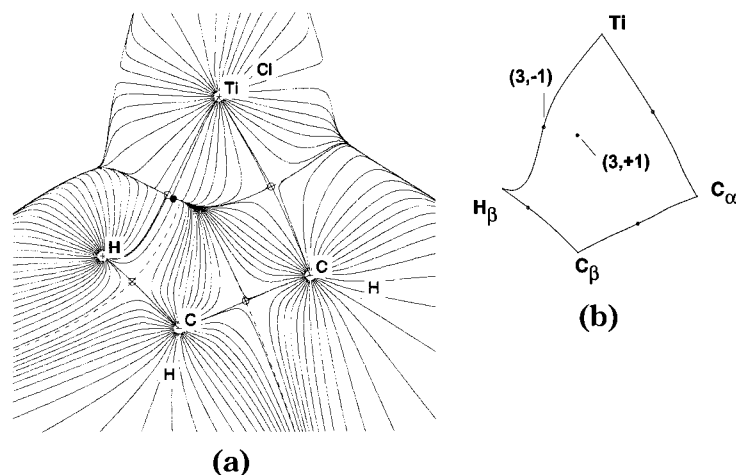
Scheme 25

25

(a)

(b)
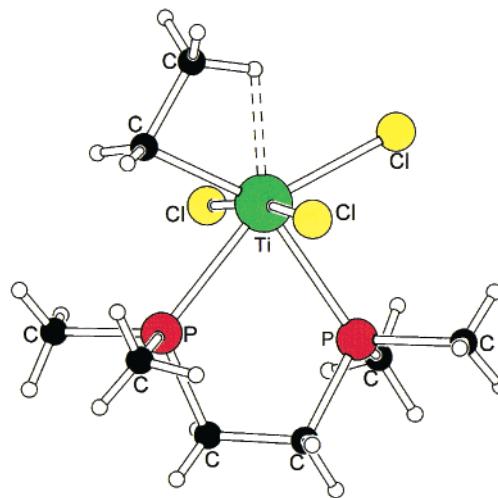
Figure 17. (a) Calculated gradient vector field in the Ti$-$C$-$C$-$H plane of [EtTiCl$_3$(dmpe)] (dmpe = 1,2-bis-(dimethylphosphino)ethane) (**25**). Bond CPs are denoted by open circles, and the ring CP is denoted by a filled circle. Bond paths are indicated by thick lines.[209b] (b) Bond paths in the Ti$-$C$-$C$-$H ring based on the experimental charge density.[209a] (Reprinted with permission from 209a. Copyright 1998 The Royal Society of Chemistry.)

distance from the Ti atom to one of the H atoms of the C$_2$H$_5$ ligand is, at 2.06(2) Å, only about 20% longer than the Ti$-$H single-bond length from theoretical DFT calculations on the related EtTiH$_3$ system, while the distance to the C$_\beta$ atom of the Et ligand is only 17% longer than that to the metal-bonded C$_\alpha$ atom. The theoretical (DFT) $\rho(\mathbf{r}_{BCP})$ values in the Ti$\cdots$C$_\alpha$ and Ti$\cdots$H$_\beta$ bond paths are 0.63 and 0.21, respectively, and the Laplacians are somewhat positive at 1.5 and 3.3, not unlike what is found for other metal$-$ligand interactions. However, the authors note that the (3,$-$1) Ti$\cdots$H$_\beta$ bond- and (3,+1) Ti$-$C$_\alpha$$-C_\beta$$-H_\beta$ ring-critical points are proximal (Figure 17) with densities which are essentially identical. This means that the two critical points almost merge into a singularity. They point out that a more meaningful manifestation of the agostic interaction may be found in the outward displacement by 0.06 Å of the Ti$\cdots$C$_\alpha$ bond path (Figure 17), a feature also observed in theoretical studies of agostic model compounds.[210]

D. Metal–Metal Bonding

Metal$-$metal bonding in transition-metal complexes tends to be more directed and stronger than the bonding in metals and alloys. Nevertheless, in many cases conventional deformation density maps, in which spherical atoms are subtracted from the total density, failed to show density accumulation between the metal atoms. Examples are dimanganese decacarbonyl Mn$_2$(CO)$_{10}$,[208] in which the metal$-$metal bond is unsupported by bridging ligands, (μ-methylene)bis[dicarbonyl(η^5-cyclopentadienyl)manganese][211] and bis[dicarbonyl-π-cyclopentadienyl iron] (**26**, Scheme 26).[212] Density accumulation in the Mn$-$Mn bond becomes visible, however, when a bonded fragment such as Mn(CO)$_5$ is used as the reference in the theoretical analyses of the Mn$_2$(CO)$_{10}$ charge density.[213,214]

For quadruply bonded and axially substituted dichromium tetraacetate, a broad area of excess electron density off the bond axis was found even in the conventional deformation density map, compatible with overlap between diffuse d orbitals.[215] The

Scheme 26
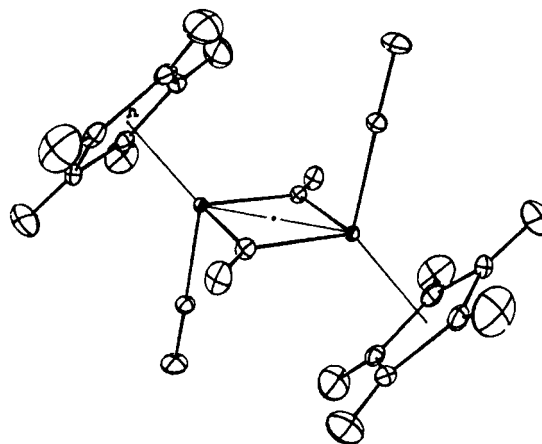
deformation density does show a pronounced inter-metallic maximum, however, for the much shorter Cr$-$Cr bond (1.879 vs 2.362 Å) in tetrakis(μ-oxy-6-methylpyridine)dichromium (**27**, Scheme 27). In this complex, the bond is bridged by N$-$C$-$O moieties rather than by the O$-$C$-$O groups of the acetate ligands and axial ligation is prevented by the bulkier substituents. A large accumulation of density, with a peak height of 0.4 comparable to bonds between first-row atoms, is observed at bond midpoint.[216]

In recent years much additional insight into metal$-$metal bonding has been obtained through multipole analysis of the X-ray data followed by topological analysis of the static total electron density. Of particular interest are the simple binuclear carbonyls and higher homologues. The bonding in the (diamagnetic) series Mn$_2$(CO)$_{10}$, Fe$_2$(CO)$_9$, and Co$_2$(CO)$_8$, with 0, 3, and 2 M$-$M-bridging CO groups, respectively, has traditionally been inferred from electron-counting rules, which require a direct M$-$M bond to achieve an 18-electron configuration for each of the metal atoms. These are obviously simplifications that call for more detailed analysis.

Mn$_2$(CO)$_{10}$ was reexamined by Bianchi et al., following the early 1982 study,[208] using the new tools since developed.[217] The topological analysis gives no

Scheme 27

27
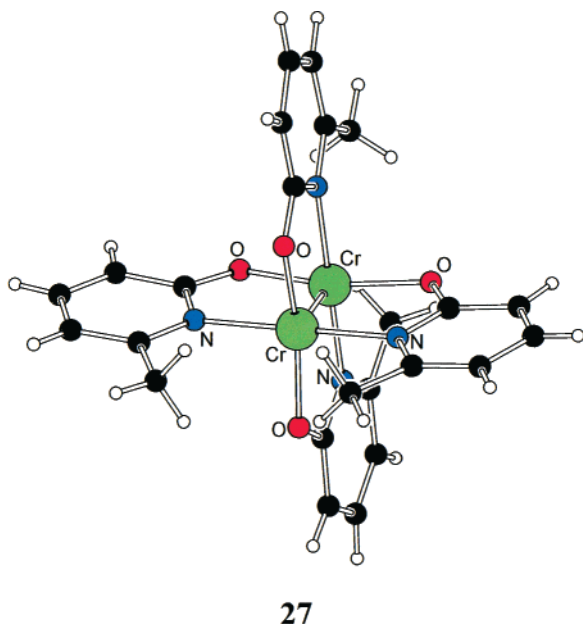
support for the existence of a 1···3 bond between the Mn and the carbon atoms of the equatorial carbonyl groups emphasized in some theoretical work,[218] as no bond paths between the metal and the equatorial carbonyls on the other Mn(CO)$_5$ group are observed. However, a bond critical point (Figure 18) with $\rho =$
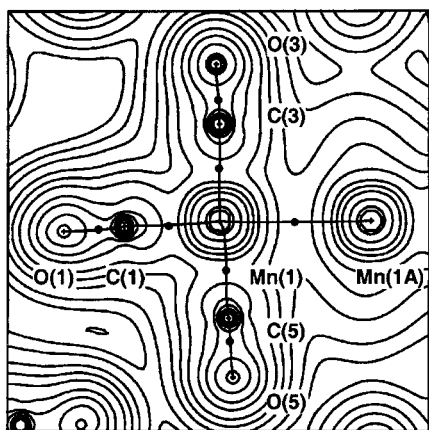

Figure 18. Experimental electron density in the plane defined by two Mn atoms and an equatorial carbon atom of Mn$_2$(CO)$_{10}$. The absolute vale of the contours (au) increase from the outermost on inward in steps of $m \times 10^n$, with $m = 2, 4, 8$ and n beginning at -3 and increasing in steps of 1. Bond paths are superimposed. (Reprinted with permission from ref 217b. Copyright 1998 The Royal Society of Chemistry.)

0.19 and $\nabla^2\rho_{BCP}$ equal to the positive, but relatively low, value of 0.815(8) formally characterizes the Mn–Mn bond (2.9042(8) Å) as a closed-shell metallic bond, as concluded by the authors.

Other criteria lead to different conclusions on the nature of such M–M bonding. Theoretical results for unsupported Ti–Co and Zr–Co bonds in two hetero-bimetallic complexes, and parallel examination of AIM properties and the ELF function[219] indicate that these bonds are, albeit weak, highly polar covalent bonds with bond orders less than 0.5. In the Ti–Co

bond, the ELF function shows a compact disk-shaped maximum approximately in the middle of the bond, of height 0.46, whereas it would be close to zero in regions were no electron pairing occurs. The value of 0.46 is much lower than that found for most covalent bonds, which the authors attribute primarily to the highly polar nature of this covalent M–M bond.

Since the ELF function is not accessible from the experimental density, Macchi, Proserpio, and Sironi, in two studies on Co$_2$(CO)$_6$(AsPh$_3$)$_2$ (**28**, Scheme 28)[220]

Scheme 28
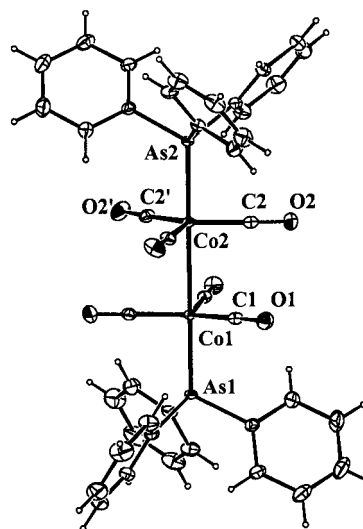
and Co$_4$(CO)$_8$(μ_2-CO)$_3$PPh$_3$ (**29**, Scheme 29),[221] use other quantities derivable from ρ to arrive at very similar conclusions about the nature of unsupported M–M bonds (see Table 6). Cremer and Kraka showed that a negative energy density at the BCP is typical for shared interactions, while the positive kinetic energy density dominates in typical ionic bonds, which thus typically have positive values of the total energy density at the bond critical point $H(\mathbf{r}_{BCP})$.[222] Thus, in addition to ρ_{BCP} and $\nabla^2\rho_{BCP}$, the quantities to be examined to assess the nature of bonding should include the local kinetic and total energy densities at the BCPs, $G(\mathbf{r}_{BCP})$ and $H(\mathbf{r}_{BCP})$, respectively.
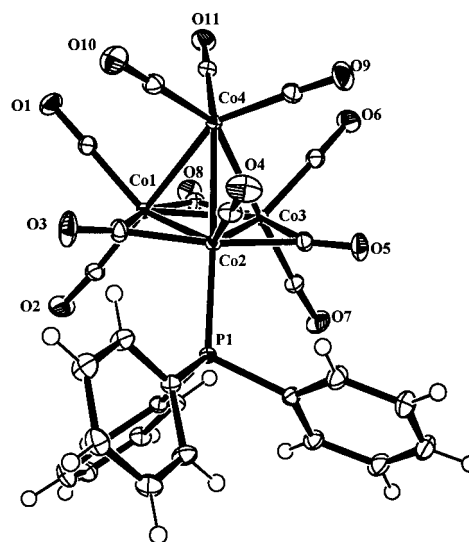
Scheme 29

Table 6. Features Characterizing Light−Light (L−L) and Heavy−Heavy (H−H) Atom Interactions (Ref 221). $L(\mathbf{r}_{BCP})$**is the Negative of the Lapacian at the Bond Critical Point,** $G(\mathbf{r}_{BCP})$ **and** $H(\mathbf{r}_{BCP})$ **Are, Respectively, the Kinetic and Total Energy Densities at the Bond Critical Point**

	$\rho(\mathbf{r}_{BCP})$	position of $\mathbf{r}_{BCP}$ with respect to $L(\mathbf{r})$ along bond path	$L(\mathbf{r}_{BCP})$	$G(\mathbf{r}_{BCP})/\rho(\mathbf{r}_{BCP})$	$H(\mathbf{r}_{BCP})$
		L−L bonds			
open shell	large	close to a minimum	>0	<1	<0
intermediate (e.g., CO)	large	close to a nodal surface	arbitrary	≥1	<0
closed shell	small	inside a flat region	<0	≥1	>0
		H−H bonds			
shared (e.g., Co−Co)		close to a maximum	∼0	<1	<0
donor acceptor (e.g., Co−As)		close to a nodal surface	<0	∼1	<0

In the experimental analyses, the energy densities along the bond path can be derived from the electron density using the Abramov functional.[156] The unsupported Co−Co (2.6430(2) Å) and Co−As (2.2906(2) Å) bonds in **28** are both represented by bond paths with significant electron densities at the BCP (∼0.20(1) and 0.46(1), respectively), with $\nabla^2(\mathbf{r}_{BCP})$ slightly positive. The potential and kinetic energy densities are both very small in magnitude, but the (everywhere negative) potential energy density dominates the total energy density, resulting in a slightly negative energy density at the BCP ($H(\mathbf{r}_{BCP}) < 0$). Macchi et al. conclude that the Co−Co bond is far from the closed-shell limit and state "*we do not find any reason for not considering it a shared interaction as suggested by common chemical sense*". In the Co−As bond, the BCP is shifted toward the less electronegative Co atom. On the basis of the shape of $\nabla^2\rho$ along the bond path, the bond appears as a highly polar shared interaction, somewhat at variance with expectations. The agreement between the experimental Laplacian and that calculated for a model compound without the phenyl groups is very good for both the Co−As and Co−Co bonds.

Three supported and three unsupported Co−Co bonds occur in **29**, Co₄(CO)₈(μ_2-CO)₃PPh₃. While the 18-electron rule predicts six metal−metal bonds between the pyramidally arranged Co atoms, only the unsupported bonds correspond to bond paths linking the metal atoms. The unsupported Co−Co bonds have small positive values of the Laplacian at the BCP but, importantly, negative values of $H(\mathbf{r}_{BCP})$, as is in fact the case for the unsupported Mn−Mn bond in Mn₂(CO)₁₀.[217]

Comparison of the density perpendicular to the Co−Co line in supported and unsupported bonds in **29** with theoretical densities of related compounds shows that upon bridging, the M−M density is spread out, the maximum in ρ is perpendicular to the bond direction, and with it the BCP disappears. The authors conclude that the Co−(μ_2-C$_{bridging}$)−Co bond is better characterized as a three-center four-electron bond. In accordance with this concept, the bond paths are curved 'inward' at the bridging carbon atom but then curve back to continue straight to the metal atoms (Figure 19). Thus, though the 18-electron rule would require direct bonds between all metal atoms in the complex, the detailed examination of the electron density reveals the more subtle nature of the bonding in these polynuclear transition-metal complexes.
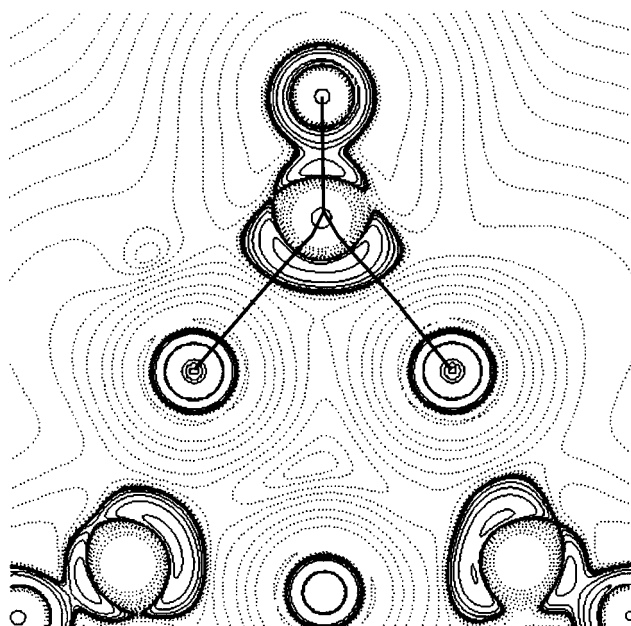

Figure 19. Lapacian distribution and bond paths for a bridging carbonyl in Co₄(CO)₈(μ_2-CO)₃PPh₃ (**29**). Negative contours solid; the superimposed bold lines represent the bond paths.[221]

VII. Physical Properties from the Experimental Density

A. Net Atomic and Molecular Charges

Even though the concept of the net charge of an atom in a molecule is subject to interpretation, as discussed in section II.A.3, it is widely applied for understanding the chemical behavior of molecules. The virial partitioning of the AIM theory is soundly based on quantum mechanics but tends to give charges quite different from those according to other definitions.

Insight into the analysis of net atomic charges is obtained by parallel analysis of structure factors based on a theoretical calculation of the crystal. Such results, for *p*-nitroaniline, are given in Table 7. When identical integration procedures are used, agreement between the experimental and theoretical net charges based on the structure factors is remarkable and almost always within 0.1 e. The effect of a difference in the definition of the atom is evident by comparing the first two columns of the table for both experiment and theory. Comparison of the last two columns, listing the multipole-based topological results and

Table 7. Net Atomic Charges in *p*-Nitroaniline from Monopole Populations, *Q(M),* and from AIM Analysis, *Q(Ω),* from Experimental and Theoretical Charge Densities (ref 57)

atom (Ω)	experiment 20 K synchrotron		theory (PDFT/6-31G**)		
	$q(M)$	$q(\Omega)$	$q(M)^a$	$q(\Omega)^b$	$q(\Omega)^c$
average O	−0.21(3)	−0.44	−0.20(1)	−0.47	−0.56
N (amino)	+0.07(9)	−0.99	−0.09(2)	−1.02	−1.28
N (nitro)	−0.01(4)	+0.29	−0.06(2)	+0.32	+0.38
C(NH$_2$)	−0.16(6)	+0.26	−0.14(3)	+0.32	+0.50
average C(H)	−0.06(5)	−0.06	−0.09(3)	−0.07	−0.00
C(NO$_2$)	+0.04(6)	+0.21	+0.14(3)	+0.17	+0.21
average H (amino)	+0.15(3)	+0.47	+0.18(1)	+0.44	+0.48
average H (phenyl)	+0.11(2)	+0.10	+0.14(1)	+0.14	+0.08
$\sum q(NO_2)$	−0.43	−0.57	−0.46	−0.62	−0.74
$\sum q(NH_2)$	+0.37	−0.05	+0.27	−0.14	−0.31
$|\mu|$ (Debye)	12.4(10)	11.9	11.2(3)	11.5	11.8

[a] Multipole refinement of theoretical structure factors. [b] AIM analysis of electron density from multipole refinement of theoretical structure factors. [c] AIM analysis of the primary theoretical density.

those based on the primary theoretical density, shows that some error is introduced by use of the current multipole model, which may need to be more flexible when very high quality data are available.

For transition-metal complexes, all analyses are affected by the diffuseness of the outer ns and np shells, which if populated correspond to density remote from the atomic center. Though metal atom populations from the multipole refinement corresponding to charges more neutral than those predicted by the formal oxidation state have often been reported, this is not always the case, as shown in the results for the metal squarate complexes summarized in Table 5. In one of the first topological integrations of the density of a transition-metal atom, Bianchi et al. found for lithium bis(tetramethylammonium) hexanitrocobaltate(III) (**2**) a theoretical AIM charge of +1.73 e for the Co atom, compared with a value of +2.23(7) e obtained with the multipole refinement.[99] The net charge summed over the octahedral Co(NO$_2$)$_6$ anion is −1.13 e according to the multipole refinement and very close (−2.95 e) to the formal charge of the anion (−3) according to the AIM integration of the theoretical data. AIM integration software applicable to experimental data is now becoming available[56,57] but at the time of writing has not yet been widely applied to transition-metal complexes.

In general, the definition of net atomic charge introduces a much larger, conceptual, variation than uncertainties in either experiment or theory. At the current state of the art, differences between experiment and theory for a given molecule appear small compared with differences between alternative definitions.

In crystals containing more than one molecular component, such as crystalline hydrates (see the discussion in section VI.C), the charge transfer among the molecules in the crystal is of interest. In particular, in low-dimensional conductors, the molecular charge determines the energy of the Fermi surface in the conducting chains and therefore the nature of the Peierls transition. An early charge-density analysis of tetrathiofulvalene−tetracyanoquinodimethanide (TTF−TCNQ) led, by integration over the molecular volume and estimated correction for the scale factor uncertainty, to a charge transfer of 0.60 e.[5] This value is in excellent though perhaps

fortuitous agreement with the transfer of 0.59 e derived from the position of the satellite reflections in the insulating low-temperature phase. A more recent analysis on bis(thiodimethylene)−tetrathiofulvalene tetracyanoquinodimethane (BTDMTTF−TCNQ) leads to a net transfer of ∼0.7 e and indicates that the charge transfer in this solid occurs between the 'external' thiodimethylene sulfur atoms at the extreme end of the molecule and the triple bonds of the cyano group of TCNQ.[223] A systematic analysis of a series of such complexes, as is now feasible, with application of the new topological integration techniques would be highly valuable.

B. Solid-State Dipole and Higher Moments and Nonlinear Optical Properties

In 1970, Stewart was the first to derive a molecular dipole moment from X-ray diffraction data.[224] His value of 4.0 ± 1.3 D for the molecule of uracil had a large assigned uncertainty but is surprisingly close to the solution value of 4.16 ± 0.4 D measured at a later date.[225] In the past decades it has become more widely recognized that electrostatic moments of molecules in the solid state can be derived from accurate X-ray diffraction data. A comprehensive coverage of the pre-1992 results is found in a review by Spackman of both dipole (first) and second moments.[8] In the current review we shall concentrate on the magnitude of the experimental dipole moments and its comparison with theoretical results.

Since X-ray diffraction is unique in being able to provide solid-state electrostatic moments, details of the application have come under increased scrutiny. As the electron density in a crystal is continuous, space must be partitioned if molecular properties are to be evaluated. This is less problematic than in the case of atoms, as the density in the intermolecular region is generally quite low. This is illustrated in the last row of Table 7,[57] which shows the experimental solid-state dipole moment for *p*-nitroaniline to be quite close to 12 D according to two very different methods of space partitioning. Typically this value is considerably larger than the isolated molecule dipole moment, which is 7.1 D according to MP2 and ∼8.1 D according to DFT and HF calculations.

There are many other examples, both theoretical and experimental, of enhancement of molecular

dipole moments in the solid state due to polarization induced by the lattice. This is not surprising as polar molecules tend to line up with facing opposite charges. A simple example is provided by the head-to-tail hydrogen-bonded chains in crystals of HCN.[226] A theoretical calculation (HF/6-31G**) shows that in the high-temperature tetragonal form the dipole moment is increased from the experimental gas-phase value of 2.5418 D (1.174 au) to 4.407 D (1.734 au), an increase of more than 50%. Compared with the HF value for the isolated molecule, the increase is still 38%. Similarly, a PHF calculation for crystal-line urea yields a molecular dipole moment increase from 5.15 D to 7.04.[98] More detailed analysis shows that the hydrogen atoms become more positive and the other atoms more negative or less positive upon crystallization, thus accounting for the increase in dipole moment.

The dipole moment of the water molecule in the solid state is of particular interest, given its ubiquitous presence in many systems. The water molecule has a dipole moment of 1.855 D in the gas phase.[227] A calculation on a cluster simulating ice-I_h yielded an enhancement of 0.9 D,[228] while PHF calculations on ice VIII give an increase from 2.142 to 2.593 D.[229] The latter result was reproduced by a refinement of theoretical structure factors, thus supporting the adequacy of the multipole model in the determination of molecular solid-state properties.[230] X−ray values in crystalline hydrates, as reported in the compilation of Spackman,[8] vary between 1.6 and 2.7 D with an average of 2.4 D. Thus, the increase of ∼0.4−0.9 D calculated for the ice phases I and VIII is qualitatively supported by the experimental data. An experimental study on deuterated ice-I_h is handicapped by the hydrogen atom disorder in the structure. Nevertheless, with careful modeling a dipole moment of 2.1 D was obtained.[231] Some more recent experimental values for the dipole moment of the water molecule in crystalline hydrates are as follows: for L-asparagine·H_2O,[232] 2.2 D (multipole) and 2.54 D (topological integration); for DL-proline·H_2O,[200] 2.7-(4) D (multipole); for glycyl-L-threonine·$2H_2O$, 1.6(3) and 2.2(8) D (multipole), for the two independent molecules, respectively.[118] No dipole moments were reported in a second charge-density study on glycyl-L-threonine·$2H_2O$.[119] In many cases idealized H positions have been assumed, as no neutron diffraction information is available. This introduces an uncertainty estimated at about 0.1 D in the results, which is usually smaller than the experimental error.

In a different approach, Bouhmaida et al. obtained the molecular moments of a small molecule or molecular fragment from the best fit to the experimental electrostatic potential.[233] Taking six sets of diffraction results, five of which are on amino acids, oligopeptides, or related substances and one from the natural zeolite natrolite, they find a calculated mean dipole moment for the water molecule of 2.23 D with a rms deviation of 0.22 D. The authors conclude that the dispersion reflects the different environments in the solid state and quote as evidence the out-of-plane displacement of the dipole moment of the natrolite water molecule with a component of 0.55 D, which

may be related to the relative location of the Na^+ ions.

For more complex molecules, much larger enhancements of the dipole moment have been found. Several concern molecules in acentric and, in particular, polar crystals, which often have particularly interesting solid-state properties. Dipole moment enhancement in non-centrosymmetric crystals may be especially strong because of the nature of the packing, but at the same time the ambiguity introduced by the X-ray phase problem is more severe. For acentric crystals, the structure factor phases can have any value rather than be restricted to 0° or 180°, which means that the least-squares adjustment is more flexible. Though this increases the uncertainty, there is no reason it would lead to a systematic *increase* in the observed dipole moments, as commonly observed, with the possible exception of acetamide, for which the refined dipole moment is too low rather than too large.[68] It is quite possible that the observed enhancements are related to the macroscopic polarization of a polar crystal, in which the molecular dipole moments along the polar axis accumulate.

A very large increase (from 9 to 25 D) was found for 2-methyl-4-nitroaniline (polar space group *Ia*),[234] the crystals of which have pronounced nonlinear optical properties. The increase from isolated molecule to the crystal was reproduced qualitatively by a calculation with the molecule in an applied electric field of a magnitude representing the crystal matrix effect but not by a recent PHF/6-21G** calculation on the crystal, which gave an increase to only 11.2 D.[235] For *p*-aminonitrobiphenyl (polar space group *Pca*2_1), the experimental dipole moment in the crystal is 25(4) D, compared with theoretical values of 9.2 D for the isolated molecule (B3LYP/6-311G**) and 11.3 D for the crystal (PHF 6-31G**).[236] Whether the theoretical periodic calculations which do not properly account for dispersion forces are in error or the experimental moments are systematically too large remains to be established.

The cap-shaped molecule phosphangulene (**30**, Scheme 30) (polar space group *R*3*m*) forms pyroelec-

Scheme 30
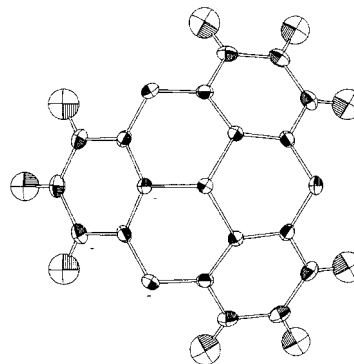
tric crystals. Its dipole moment was determined as 4.7(8) D, a 42% increase over the measured solution value.[237] By combining this dipole moment with the temperature dependence of the unit cell volume, Madsen et al. reproduced the pyroelectric coefficient of the material within the error limits, an excellent

illustration of the potential of the X-ray method for applications in materials science.

Because the induced polarization in crystals is a cooperative effect, it is dependent on molecular packing. In the crystals of *p*-aminonitrobiphenyl, the molecules are arranged in sheets of roughly parallel molecules linked by strong N−H···O hydrogen bonds. In contrast, the nitro groups in cocrystals of *p*-aminonitrobiphenyl with triphenylphosphine oxide (TPPO) (space group $P\bar{1}$) are involved only in weak O···H−C interactions, with the NH_2 hydrogen atoms participating in H bonds to the TPPO oxygen. In this arrangement the cooperative effect of extended head-to-tail hydrogen bonding is absent. Accordingly, the dipole moment of the molecule is reduced from the X-ray value of 25 D for the neat crystal to 16.8(1.6) D in the complex.[238] Thus, the experimental dipole moments can be used as a measure of the strength of polarizing effects in the crystal.

Further insight into the effect of the matrix on the dipole moment can be obtained by the study of molecules that crystallize in both centric and acentric polymorphic modifications. Gopalan, Kulkarni, and Rao[239] found the dipole moment for 5-nitrouracil in the noncentric polymorph to be much higher (9 D) than in the centric form, in which it is 5 D, close to the theoretical value for the isolated molecule. The effect is clearly related to the molecular packing, as the molecular geometries are essentially identical. The centric structure is composed of N−H···O hydrogen-bonded dimers, while the molecules in the acentric modification form N−H···O bonded linear chains. Among three 2,2-disubstituted 1,1-ethylenedicarbonitriles, reported in the same publication, the noncentric thioamino derivative (**31**, Scheme 31) that

Scheme 31
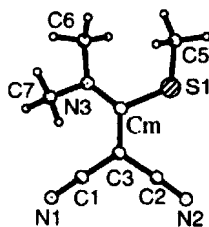
crystallizes in the polar space group $Pna2_1$ has a dipole moment of 15 D, compared to 8.1 D for the theoretical value for the molecule with the crystal geometry and 5 D for the molecule in its optimized geometry. For two other centrosymmetric, substituted 1,1-ethylenedicarbonitriles, however, the experimental solid-state dipole moments rather closely reproduce theoretical isolated-molecule values.

Thus, the evidence overwhelmingly points to an often pronounced, crystal-packing-dependent, enhancement of the dipole moments of molecules in crystals. A study by May, Destro, and Gatti on 3,4-bis(dimethylamino)-3-cyclobutene-1,2 dione (**32**, Scheme 32) is of particular interest for understanding the effect at the atomic level.[240] The intermolecular interactions in the crystal are exclusively of the C−H···O type, usually classified as weak interactions. Nevertheless, a highly significant molecular dipole moment enhancement occurs on crystallization. The

Scheme 32
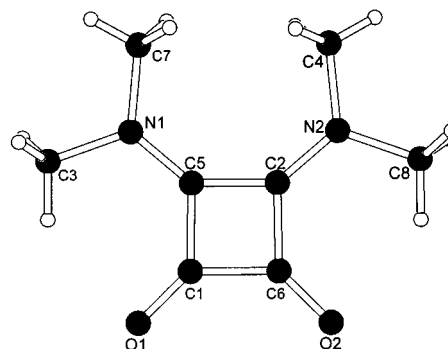
weak C−H···O interactions formed on crystallization induce an increase in the molecular dipole moment from the isolated molecule value of about 7 D to crystal values of 12.99 and 12.61 (theory) and 16.6-(13) and 16.2(12) D (experiment) for the two independent molecules in the cell, respectively. According to both theory and experiment, one molecule is slightly more polar, suggesting a differentiation by the solid-state environment. Analysis of the changes shows a small (about 0.2 e) net flux of electronic charge from the hydrogens of the methyl groups to the carbonyl oxygen atoms. Since the atoms lie rather far apart, the effect on the dipole moment is substantial. The authors note that the results support classification of the C−H···O interaction as a true H bond.

Somewhat smaller relative enhancements of dipole moment are obtained for amino acids, even in acentric crystals. Reported studies include L-alanine,[241] DL-proline,[38] and L-asparagine.[120] For all of these compounds, X-ray values of, respectively, 12.9, 13.0, and 14.3 D are only slightly larger than theoretical isolated molecule results of 12.4(HF/6-31G**), 11.2 (B3LYP-6-311G**),[242] and 13.1 D (B3LYP/6−311**G-(3df, 3pd)), respectively. For D,L-histidine, the increase is larger, the isolated molecule value being 9.8 D (B3LYP/6-311**) compared with an X-ray experimental value of 13.4(5) D and a theoretical crystal result of 13.1 D (PHF/6-21G**).[236]

The X-ray method may similarly be used for the derivation of higher moments. It has been noted that chemical bonding results in a systematic reduction of the magnitude $\langle r^2 \rangle$ of the second moment (i.e., trace of the second moment tensor) compared to that of isolated atoms and promolecules.[68,243] Model calculations by Spackman and Byrom on crystals composed of theoretical promolecules indicate that the expectation value of r^2 is well determined from the densities obtained through multipole refinement. Analysis of theoretical structure factors from periodic HF calculations on ice-VIII, acetylene, formamide, and urea indicate the effect of intermolecular interactions to be small for the magnitude of the second moment. More detailed examination of the results for acetylene and urea indicates the same to be the case for the principal tensor elements.[244]

It was first shown by Robinson that within several approximations, the nonlinear optical (NLO) properties of a molecule can be related to the molecular charge density.[245] The results show the elements of

the first-order polarizability tensor α_{ij} to be related to the molecular quadrupole moments, while those of the nonlinear second-order polarizability β_{ijk} are a function of both the molecular quadrupole and octupole moments. The Robinson expressions have now been applied to experimental charge densities as obtained from the multipole refinement. The first such study, by Baert, Zyss, and co-workers on N-(4-nitrophenyl)-L-prolinol,[246] gave quite reasonable qualitative agreement between charge-density-based and measured values for the principal components of the β-tensor. Similar results have been obtained in extensive studies by Antipin and co-workers on a series of dicyanovinylbenzenes.[247] As the experimental charge-density measurement has become quite rapid, the method can be used for the screening of promising NLO materials using tiny crystals rather than the larger samples needed for direct experimental measurement. Given the pronounced polarization effects in molecular crystals, described in the preceding paragraphs, it is generally accepted that deviations of the polarizability values from those calculated for isolated molecules are related to the effect of the matrix on the molecular charge density.

C. Electric Field Gradient at the Nuclear Positions

The contributions to the electric field gradient (EFG) can be divided into *central contributions* originating from the atomic valence-shell asphericity (and in particular its quadrupole component) and *peripheral contributions* due to the surrounding atoms. The latter become important when short distances are involved, as is the case for hydrogen atoms for which peripheral contributions outweigh the small quadrupolar component of the single valence electron. Tegenfeldt and Hermansson conclude, using results on LiOD·D$_2$O, LiNO$_3$·3D$_2$O, and NaDC$_2$O$_4$·D$_2$O, that for deuterium in hydrogen-bonded systems good diffraction data provide reasonable estimates of quadrupole coupling that at least qualitatively reflect variations in hydrogen bond strength.[248] For the deuterons in deuteriobenzene, very good agreement has been obtained between X-ray, NMR, and theoretical values for the principal components of the EFG.[12]

Two recent studies confirm that reliable values can be extracted from the X-ray data. A careful analysis of benzene by Spackman and co-workers, based on new experimental data, clearly distinguishes between the three crystallographically independent hydrogen atoms in the crystals and gives EFGs which agree within 2% with spectroscopic values, with a definite assignment of the three values to each of the H atoms.[249] Quadrupole coupling constants for the three H atoms of the NH$_3$ group of glycine are in good agreement with (more accurate) NQR values, as are the asymmetry parameters.[110]

For all other atoms, induced deformations in the electronic core, which are not accessible with most current X-ray data, affect the EFG and thus make the X-ray values less reliable. In a recent study of the EFG at the oxygen and nitrogen nuclei of L-asparagine,[120] an icosahedral representation of the EFG is used which includes information on both tensor magnitude and orientation. The agreement between the NMR and X-ray results for the three oxygen atoms of L-asparagine is quite reasonable, but it is poor for the three nitrogen atoms, the EFG elements of which, however, span a much smaller range of values. The principal elements for the three oxygen atoms correlate well with spectroscopic and theoretical results but indicate a systematic underestimation of magnitude by the X-ray method. This suggests that a Sternheimer antishielding factor, routinely applied in the analysis of ^{57}Fe Mössbauer data to account for inner-shell polarization effects, should be introduced here also.[250] This is reasonable as the X-ray scattering formalism uses the frozen core approximation, so that induced polarization of the core is not accounted for. The authors conclude that while the charge density, its topological parameters, the dipole moment, and the electrostatic potential are well described from diffraction data, the EFG is simply more difficult to extract from the X-ray experiment. The EFG at the nuclear positions, being proportional to r^{-3}, r being the distance to the nucleus, is particularly sensitive to the region close to the nucleus.

In two studies X-ray results for iron complexes have been compared with Mössbauer hyperfine splittings. The shielding and antishielding factors required for the comparison have been calculated theoretically for Fe in different oxidation states using perturbation theory.[251] As the multipole formalism incorporates a flexible valence shell, it is appropriate to apply only core correction factors in the calculation of the hyperfine splitting from X-ray data. The combination of spectroscopic nuclear quadrupole splittings and X-ray charge density derived values for sodium nitroprusside, iron pyrite, and [Fe(tetraphenylporphyrin)(pyridyl)$_2$] have been used to calculate a value of $0.11(2) \times 10^{-28}$ m^2 for the nuclear quadrupole moment of the excited ^{57}Fe^m nucleus,[251] which agrees well with an earlier value of $0.12(2) \times 10^{-28}$ m^2 based on diffraction data of sodium nitroprusside and hematite.[252]

D. Electrostatic Potential

As the electrostatic potential ($\Phi(\mathbf{r})$) is an important function in the study of chemical reactivity, considerable attention has been paid to its derivation from the X-ray measurements. Electrostatic forces are long-range forces and therefore affect the path along which a reactant will approach a molecule. Regions of positive potential will attract nucleophilic reagents, while conversely, the negative regions of the molecule will determine the approach of electrophilic reagents.

An advantage of the experimental electrostatic potential over the potential from single-molecule calculations is that many-body effects in the crystal are accounted for. Of course, if the environment is different, many body effects may vary but molecules generally pack in characteristic ways dictated by the nature of the molecular interactions.

Examples of the experimental evaluation of the electrostatic potential include studies on the neurotransmitter γ-aminobutyric acid[253] and diisocyano-
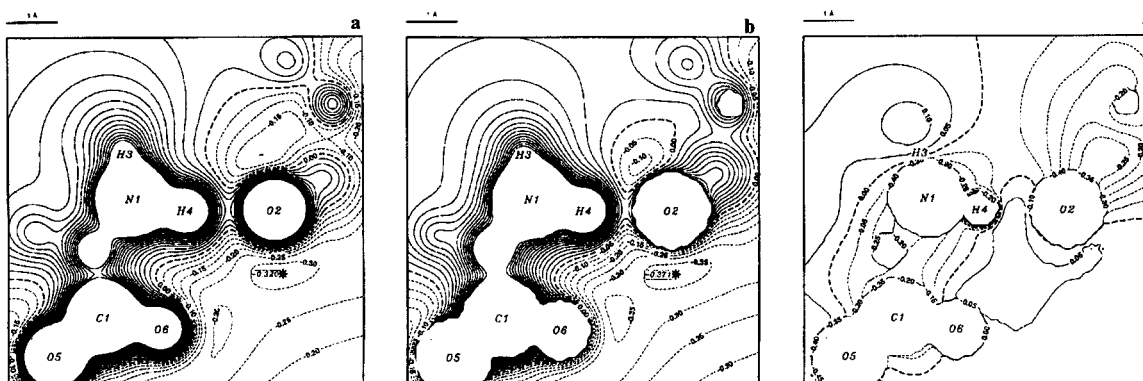
Figure 20. Electrostatic potential in the N−H···O hydrogen bond of L-arginine phosphate monohydrate: (a) experimental, (b) theoretical, (c) experiment−theory. Contours at 0.05 eÅ⁻³. Solid lines positive, dotted lines negative, zero contour broken.[257]

methane,[63a] the nonlinear optical solid 3-methyl 4-nitropyridine *N*-oxide,[254] the amino acids L-alanine[241] and L-asparagine,[120] the oligopeptides glycyl-L-threonine dihydrate[118] and triglycine,[116] nicotinamide,[255] β-cytidine and cytosine monohydrate,[256] and 2-pyridone.[134] Results reported are qualitatively predictable. They show, for example, negative potential regions adjacent to negatively charged nucleophilic oxygen atoms and positive potentials near hydrogen atoms. For the zwitterion glycyl-L-threonine, the potential around the carboxylic group is very negative and slightly asymmetric when a single molecule is examined. The negative feature is reduced as the water molecules of the coordination sphere are added and entirely neutralized when all hydrogen-bonded neighbors are included. A similar conclusion had already been drawn from comparison of the isolated molecule and crystal electrostatic potentials of L-alanine.[241] For L-arginine phosphate monohydrate, the agreement for $\Phi(\mathbf{r})$ between theory (HF triple-ζ plus diffuse and polarization functions) and experiment (130 K, X-ray and neutron data) is found to be quantitative within the small (<0.05) experimental errors (Figure 20) in the region of the hydrogen-bond between NH₃ and an oxygen atom of the phosphate group.[257] The map shows a topological saddle point in this region, which is a characteristic signature of H-bonding.

The electrostatic potentials of the four amino acids L-asparagine, DL-glutamic acid, DL-serine, and L-threonine (Figure 21) shows the common feature of a kidney-shaped electronegative region around the carboxylic group, which is more extended than the theoretical result for the isolated molecules, thus suggesting a polarization effect due to the crystal environment.[107]

A comparison between the electrostatic potentials of the 18-crown-6 macrocycle with and without a cation bonded in the center of the cycle has been made by Koritsanszky et al.[258] The electrostatic potential of the complexed crown ether molecule has only a relatively shallow depression at its center. However, when the potential of the K⁺ complexed molecule without the cation is examined, a deep minimum is observed at the cation position (Figure 22). Thus, the electrostatic potential reveals differences due to induced polarization by the cation, which
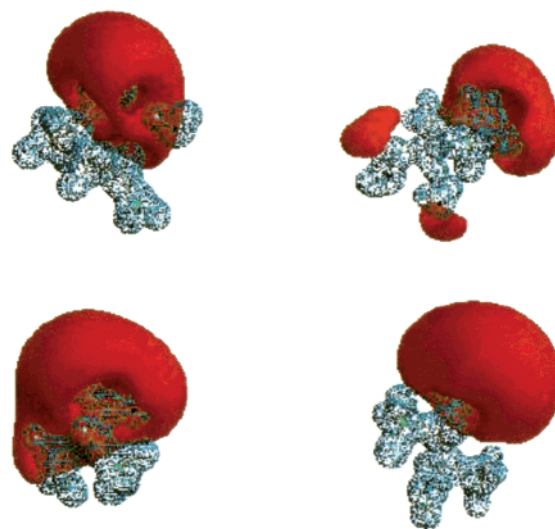

Figure 21. Isosurface representation of experimental electrostatic potentials (e/Å): blue, positive; red, negative; L-Asn (top left, surfaces at 0.5/−0.15); DL-Glu (top right, 0.5/−0.08); DL-Ser (bottom left, 0.5/−0.1); L-Thr (bottom right, 0.5/−0.1). The large red-colored regions represent the COO⁻ groups of the zwitterionic amino acids. (Reprinted with permission from ref 107b. Copyright 1999 Wiley-VCH.)
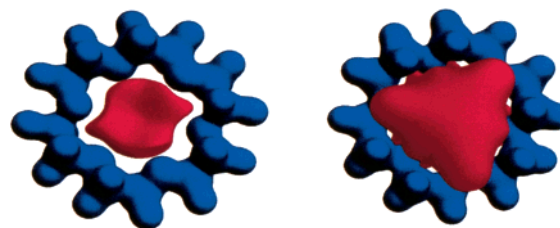

Figure 22. Isosurface representation of the experimental "pseudomolecular" electrostatic potential of the 18-crown-6-ring as extracted from the crystal environment of the neutral host−guest complex of 18-crown-6 with cyanamide (left) and the ionic complex, Kc18-crown-6 (right): blue (0.3 e/Å), red (−0.2 e/Å). The contribution of the guest molecule (cation) to the potential has been removed. The negative cavity in the ring is more extended for the macrocation than for the neutral molecule, indicating the polarization induced by the potassium cation.[258]

are not immediately obvious in the electron density itself.

To obtain the electrostatic potential of a much larger entity, Bouhmaida et al. assembled a fragment
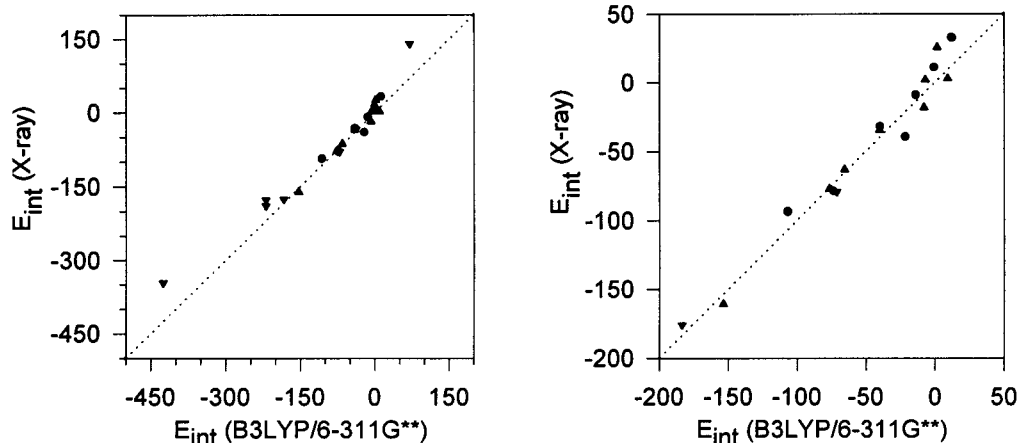
Figure 23. Experimental versus theoretical (DFT, supermolecule) intermolecular interaction energies (kJ/mol) in the dimers of DL-proline (●), DL-histidine (▲), and glycyglycine (▼). (b) Enlargement of the central area of part a. The dotted line represents exact agreement.[269]

of a number of small to medium-size peptides into the 3_{10} helix octapeptide Ac-Aib$_2$-L-Lys(Bz)-Aib$_2$–NHMe.[259] The fragment moments were obtained by the fitting of the electrostatic potentials of the isolated molecules and subsequently used to calculate the potential for the large entity. The results agree at least qualitatively with those from ab initio theory and Amber-dictionary charges. The methods used point the way to obtaining electrostatic potentials of macromolecules from small-molecule results, subject to the neglect of changes in the molecular environment.

E. Quantitative Evaluation of Electrostatic Interactions from the X-ray Charge Density

While the electrostatic potential gives information on likely directions of approach of nucleophilic and electrophilic reactants, the X-ray charge density contains quantitative information on the electrostatic interactions between molecules.

As noted by Price and co-workers, the electrostatic forces between molecules can be modeled far more accurately by representing the molecular charge distribution by sets of point *multipoles* on every atomic site than is possible with a point-charge model.[260] This is the *distributed multipole* model.[261] The importance of including distributed multipoles rather than only isotropic net atomic charges in molecular force fields was further demonstrated by Koch and Egert, who, by including distributed multipoles up to the quadrupole level, obtained a dramatic improvement in the calculation of host orientation in a benzene–hexacyclophane complex.[262]

The atom-centered multipoles are obtained in a straightforward manner from the multipolar population parameters from the X-ray aspherical-atom refinement. They were first applied in the calculation of molecular packing of amides and carboxylic acids by Berkovitch-Yellin and Leiserowitz.[263] The *experimental charge-density approach* to intermolecular interactions in crystals was developed systematically by Spackman.[264] In this approach, the anisotropic electrostatic interaction energy in the crystal is derived via an expression by Buckingham valid for nonoverlapping charge distributions.[12,265]

The Ewald lattice summation technique is used in the summation over the whole crystal. To obtain the total interaction energy, the Coulombic contribution is combined with the repulsive and dispersive van der Waals interaction energy evaluated with isotropic atom–atom *exp-6* potentials. Care must be taken in selecting the sets of atom–atom parameters to be used. As parameters obtained from minimization of lattice energies may be biased by the choice (or neglect) of net atomic charges, nonempirical sets are to be preferred. One such set was derived by Spackman[266] from the electron gas model within the Kim and Gordon approximation.[267] In recent applications of the technique by Abramov et al.,[268] an optimized hydrogen bond potential of Coombes, Price et al.[260] is introduced.

As illustrated in Figure 23, the method leads to quite satisfactory correlation with dimer interaction energies calculated by ab initio DFT methods.[269] For all but the strongest attractive and repulsive interactions the fit is linear, with relatively small deviations. In Figure 24 the charge-density interaction energies are compared with results based on multipole parameters obtained by refinement of structure factors
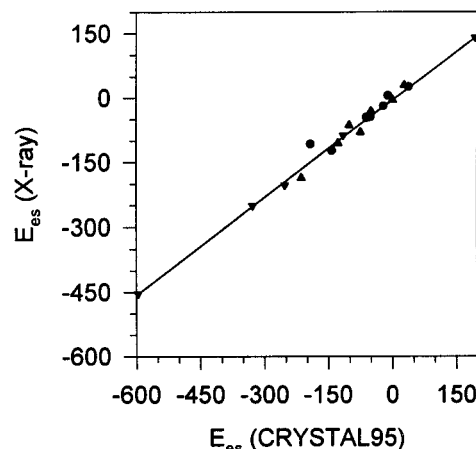

Figure 24. Comparison of experimental and theoretical (based on theoretical structure factors from Periodic HF calculations). Coulombic intermolecular interaction energies have units kJ/mol. Symbols as in Figure 23. The linear fit ($R = 0.99$) corresponds to the equation (a) E_{es}(X-ray) = $-2.78(369) + 0.76(2)E_{es}$(PHF).[269]

Table 8. Lattice Energies from X-ray Charge Densities and Theoretical Calculations (kJ/mol), from Refs 268 and 269

crystal	charge-density approach[a]	PHF/6-21G**	PHF/6-31G**
DL-histidine	−131.2	−134.9	−124.2
DL-proline·H$_2$O	−172.5	−177.7	
L-asparagine·H$_2$O	−98.7(16.7)		−122.8
glycylglycine	−274.9	−284.3	−279.5
p-nitroaniline	−96.5(11.5)	−0.6	+0.1

[a] From experiment. Esd's in parentheses.

from HF calculations for the periodic crystal. In a similar comparison based on DFT results, the slope of the fitted line is very close to one, but this is not the case when the HF method is used. The electrostatic interaction energy calculated with multipoles from refinement of PHF theoretical structure factors gives a linear fit ($R = 0.99$) with experimental values but with a slope that is significantly different from one (Figure 24). Its value of 0.76(2) indicates a systematic enhancement of the interaction densities derived from PHF results. This is in accordance with the well-known overestimation of the molecular polarity by HF calculations, generally attributed to the lack of electron correlation in the HF method. It is noticeable that the value of 0.76 resulting from the experiment/theory comparison is within three standard deviations of the correction factor of 0.81, applied by Price and co-workers in calculations of intermolecular interactions by reducing all electrostatic moments (including net atomic charges) to 90% of their HF values to account for the bias in the HF results.[270]

Lattice energies represent a more global measure of the interactions and are less sensitive to discrepancies in individual interactions, as errors in individual contributions may compensate each other. A comparison of charge-density-based lattice energies and theoretical results for DL-histidine, DL-proline, and α-diglycine, reproduced in Table 8, shows quite reasonable agreement as does comparison with calorimetric values when available.[269] The exception is p-nitroaniline (last column), which, surprisingly, is not or barely stable according to the periodic crystal calculations. The most likely explanation is that the theory at HF and DFT levels does not properly account for the stacking interaction between the aromatic rings. This explanation is supported by comparison of dimer interaction energies, which agree well for hydrogen-bonded dimers but disagree strongly for dimers stabilized by stacking interactions. Much better agreement with experimental interaction energies is reported when the interactions are evaluated at the post-HF MP2 level, which explicitly includes electron correlation.[269]

VIII. Concluding Remarks

During the past decade, X-ray charge-density analysis has grown into a mature field with widespread applications. Like the development of structure determination, it is being increasingly applied as methods have been standardized to a large extent so that more routine use becomes possible. Parallel analysis of theoretical results on both isolated molecules and periodic crystals is becoming common. In particular

for the crystal density, differences between theory and experiment have been identified which warrant further analysis. It has become very clear that molecular properties, such as dipole moments, change upon incorporation of the molecule into a solid.

In recent years data quality has become less of a concern, as redundancy of the measurements has increased significantly and low-temperature techniques are widely applied. With the improved quality of the data, emphasis has shifted to improvements in the charge-density model and to further development of interpretive techniques. Given the increased ease of data collection, many more applications of experimental charge-density analysis may be expected in coming years.

IX. Glossary of Abbreviations

ADP	atomic displacement parameters
AIM	atoms in molecules
APS	advanced photon source
BCP	bond critical point.
BP	bond path
CBED	convergent beam electron diffraction
CCP	cage critical point
CP	critical point
DCD	Dewar−Chatt−Duncanson
ED	electron distribution
EF	the electric field
EFG	electric field gradient
ELF	electron localization function
EP	electrostatic potential
F	coherent elastic scattering amplitude, structure factor
FHD	Fermi hole density
HF	Hartree−Fock
IAM	independent atom model
KRMM	κ'-restricted multipole model
LS	least squares
NLO	nonlinear optical
Ω	open quantum subsystem
PDFT	periodic density functional theory
PHF	periodic Hartree−Fock
RAHB	resonance-assisted hydrogen-bonding
RCP	ring critical point
TDS	thermal diffuse scattering
VSCC	valence shell charge concentration
VSEPR	valence shell electron pair repulsion

X. Acknowledgments

XI. References

(1) Debye, P. *Ann. Phys.* **1915**, *46*, 809.
(2) Destro, R.; Merati, F. *Acta Crystallogr.* **1995**, *B51*, 559.
(3) Scherer, W.; Spiegler, M.; Pedersen, B.; Tafipolsky, M.; Hieringer, W.; Reinhard, B.; Downs, A. J.; McGrady, G. S. *Chem. Commun.* **2000**, 635.
(4) Katan, C.; Rabiller, P.; Toupet, L. Reported at the 19th European Crystallography Meeting ECM19, Nancy, France, 2000.
(5) Coppens, P. *Phys. Rev. Lett.* **1975**, *35*, 98.
(6) Espinosa, E.; Molins, E.; Lecomte, C. *Chem. Phys. Lett.* **1998**, *285*, 170.
(7) Hirshfeld, F. L. *Crystallogr. Rev.* **1991**, *2*, 169−204.
(8) Spackman, M. A. *Chem. Rev.* **1992**, *92*, 1769−1797.
(9) Spackman, M. A.; Brown, A. S. *Annu. Rep. Prog. Chem., Sect. C: Phys. Chem.* **1994**, *91*, 175−212.
(10) Spackman, M. A. *Annu. Rep. Prog. Chem., Sect. C: Phys. Chem.* **1997**, *94*, 177−207.
(11) *Crystallography across the Sciences*; Schenk, C. H., Ed.; International Union of Crystallography: Chester, U. K., 1998.
(12) Coppens, P. *X-ray Charge Densities and Chemical Bonding*; Oxford University Press: Oxford, 1997.
(13) Tsirel'son, V. G.; Ozerov, R. P. *Electron Density and Bonding in Crystals*; Institute of Physics Publishing: Bristol, 1996.
(14) Born, M. *Z. Phys.* **1926**, *38*, 803.
(15) Stewart, R. F.; Feil, D. *Acta Crystallogr.* **1980**, *A36*, 503.
(16) Coppens, P. *Acta Crystallogr.* **1968**, *B24*, 1272. Coppens, P. *Acta Crystallogr.* **1974**, *B30*, 255−261.
(17) Allen, F. H. *Acta Crystallogr.* **1986**, *B42*, 515−522.
(18) Dunitz, J. D.; Seiler, P. *J. Am. Chem. Soc.* **1983**, *105*, 7056−7058.
(19) Schwarz, W. H. E.; Ruedenberg, K.; Mensching, L. *J. Am. Chem. Soc.* **1989**, *111*, 6926−6933.
(20) Mensching, L.; Von Niessen, W.; Valtazanos, P.; Ruedenberg, K.; Schwarz, W. H. E. *J. Am. Chem. Soc.* **1989**, *111*, 6933−6941.
(21) (a) Hirshfeld, F. L. *Acta Crystallogr.* **1971**, *B27*, 769. (b) Stewart, R. F. *Acta Crystallogr.* **1976**, *A32*, 565.
(22) Hansen, N. K.; Coppens, P. *Acta Crystallogr.* **1978**, *A34*, 909.
(23) Clementi, E.; Roetti, C. *At. Data Nucl. Data Tables* **1974**, *14*, 177.
(24) Su, Z.; Coppens, P. *Acta Crystallogr.* **1998**, *A54*, 646−652.
(25) Clementi, E.; Raimondi, D. L. *J. Chem. Phys.* **196**3, *38*, 2686.
(26) Coppens, P.; Guru Row: T. N.; Leung, P.; Stevens, E. D.; Becker, P. J.; Yang, Y. W. *Acta Crystallogr.* **1979**, *A35*, 63.
(27) Hirshfeld, F. L. *Theor. Chim. Acta* **1977**, *44*, 129.
(28) Su, Z.; Coppens, P. *Acta Crystallogr.* **1992**, *A48*, 188.
(29) (a) Epstein, J.; Swanton, D. J. *J. Chem. Phys.* **1982**, *77*, 1048. (b) Su, Z.; Coppens, P. *J. Appl. Crystallogr.* **1994**, *27*, 89.
(30) Seiler, P. In *Accurate Molecular Structures. Their Determination and Importance*; Domenicano, A., Hargittai, I., Eds.; Oxford University Press: Oxford, 1992; p 170.
(31) (a) Becker, P.; Coppens, P. *Acta Crystallogr.* **1974**, *A30*, 129. (b) Hester, J. R.; Okamura, F. P. *Acta Crystallogr.* **1996**, *A52*, 700.
(32) Stash, A. I.; Zavodnik, V. E. *Crystallogr. Rep.* **1996**, *41*, 404.
(33) (a) Luger, P. *Cryst. Res. Technol.* **1993**, *28*, 767. (b) Larsen, F. K. *Acta Crystallogr.* **1995**, *B51*, 468.
(34) (a) Zobel, D.; Luger, P.; Dreissig, W.; Koritsanszky, T. *Acta Crystallogr.* **1992**, *B48*, 837. (b) Figgis, B. N.; Iversen, B. B.; Larsen, F. K.; Reynolds, P. A. *Acta Crystallogr.* **1993**, *B49*, 794.
(35) Destro, R. *Aust. J. Phys.* **1988**, *41*, 503.
(36) Coppens, D. D.; Coppens, P.; Li, R. M.; Lee, P. *J. Appl. Crystallogr.* **1993**, *26*, 226.
(37) Blessing, R. H. *J. Appl. Crystallogr.* **1997**, *30*, 421.
(38) Koritsanszky, T.; Flaig, R.; Zobel, D.; Krane, H.-G.; Morgenroth, W.; Luger, P. *Science* **1998**, *279*, 356.
(39) see for example Coppens, P. *Synchrotron Radiation in Crystallography*; Academic Press: New York, 1992.
(40) (a) Nielsen, F. S.; Lee, P.; Coppens, P. *Acta Crystallogr.* **1986**, *B42*, 359. (b) Kirfel, A.; Eichhorn, K. *Acta Crystallogr.* **1990**, *A46*, 271.
(41) (a) Bolotovsky, R.; Darovsky, A.; Kezerashvili, V.; Coppens, P. *J. Synchrotron Radiat.* **1995**, *2*, 181. (b) Iversen, B. B.; Larsen, F. K.; Pinkerton, A. A.; Martin, A.; Darovsky, A.; Reynolds, P. A. *Acta Crystallogr.* **1999**, *B55*, 363.
(42) (a) Graafsma, H.; Svensson, S. O.; Kvick, A. *J. Appl. Crystallogr.* **1997**, *30*, 957. (b) Mallinson, P. R.; Barr, G.; Coles, S. J.; Guru Row: T. N.; MacNicol, D. D.; Teat, S. J.; Wozniak, K. *J. Synchrotron Radiat.* **2000**, *7*, 160.
(43) Darovsky, A.; Bolotovsky, R.; Coppens, P. *J. Appl. Crystallogr.* **1994**, *27*, 1039.
(44) Hardie, M. J.; Kirschbaum, K.; Martin, A.; Pinkerton, A. A. *J. Appl. Crystallogr.* **1998**, *31*, 815. Ribaud L.; Wu G.; Zhang Y. G.; Coppens P. *J. Appl. Crystallogr.* **2001**, *34*, 76.
(45) (a) Martin, A.; Pinkerton, A. A. *Acta Crystallogr.* **1998**, *B54*, 471. (b) Macchi, P.; Proserpio, D. M.; Sironi, A.; Soave, R.; Destro, R. *J. Appl. Crystallogr.* **1998**, *31*, 583. (c) Dahaoui, S.; Jelsch, C.; Howard, J. A. K.; Lecomte, C. *Acta Crystallogr.* **1999**, *B55*, 226.
(46) Macchi, P.; Proserpio, D. M.; Sironi, A. *J. Am. Chem. Soc.* **1998**, *120*, 1447.
(47) Kuntzinger, S.; Dahaoui, S.; Ghermani, N. E.; Lecomte, C.; Howard, J. A. K. *Acta Crystallogr.* **1999**, *B55*, 867.
(48) *DENZO, Kappa CCD Program Package*; Nonius BV: Delft, The Netherlands, 1998. (b) *SAINT Software Reference Manual*; Bruker AXS: Madison, WI, 1998.
(49) Gilmore, C. J. *Acta Crystallogr.* **1996**, *A52*, 561.
(50) Roversi, P.; Irwin, J. J.; Bricogne, G. *Acta Crystallogr.* **1998**, *A54*, 971−996.
(51) Stewart, R. F.; Spackman, M. A. *Valray User's Manual*; Department of Chemistry, Carnegie-Mellon University: Pittsburgh, PA, 1983.
(52) Craven, B. M.; Weber, H. P.; He, X. *Technical Report TR-872*; Department of Crystallography, University of Pittsburgh: Pittsburgh, PA, 1987.
(53) Figgis, B. N.; Reynolds, P. A.; Williams, G. A. *J. Chem. Soc., Dalton Trans.* **1980**, 2339.
(54) Koritsanszky, T.; Howard, S. T.; Richter, T.; Mallinson, P. R.; Su, J.; Hansen, N. K. *XD. A Computer Program Package for Multipole Refinement and Analysis of Charge Densities from X-ray Diffraction Data*; Free University of Berlin: Germany, 1995.
(55) Souhassou, M.; Blessing, R. *J. Appl. Crystallogr.* **1999**, *32*, 210.
(56) Flensburg, C.; Madsen, D. *Acta Crystallogr.* **2000**, *A56*, 24.
(57) Volkov, A.; Gatti, C.; Abramov, Yu.; Coppens, P. *Acta Crystallogr.* **2000**, *A56*, 252.
(58) Gatti, C. *TOPOND98 User's Manual*; CNR−CSRSRC: Milano, Italy, 1999.
(59) Kurki-Suonio, K. *Isr. J. Chem.* **1977**, *16*, 115.
(60) Hirshfeld, F. L. *Isr. J. Chem.* **1977**, *16*, 1226.
(61) Blessing, R. H. *Acta Crystallogr.* **1995**, *B51*, 816.
(62) Hirshfeld, F. L. *Acta Crystallogr.* **1976**, *A32*, 239.
(63) (a) Koritsanszky, T.; Buschmann, J.; Lentz, D.; Luger, P.; Perpetuo, G.; Röttger, M. *Chem. Eur. J.* **1999**, *5*, 3413. (b) Buschmann, J.; Koritsanszky, T.; Lentz, D.; Luger, P.; Nickelt, N.; Willemsen, S. *Z. Kristallogr.* **2000**, *215*, 487−494.
(64) Schomaker, V.; Trueblood, K. N. *Acta Crystallogr.* **1968**, *B24*, 63.
(65) Fuhrmann, P.; Koritsanszky, T.; Luger, P. *Z. Kristallogr.* **1997**, *212*, 213.
(66) Kampermann, S. P.; Ruble, R. J.; Craven, B. M. *Acta Crystallogr.* **1994**, *B50*, 737.
(67) El Haouzi, A.; Hansen, N. K.; Le Hénaff, C.; Protas, J. *Acta Crystallogr.* **1996**, *A52*, 291.
(68) Spackman, M. A.; Byrom, P. G. *Acta Crystallogr.* **1996**, *B52*, 1023.
(69) Krijn, M. P. C. M.; Graafsma, H.; Feil, D. *Acta Crystallogr.* **1988**, *B44*, 609.
(70) Dovesi, R.; Saunders: V. R.; Roetti, C.; Causa', M.; Harrison, N. M.; Orlando, R.; Apra', E. *CRYSTAL98 User's Manual*; University of Turin: Italy, 1995.
(71) Spackman, M. A.; Byrom, P. G.; Alfredsson, M.; Hermansson, K. *Acta Crystallogr.* **1999**, *A55*, 30.
(72) De Vries, R. Y.; Feil, D.; Tsirelson, V. G. *Acta Crystallogr.* **2000**, *B56*, 118.
(73) Spackman, M. A.; Byrom, P. G. *Acta Crystallogr.* **1997**, *B53*, 553.
(74) Haumann, T.; Boese, R.; Kozhushkov, S. I.; Rauch, A. K.; de Meijere, A. *Liebigs Ann./Recl.* **1997**, 2047−2053.
(75) Haumann, T.; Benet-Buchholz, J.; Klarner, F.-G.; Boese, R. *Liebigs Ann./Recl.* **1997**, 1429−1435.
(76) Bader, R. F. W. *Atoms in Molecules−A Quantum Theory*; Oxford University Press: Oxford, 1990.
(77) (a) Bader, R. F. W.; Nguyen-Dang, T. T.; Tal, Y. *Rep. Prog. Phys.* **1981**, *44*, 893. (b) Bader R. F. W.; Tal, Y.; Anderson, S. G.; Nguyen-Dang, T. T. *Isr. J. Chem.* **1980**, *19*, 8.
(78) Bader, R. F. W.; Essèn, H. *J. Chem. Phys.* **1984**, *80*, 1943.
(79) Collard, K.; Hall, G. G. *Int. J. Quantum Chem.* **1997**, *12*, 623.
(80) Johnson, C. American Crystallographic Association, Annual Meeting 1992, *Abstr. Ser. 2*, Vol. 29, p 105.
(81) Becke, A. D.; Edgecombe, K. E. *J. Chem. Phys.* **1990**, *92*, 5397.
(82) Bader R. F. W.; Johnson, S.; Tang, T.-H.; Popelier, P. L. A. *J. Phys. Chem.* **1996**, *100*, 15398.
(83) Bader, R. F. W.; Slee, T. S.; Cremer, D.; Kraka, E. *J. Am. Chem. Soc.* **1983**, *105*, 5061.
(84) Wiberg, K. B.; Bader, R. F. W.; Lau, C. D. H. *J. Am. Chem. Soc.* **1987**, *109*, 985.
(85) Cremer, D.; Kraka, E.; Slee, T. S.; Bader, R. F. W.; Lau, C. D. H.; Nguyen-Dang, T. T.; MacDougall, P. J. *J. Am. Chem. Soc.* **1983**, *105*, 5069.
(86) Bader, R. F. W.; Gillespie, R. J.; MacDougall, P. J. *J. Am. Chem. Soc.* **1988**, *110*, 7329.
(87) Bader, R. F. W.; Chang, C. *J. Phys. Chem.* **1989**, *93*, 2946.
(88) Gillespie, R. J. *Molecular Geometry*; Van Nostrand Reinhold: London, 1972.
(89) (a) Brown, A. S.; Spackman, M. A. *Acta Crystallogr.* **1990**, *A46*, 381. (b) Takata, M.; Sakata, M. *Acta Crystallogr.* **1996**, *A52*, 287.
(90) Abramov, Yu. A.; Okamura, F. P. *Acta Crystallogr.* **1997**, *A53*, 187.

(91) (a) Lu, Z. W.; Zunger, A.; Deutsch, M. *Phys. Rev.* **1993**, *B47*, 9385. (b) Lu, Z. W.; Zunger, A.; Deutsch, M. *Phys. Rev.* **1995**, *B52*, 11904.

(92) Zuo, P. F.; Bader, R. F. W. *Acta Crystallogr.* **1995**, *A50*, 714.

(93) Kapphahn, M.; Tsirelson, V. G.; Ozerov, R. P. *Port. Phys.* **1988**, *19*, 213.

(94) Stewart, R. F. In *Applications of Charge Density Research to Chemistry and Drug Design*; Jeffrey, G. A., Piniella, J. F., Eds.; Plenum Press: New York, 1991.

(95) Koritsanszky, T.; Buschmann, J.; Luger, P. *J. Phys. Chem.* **1996**, *100*, 10547.

(96) Gatti, C.; Bianchi, R.; Destro, R.; Merati, F. *J. Mol. Struct. (THEOCHEM)* **1992**, *255*, 409.

(97) Gatti, C.; MacDougall, P. J.; Bader, R. F. W. *J. Chem. Phys.* **1988**, *88*, 3792.

(98) Gatti, C.; Saunders: V. R.; Roetti, C. *J. Chem. Phys.* **1994**, *101*, 10686.

(99) Bianchi, R.; Gatti, C.; Adovasio, V.; Nardelli, M. *Acta Crystallogr.* **1996**, *B52*, 471.

(100) Howard, R. S. T.; Hursthouse, M. B.; Lehmann, C. W. *Acta Crystallogr.* **1995**, *B51*, 328.

(101) Volkov, A.; Abramov, Yu.; Coppens, P.; Gatti, C. *Acta Crystallogr.* **2000**, *A56*, 332.

(102) Brown, A. S.; Spackman, M. A. *Acta Crystallogr.* **1991**, *A47*, 21.

(103) Moss, G. R.; Souhassou, M.; Blessing, R. H.; Espinosa, E.; Lecomte, C. *Acta Crystallogr.* **1995**, *B51*, 650.

(104) Abramov, Yu.; Volkov, A.; Coppens, P. *Chem. Phys. Lett.* **1999**, *311*, 81.

(105) Volkov, A.; Abramov, Yu.; Coppens, P. *Acta Crystallogr.* **2001**, In Press.

(106) Flaig, R.; Koritsanszky, T.; Zobel, D.; Luger, P. *J. Am. Chem. Soc.* **1998**, *120*, 2227.

(107) (a) Flaig, R.; Koritsanszky, T.; Janczak, J.; Krane, H.-G.; Morgenroth, W.; Luger, P. *Angew. Chem.* **1999**, *111*, 1494. (b) Flaig, R.; Koritsanszky, T.; Janczak, J.; Krane, H.-G.; Morgenroth, W.; Luger, P *Angew. Chem., Int. Ed. Engl.* **1999**, *38*, 1397.

(108) Espinosa, E.; Lecomte, C.; Molins, E.; Veintemillas, S.; Cousson, A.; Paulus, W. *Acta Crystallogr. B* **1996**, *52*, 519.

(109) Dahaoui, S.; Pichon-Pesme, V.; Howard, J. A. K.; Lecomte, C. *J. Phys. Chem.* **1999**, *A103*, 6240.

(110) Destro, R.; Roversi, P.; Barzaghi, M.; Marsh, R. E. *J. Phys. Chem.* **2000**, *A104*, 1047.

(111) Coppens, P.; Abramov, Yu.; Carducci, M.; Korjov, B.; Novozhilova, I.; Alhambra, C.; Pressprich, M. R. *J. Am. Chem. Soc.* **1999**, *121*, 2585.

(112) Pichon-Pesme, V.; Lachekar, H.; Souhassou, M.; Lecomte, C. *Acta Crystallogr.* **2000**, *B56*, 728.

(113) Souhassou, M.; Lecomte, C.; Blessing, R. H.; Aubry, A.; Rohmer, M.-M.; Wiest, R.; Bénard, M. *Acta Crystallogr.* **1991**, *B47*, 253.

(114) Souhassou, M.; Lecomte, C.; Ghermani, N.-E.; Rohmer, M.-M.; Wiest, R.; Bénard, M.; Blessing, R. H. *J. Am. Chem. Soc.* **1992**, *114*, 2371.

(115) Wiest, R.; Pichon-Pesme, V.; Bénard, M.; Lecomte, C. *J. Phys. Chem.* **1994**, *98*, 1351.

(116) Pichon-Pesme, V.; Lecomte, C. *Acta Crystallogr.* **1998**, *B54*, 485.

(117) Dahaoui, S.; Jelsch, C.; Howard, J. A. K.; Lecomte, C. *Acta Crystallogr.* **1999**, *B55*, 226.

(118) Benabicha, F.; Pichon-Pesme, V.; Jelsch, C.; Lecomte, C.; Khmou, A. *Acta Crystallogr.* **2000**, *B56*, 155.

(119) Dittrich, B.; Flaig, R.; Koritsanszky, T.; Krane, H.-G.; Morgenroth, W.; Luger, P. *Chem. Eur. J.* **2000**, *6*, 2582.

(120) Arnold, W. D.; Sanders, L. K.; McMahon, M. T.; Volkov, A. V.; Wu, G.; Coppens, P.; Wilson, S. R.; Godbout, N.; Oldfield, E. *J. Am. Chem. Soc.* **2000**, *122*, 4708.

(121) Pérès, N.; Boukhris, A.; Souhassou, M.; Gavoille, G.; Lecomte, C. *Acta Crystallogr.* **1999**, *A55*, 1038.

(122) Koritsanszky, T.; Zobel, D.; Luger, P. *J. Phys. Chem.* **2000**, *A104*, 1549.

(123) Yufit, D. S.; Mallinson, P. R.; Muir, K. W.; Kozhushkov, S. I.; DeMeijere, A. *Acta Crystallogr.* **1996**, *B52*, 668.

(124) Roversi, P.; Barzaghi, M.; Merati, F.; Destro, R. *Can. J. Chem.* **1996**, *74*, 1145.

(125) Williams, R. V.; Kurtz, H. A.; Farley, B. *Tetrahedron* **1988**, *44*, 7455.

(126) (a) Dewar, M. J. S.; Lo, D. H. *J. Am. Chem. Soc.* **1971**, *93*, 7201. (b) Hoffmann, R.; Stohrer, W. D. *J. Am. Chem. Soc.* **1971**, *93*, 6941.

(127) Williams, R. V.; Gadgil, V. R.; Chauhan, K.; van der Helm, D.; Hossain, M. B.; Kackman, L. M.; Fernandes, E. *J. Am. Chem. Soc.* **1996**, *118*, 4208.

(128) Williams, R. V.; Gadhil, V. R.; Luger, P.; Koritsanszky, T.; Weber, M. *J. Org. Chem.* **1999**, *64*, 1180.

(129) Smith, G. T.; Mallinson, P. R.; Frampton, C. S.; Howard, J. A. K. *J. Chem. Soc., Perkin Trans.* **1997**, *2*, 1329.

(130) McCormack, K.; Mallinson, P. R.; Webster, B. C.; Yufit, D. S.; Slater, L. A.; Robins, D. J. *Acta Crystallogr.* **1997**, *B53*, 181.

(131) Howard, S. T.; Krygowski, T. M. *Can. J. Chem.* **1997**, *75*, 1174.

(132) Bianchi, R.; Gervasio, G.; Viscardi, G. *Acta Crystallogr.* **1998**, *B54*, 66.

(133) Klooster, W. T.; Swaminathan, S.; Nanni, R.; Craven, B. M. *Acta Crystallogr.* **1992**, *B48*, 217.

(134) Yang, H. W.; Craven, B. M. *Acta Crystallogr.* **1998**, *B54*, 912.

(135) McCormack, K. L.; Mallinson, P. R.; Webster, B. C.; Yufit, D. S. *J. Chem. Soc., Faraday Trans.* **1996**, *92*, 1709.

(136) Scherer, W.; Spiegler, M.; Pedersen, B.; Tafipolsky, M.; Hieringer, W.; Reinhard, B.; Downs, A. J.; McGrady, G. S. *Chem. Commun.* **2000**, 635.

(137) Musher, J. I. *Angew. Chem., Int. Ed. Engl.* **1969**, *8*, 54.

(138) Kálmán, A. *Croat. Chem. Acta* **1993**, *66*, 519.

(139) Koritsanszky, T. In *Intermolecular Interactions*; Gans, W., Boeyens, J. C. A., Eds.; Plenum Press: New York, 1998; p 57.

(140) Cioslowski, J.; Surján, P. R. *J. Mol. Struct. (THEOCHEM)* **1992**, *255*, 9.

(141) Bader, R. F. W.; Legare, D. A. *Can. J. Chem.* **1992**, *70*, 657.

(142) Antipin, M.; Boese, R.; Bläser, D.; Maulitz, A. *J. Am. Chem. Soc.* **1997**, *119*, 326.

(143) Lyssenko, K. A.; Antipin, M. Yu.; Lebedev, V. N. *Inorg. Chem.* **1998**, *37*, 5834.

(144) Boyd, R. J.; Choi, S. C. *Chem. Phys. Lett.* **1986**, *129*, 62.

(145) Koch, U.; Popelier, P. L. A. *J. Chem. Phys.* **1995**, *99*, 9747.

(146) (a) Hermansson, K.; Lunell, S. *Acta Crystallogr.* **1982**, *B38*, 2563. (b) Ojamäe, L.; Hermansson, K.; Pisani, K.; Causa, M.; Roetti, C. *Acta Crystallogr.* **1994**, *B50*, 268.

(147) Mallinson, P. R.; Wozniak, K.; Wilson, C. C.; McCormack, K. L.; Yufit, D. S. *J. Am. Chem. Soc.* **1999**, *121*, 4640.

(148) Mallinson, P. R.; Wozniak, K.; Smith G. T.; McCormack, K. L.; Yufit, D. S. *J. Am. Chem. Soc.* **1997**, *119*, 11502.

(149) Gilli, P.; Bertolasi, V.; Ferretti, V.; Gilli, G. *J. Am. Chem. Soc.* **1994**, *116*, 909.

(150) Speakman, J. C. *Struct. Bonding (Berlin)* **1972**, *12*, 141.

(151) Flensburg, C.; Larsen, S.; Stewart, R. F. *J. Phys. Chem.* **1995**, *99*, 10130.

(152) Madsen, D.; Flensburg, C.; Larsen, S. *J. Phys. Chem.* **1998**, *A102*, 2177

(153) Gilli, G.; Belluci, F.; Ferretti, V.; Bertolasi, V. *J. Am. Chem. Soc.* **1989**, *111*, 1023.

(154) Madsen, G. K. H.; Iversen, B. B.; Larsen, F. K.; Kapon, M.; Reisner, G. M.; Herbstein, F. H. *J. Am. Chem. Soc.* **1998**, *120*, 10040.

(155) Schiøtt, B.; Iversen, B. B.; Madsen, G. K. H.; Bruice, T. C. *J. Am. Chem. Soc.* **1998**, *120*, 12117.

(156) Abramov, Yu. A. *Acta Crystallogr.* **1997**, *A53*, 264.

(157) (a) Thomas, L. H. *Proc. Cambridge Philos. Soc.* **1927**, *23*, 542. (b) Fermi, E. *Z. Phys.* **1928**, *48*, 73.

(158) Von Weizsacker, C. F. *Z. Phys.* **1935**, *96*, 431. Kirzhitz, D. A. *Sov. Phys. JETP* **1957**, *5*, 64.

(159) Spackman, M. A. *Chem. Phys. Lett.* **1999**, *301*, 425.

(160) Espinosa, E.; Lecomte, C.; Molins, E. *Chem. Phys. Lett.* **1999**, *300*, 745.

(161) Espinosa, E.; Molins, E. *J. Chem. Phys.* **2000**, *113*, 5686–5694.

(162) Brown, G. E.; Gibbs, G. V.; Ribbe, P. H. *Am. Mineral.* **1969**, *54*, 1044.

(163) Cruickschank, D. W. J. *J. Chem. Soc.* **1961**, 5686.

(164) Gibbs, G. V. *Am. Mineral.* **1982**, *67*, 412.

(165) Tsirelson, V. G.; Evdokimova, O. A.; Belokoneva, E. L.; Urusov, V. S. *Phys. Chem. Miner.* **1990**, *17*, 275.

(166) Gibbs, G. V.; Hill, F. C.; Boisen, M. B. *Phys. Chem. Miner.* **1997**, *23*, 167.

(167) Downs, J. W. *J. Phys. Chem.* **1995**, *99*, 6849.

(168) (a) Kuntzinger, S.; Ghermani, N. E.; Dusausoy, Y.; Lecomte, C. *Acta Crystallogr.* **1998**, *B54*, 819. (b) Kirfel, A.; Gibbs, G. V. *Phys. Chem. Miner.* **2000**, *27*, 270.

(169) Ivanov, Yu. V.; Belokoneva, E. L.; Protas, J.; Hansen, N. K.; Tsirelson, V. G. *Acta Crystallogr.* **1998**, *B54*, 774.

(170) Downs, J. W.; Swope, J. *J. Phys. Chem.* **1992**, *96*, 4834.

(171) (a) Geisinger, K. L.; Spackman, M. A.; Gibbs, G. V. *J. Phys. Chem.* **1987**, *91*, 3237. (b) Rosso, K. M.; Gibbs, G. V.; Boisen, M. B. *Phys. Chem. Minerals* **1999**, *26*, 264.

(172) Chang, C.; Bader, R. F. W. *J. Phys. Chem.* **1992**, *96*, 1654.

(173) Popelier, P. L. A.; Bader, R. F. W. *J. Phys. Chem.* **1994**, *98*, 4473.

(174) Pichon-Pesme, V.; Lecomte, C.; Lachekar, H. *J. Phys. Chem.* **1995**, *99*, 6242

(175) Hirshfeld, F. L. *Acta Crystallogr.* **1976** *A32*, 239.

(176) Jelsch, C.; Pichon-Pesme, V.; Lecomte, C.; Aubry, A. *Acta Crystallogr.* **1998**, *D54*, 1306–1318.

(177) Housset, D.; Benabicha, F., Pichon-Pesme, V.; Jelsch, C.; Maierhofer, A.; David, S.; Fontecilla-Camps, J. C.; Lecomte, C. *Acta Crystallogr.* **2000**, *D56*, 151–160.

(178) Jelsch, C.; Teeter, M. M.; Lamzin, V.; Pichon-Pesme, V.; Blessing, R. H.; Lecomte, C. *Proc. Natl. Acad. Sci. U.S.A.* **2000**, *97*, 3171–3176.

(179) Guillot, B.; Jelsch, C.; Muzet, N., Lecomte, C. Reported at the 19th European Crystallographic Meeting, Nancy, August 2000; Abstract s3.m1.p7.

(180) Iwata, M.; Saito, Y. *Acta Crystallogr.* **1973**, *B29*, 8222.

(181) Iwata, M. *Acta Crystallogr. B* **1977**, *33*, 59.

(182) (a) Dewar, J. S. *Bull. Soc. Chim. Fr.* **1951**, *18*, C71. (b) Chatt, J.; Duncanson, L. A. *J. Am. Chem. Soc.* **1953**, 2939–2947.

(183) Rees, B.; Mitschler, A. *J. Am. Chem. Soc.* **1976**, *98*, 7918−7924.
(184) Coppens, P. In *Computational Chemistry-The Challenge of d and f Electrons*; Salahub, D. R., Zerner, M. C., Eds.; ACS Symposium Series 394; American Chemical Society: Washington, DC, 1973; pp 39−57.
(185) Lecomte, C.; Rohmer, M. M.; Benard, M. *Models for the Electronic Structure of Metalloporphyrins from HighResolution X-ray Diffraction and Ab Initio Calculations. The Porphyrin Handbook*; Kadish, K. M., Smith, K. M., Guilard, R., Eds.; Academic Press: New York, 2000; Vol. 7, pp 39−78.
(186) *Nature* **1999**, Sept 2.
(187) Zuo, J. M.; Kim, M.; O'Keeffe, M.; Spence, J. C. H. *Nature* **1999**, 48−52.
(188) Restori, R.; Schwarzenbach, D. *Acta Crystallogr.* **1986**, *B42*, 201−208.
(189) Scerri, E. *J. Chem. Educ.* **2000**, *77*, 1492.
(190) Wang, S.-G.; Schwartz, W. H. E. *Angew. Chem., Int. Ed.* **2000**, *39*, 1757−1762. See also: Zuo, J. M.; O'Keeffe, M.; Spence, J. C. H. *Angew. Chem., Int. Ed.* **2000**, *39*, 3791. Wang, S.-G.; Schwarz, W. H. E. *Angew. Chem., Int. Ed.* **2000**, *39*, 3794.
(191) Lippmann, T.; Schneider, J. R. *J. Appl. Crystallogr.* **2000**, *33*, 156−167; Lippmann, T.; Schneider, J. R. *Acta Crystallogr.* **2000**, *A56*, 575−584.
(192) Hwang, T.-S.; Wang, Y. *J. Phys. Chem.* **1998**, *102*, 3726−3731.
(193) Smith, G. T.; Mallinson, P. R.; Frampton, C. S.; Farrugia, L. J.; Peacock, R. D.; Howard, J. A. K. *J. Am. Chem. Soc.* **1997**, *119*, 5028−5034.
(194) Figgis, B. N.; Khor, L.; Kucharski, E. S.; Reynolds, P. A. *Acta Crystallogr.* **1993**, *B49*, 794−806.
(195) Figgis, B. N.; Kepert, C. J.; Kucharski, E. S.; Reynolds, P. A. *Acta Crystallogr.* **1992**, *B48*, 753−761.
(196) Figgis, B. N.; Iversen, B. B.; Larsen, F. K.; Reynolds, P. A. *Acta Crystallogr.* **1992**, *B48*, 144−151.
(197) Figgis, B. N.; Sobolev, A. N.; Young, D. M.; Schultz, A. J.; Reynolds, P. A. *J. Am. Chem. Soc.* **1998**, *120*, 8715−8723.
(198) Lee, C.-H.; Wang, C.-C.; Chen, K.-C.; Lee, G.-H.; Wang, Y. *J. Phys. Chem.* **1999**, *103*, 156−165.
(199) Chandler, G. S.; Christos, G. A.; Figgis, B. N.; Reynolds, P. A. *J. Chem Soc., Faraday Trans.* **1992**, *88*, 1961.
(200) Abramov, Yu. A. Unpublished results.
(201) Bats, J. W.; Fuess, H.; Ellerman, Y. *Acta Crystallogr.* **1986**, *B42*, 552.
(202) Fernandes; N. G., Tellgren, R.; Olovsson, I. *Acta Crystallogr.* **1990**, *B46*, 458.
(203) Wang, C.-C.; Wang, Y.; Liu, H.-J.; Lin, K.-J.; Chou, L.-K.; Chan, K.-S. *J. Phys. Chem.* **1997**, *A101*, 8887−8901.
(204) Macchi, P.; Proserpio, D. M.; Sironi, A. *J. Am. Chem. Soc.* **1998**, *120*, 1447−1455.
(205) Frenking, G.; Fröhlich, N. *Chem. Rev.* **100**, 717−774.
(206) Cremer, D.; Kraka, E. *J. Am. Chem. Soc.* **1985**, *107*, 3800−3810.
(207) Abramov, Yu. A.; Brammer, L.; Klooster, W. T.; Bullock, R. M. *Inorg. Chem.* **1998**, *37*, 6317−6328.
(208) Martin, M.; Rees, B.; Mitschler, A. *Acta Crystallogr.* **1982**, *B38*, 6−15.
(209) (a) Scherer, W.; Hieringer, W.; Spiegler, M.; Sirsch, P.; McGrady, G. S.; Downs, A. J.; Haaland, A.; Pedersen, B. *Chem. Commun.* **1998**, 2471−2472. (b) Scherer, W.; Priermeier, P.; Haaland, A.; Volden, G. S.; Downs, A. J.; Boese, R.; Blaser, D. *Organometallics* **1998**, *17*, 4406−4412.
(210) Popelier, P. L. A.; Logothetis, G. *J. Organomet. Chem.* **1998**, *555*, 101−111.
(211) Clemente, D. A.; Biagini, M. C.; Rees, B.; Herrmann, W. A. *Inorg. Chem.* **1982**, *21*, 3741−3749.
(212) Mitschler, A.; Rees, B.; Lehmann, M. S. *J. Am. Chem. Soc.* **1978**, *100*, 3390−3397.
(213) Low, A. A.; Kunze, K. L.; MacDougall, P. J.; Hall, M. B. *Inorg. Chem.* **1991**, *30*, 1079−1086.
(214) Heijser, W.; Baerends, E. J.; Ros, P. *Discuss. Faraday Soc.* **1980**, *14*, 211−234.
(215) Bénard, M.; Coppens, P.; DeLucia, M. L.; Stevens, E. D. *Inorg. Chem.* **1980**, *19*, 1924−1930.
(216) Mitschler, A.; Rees, B.; Wiest, R.; Bénard, M. *J. Am. Chem. Soc.* **1982**, *104*, 7501−7509.
(217) (a) Bianchi, R.; Gervasio, G.; Marabello, D. *Inorg. Chem.* **2000**, *39*, 2360−2366. (b) Bianchi, R.; Gervasio, G.; Marabello, D. *Chem. Commun.* **1998**, 1535−1536.
(218) Brown, D. A.; Chambers, W. J.; Fitzpatrick, N. J.; Rawilson, R. M. *J. Chem. Soc. A* **1971**, 720−725.
(219) Jansen, G.; Schubart, M.; Findeis, B.; Gade, L. H.; Scowen, I. J.; McPartlin, M. *J. Am. Chem. Soc.* **1998**, *120*, 7239−7251.
(220) Macchi, P.; Proserpio, D. M.; Sironi, A. *J. Am. Chem. Soc.* **1998**, *120*, 13429−13435.
(221) Macchi, P.; Garlaschelli, L.; Martinengo, S.; Sironi, A. *J. Am. Chem. Soc.* **1999**, *121*, 10428−10429.
(222) Cremer, D.; Kraka, E. *Croat. Chem. Acta* **1984**, *57*, 1259−1281; Cremer, D.; Kraka, E. *Angew. Chem., Int. Ed. Engl.* **1984**, *23*, 62.
(223) Espinosa, E.; Molins, E.; Lecomte, C. *Phys. Rev. B.-II* **1997**, *56*, 1820−1833.
(224) Stewart, R. F. *J. Chem. Phys.* **1970**, *53*, 205.
(225) Kulakowska, I.; Geller, M.; Lesyng, B.; Wierzchowski, K. L. *Biochim. Biophys. Acta* **1974**, *361*, 119.
(226) Platts, J. A.; Howard, S. T. *J. Chem. Phys.* **1996**, *105*, 4668−4674.
(227) Lovas, F. J. *J. Phys. Chem.* **1978**, Ref. Data 7, 1445.
(228) Gregory, J. K.; Clary, D. C.; Liu, K.; Brown, M. G.; Saykally, R. J. *Science* **1997**, *275*, 814.
(229) Gatti, C.; Silvi, B.; Colonna, F. *Chem. Phys. Lett.* **1995**, *247*, 135−141.
(230) Spackman, M. A.; Byrom, P. G.; Alfredson, M.; Hermansson, K. *Acta Crystallogr.* **1999**, *A55*, 30.
(231) Vanbeek, C. G.; Overeem, J.; Ruble, J. R.; Craven, B. M. *Can. J. Chem.* **1996**, *74*, 943−950.
(232) Volkov A. V.; Coppens, P. Unpublished results.
(233) Bouhmadia, N.; Ghermani, N. E.; Lecomte, C.; Thalal, A. *Acta Crystallogr.* **1999**, *A55*, 729.
(234) Howard, S. T.; Hursthouse, M. B.; Lehmann, C. W.; Mallinson, P. R.; Frampton, C. S. *J. Chem. Phys.* **1992**, *97*, 5616.
(235) Volkov, A. V. Ph.D. Thesis, State University of New York at Buffalo, July 2000, p 114.
(236) Reference 235, p 47.
(237) Madsen, G. K. H.; Krebs, F. C.; Lebech, B.; Larsen, F. K. *Chem. Eur. J.* **2000**, *6*, 1797.
(238) Zhang Y.; Coppens, P. *Chem. Commun.* **1999**, *23*, 2425.
(239) Gopalan, R. S.; Kulkarni, G. U.; Rao, C. N. R. *Chem. Phys. Chem.* **2000**, *1*, 127−135.
(240) May, E.; Destro, R.; Gatti, C. Manuscript in preparation.
(241) Destro, R.; Bianchi, R.; Morosi, G. J. *J. Phys. Chem.* **1989**, *93*, 4447−4457.
(242) Abramov, Yu. A. Unpublished results.
(243) O'Keeffe, M.; Spence, J. C. H. *Acta Crystallogr.* **1994**, *A50*, 33−45.
(244) Spackman, M A.; Byrom, P. G.; Alfredson, M.; Hermansson, K. *Acta Crystallogr.* **1999**, *A55*, 30.
(245) Robinson, F. N. H. *Bell Syst. Techn. J.* **1967**, 913−9. Reference 12, pp 282−283.
(246) Fkyerat, A.; Guelzim, A.; Baert, F., Zyss, J.; Perigaud, A. *Phys. Rev.* **1996**, *B53*, 16236−16246. Fkyerat, A Guelzim, A.; Baert, F.; Paulus, W.; Heger, J.; Zyss, J.; Perigaud, A. *Acta Crystallogr.* **1995**, *B51*, 197−209.
(247) Antipin, M. Yu.; Clark, R. D.; Nesterov, V. N.; Lyssenko, K. A.; Timofeeva, T. V. *Proc. SPIE* **1998**, *3474*, 41−52.
(248) Tegenfeldt, J.; Hermannson, K. *Chem. Phys. Lett.* **1985**, *118*, 293.
(249) Spackman, M. A.; Goeta, A. E.; Howard, J. A. K.; Yufit, D. S. Reported at the 19th European Crystallography Meeting ECM19, Nancy, France, 2000.
(250) Reference 12, pp 226−227.
(251) Su, Z.; Coppens, P. *Acta Crystallogr.* **1996**, *A52*, 748.
(252) Tsirel'son, V. G.; Strel'tsov, V. A.; Makarov, E. F.; Ozerov, R. P. *Sov. Phys. JETP* **1987**, *65*, 1065.
(253) Stewart, R. F.; Craven B. M. *Biophys. J.* **1993**, *65*, 998.
(254) Hamzaoui, F.,; Baert, F.; Zyss, J. *J. Mater. Chem.* **1996**, *6*, 1123.
(255) Miwa, Y.; Mizuno, T.; Tsuchida, K.; Taga, T.; Iwata, Y. *Acta Crystallogr. B* **1999**, *55*, 78.
(256) Chen, L. R.; Craven, B. M. *Acta Crystallogr.* **1995**, *B51*, 1081.
(257) Espinosa, E.; Lecomte, C.; Ghermani, N. E.; Devémy, J.; Rohmer, M. M.; Bénard, M.; Molins, E. *J. Am. Chem. Soc.* **1996**, *118*, 2501−2502.
(258) (a) Koritsanszky, T.; Buschman, J.; Denner, L.; Luger, P.; Knöchel, A.; Haarich, M.; Patz, M. *J. Am. Chem. Soc.* **1991**, *113*, 8388−8398. (b) Koritsanszky, T.; Buschman, Luger, P.; Knochel, A.; Patz, M. *J. Am. Chem. Soc.* **1994**, *116*, 6748−6756.
(259) Bouhmaida, N.; Ghermani, N. E.; Jelsch, C.; Lecomte, C.; Rohmer, M.-M.; Benard, M. Reported at the 19th European Crystallography Meeting ECM19, Nancy, France, 2000.
(260) Coombes, D. S.; Price, S. L.; Willock, D. J.; Leslie, M. *J. Phys. Chem.* **1996**, *100*, 7352.
(261) (a) Stone, A. J. *Chem. Phys. Lett.* **1981**, *83*, 233. (b) Stone, A. J. *The Theory of Intermolecular Forces*; Clarendon Press: Oxford, 1996.
(262) Koch, U.; Egert, E. *J. Comput. Chem.* **1995**, *16*, 937.
(263) (a) Berkovitch-Yellin, Z.; Leiserowitz, L. *J. Am. Chem. Soc.* **1980**, *102*, 7677. (b) Berkovitch-Yellin, Z.; Leiserowitz, L. *J. Am. Chem. Soc.* **1982**, *104*, 4052.
(264) Spackman, M. A. *J. Chem. Phys.* **1986**, *85*, 6587.
(265) (a) Buckingham, A. D. In *Intermolecular Interactions: from Diatomics to Biopolymers*; Pullman, B., Ed.; Wiley & Sons: New York, 1978; pp 1−67.
(266) Spackman, M. A. *J. Chem. Phys.* **1986**, *85*, 6579.
(267) Kim, Y. S.; Gordon, R. G. *J. Chem. Phys.* **1974**, *60*, 1842.
(268) Abramov, Yu. A.; Volkov, A.; Wu, G.; Coppens, P. *Acta Crystallogr.* **2000**, *A56*, 585.
(269) Abramov, Yu. A.; Volkov, A.; Wu, G.; Coppens, P. *J. Phys. Chem.* **2000**, *B104*, 2183.
(270) Price, S. L.; Andrews, J. S.; Murray, C. W.; Amos, R. D. *J. Am. Chem. Soc.* **1992**, *114*, 8268−8276.